Water-Rock Interaction in the Coso Geothermal System

THESIS

Presented in Partial Fulfillment of the Requirements for the Degree Master of Science in the Graduate School of The Ohio State University

By

Bohyun Hwang, B.S.

Graduate Program in Geological Sciences

The Ohio State University

2014

Master's Examination Committee:

Prof. David Cole, Advisor

Prof. Michael Barton

Prof. Ann Cook

Abstract

The overarching objective of this study is to document the water-rock interaction at the Coso geothermal area where the U.S. Department of Energy Enhanced Geothermal Systems (EGS) experiments are conducted to better understand the thermal evolution of this system. This effort quantifies the relationship between mineralogy and the pore/fracture network in order to track the evolution of water-rock interaction as a function of space and time. The relationship among the size, shape and distribution of pores relevant to mineralogy and mineral abundance are used as indicators of how fluids migrate through and react within the micropore environment. This paper summarizes petrologic and geochemical characterizations on well cuttings from three East Flank wells, and one West Flank well, with the focus on one of the East Flank wells, Navy II well 42A-16, to better understand the geologic process of hydrothermal alteration, its evolution, and how changes in mineralogy impacted porosity and permeability.

Several alteration types in these well cuttings are observed with the two most important being:

$$NaAlSi_3O_8 \cdot CaAl_2Si_2O_8 + H_4SiO_4 + Na^+ = 2NaAlSi_3O_8 + Al^{+3} + Ca^{+2} + 4OH^- \quad (1)$$

$$(xNa, yCa)AlSi_3O_8 + K^+ + Na^+ + Fe^{+3} + Mg^{+2} + H_2O \rightarrow \quad (2)$$

$$(K, Na)_2(Al, Fe, Mg)_4Si_6O_{20}(OH)_4 + (x+mNaAlSi_3O_8, y\text{-}mCaAlSi_2O_8) + 2mCa^{+2}$$

where albitization of calcic-plagioclase is represented by (1), and sericitization after plagioclase is represented by reaction (2). Collectively these reactions are two of the most significantly occurring over the range of depths in Navy II well 42A-16. This albite-sericite alteration tends to be associated with the potassic alteration, and often occur together especially in quartz diorite and granodiorite host rocks. Secondary albite and sericite formed at the mid-stage of mineral paragenesis in this system. The earliest minerals to form were epidote, titanite, rutile/anatase, and chlorite (perhaps of earlier metamorphic origin); whereas the most recently formed mineral was calcite. Porosity modification in the form of dissolution pits in plagioclase are observed using SEM/QEMSCAN method. Plagioclase has the largest area percent of pores within the grains or adjacent to them with respect to the equation (1) and (2). The plagioclase dissolution pits are dominant especially from the sample at 2000-2010 ft in Navy II well 42A-16. These dissolution type pores are sometimes filled with either clay (e.g. sericite) or calcite which is the last alteration phase to form in this system.

Pore features were investigated using standard BET gas adsorption which interrogates pores from about 1.7 nm to 0.3 microns. These results indicate the current matrix porosity is extremely low – ranging from <0.01 to about 0.1 percent. A comparison of BET data with neutron scattering results indicate that a significant fraction of matrix pores are not part of any organized network. This is supported by a preliminary micro-CT scan of one key sample from Navy II well 42A-16 which revealed numerous very small unconnected pores. Micro-fracture porosity and permeability were estimated

from a nomogram approach developed by North and Knapp (1977) which also suggests very low values for these parameters during the late stage development of calcite veining.

Dedication

This document is dedicated to my family.

Acknowledgments

I would like to express my special appreciation to my advisor Dr. David Cole for his scientific guidance, encouragement and support. I would like to thank Dr. Michael Barton and Dr. Ann Cook for serving as my committee members, and thank Dr. Julie Sheets for unstintingly providing training in laboratory procedure and data acquisition, along with personal insight and lots of encouragement. I would also like to thank Dr. Susan Welch, Tingting Liu and all other SEMCAL members for their advice and help in the lab. Special thanks go to my fellow graduate students: Alexander Swift, for his encouragement and good council at various stages of my project, and Edwin Buchwalter for his contributions to the micro-CT work reported in this study. Last but not least, I want to thank my friends, family, and teachers for their daily support, enthusiasm, and inspiration as I dedicated myself to academics.

A graduate research assistantship in the School of Earth Sciences was supported through funding from the Office of Geothermal Technology Development and Office of Fossil Energy both in the US Department of Energy (DOE)

Vita

February 2006	Pyeongtaek Girl's High School, Republic of Korea
2012	B.S. Geology and Earth Environmental Sciences, Chungnam National University, Republic of Korea
2012 to present	Graduate Research Associate, Department of Earth Sciences, The Ohio State University, USA

Presentation

Water-Rock Interaction in the Coso Geothermal System, poster presented at the 28th Edward F. Hayes Research Forum. February 21, 2014. The Ohio State University, Columbus, OH

Fields of Study

Major Field: Geological Sciences

Table of Contents

List of Tables

List of Figures

Chapter 1: Introduction

Understanding rock composition and geophysical properties including mineralogy, porosity, and permeability is fundamental to deciphering the geological and geochemical history of geothermal systems. In such systems, it is critical to understand the evolution of alteration and its distribution in rocks, and changes in porosity as a function of time and depth. Changes in effective porosity and permeability determine how fluids migrate into the nano- to micropore system, especially within the low–permeability reservoir rocks. It is also necessary to evaluate changes in mineral assemblages because they may influence and be influenced by the water chemistry, and therefore may help to reveal water-rock interactions. These are needed to better constrain the thermal anomaly and how the system evolves with time during production (e.g. changes in reservoir temperatures, pressures, and corresponding thermal activities).

The Coso geothermal field is a high temperature system and is America's second largest electricity producer by geothermal energy (Fialko and Simons, 2000) using Enhanced Geothermal Systems (EGS) technology. The EGS technique is designed to improve permeability and injectivity of borehole wells, and thus allows electricity production without natural convective hydrothermal resources. A water-based EGS system requires a large volume of water to generate electricity, and a significant amount of this water is lost during production. Brown (2000) proposed a potential advantage of

substituting CO_2 instead of water as the heat transmission fluid in EGS production systems. Numerous benefits result from CO_2 as the fluid, including enhanced power output, minimized parasitic power consumption of the fluid circulation system (Huddlestone-Homes and Hayward, 2011), carbon sequestration opportunities, and minimized water use. While the CO_2-EGS technology looks promising, the most important uncertainties remain with regard to chemical interactions between fluids and rocks (Pruess, 2006).

The Coso area has been the focus of a number of geological, geophysical, and geochemical studies. Temperatures and chemical compositions of the fluids inside rocks of the Coso region were obtained from fluid inclusions, which indicate that the system has undergone several thermal events. In particular, the East Flank area is currently reheating (Adams et al., 2000; Kovac et al., 2005). In addition to higher heat flow within the Coso system, the rocks tend to be generally more porous than surrounding regional rocks. Average porosity of this area is 2%, but locally it is as high as 12% at depths ranging from ~1.5 to 3.0 km (Lees and Wu, 2000). A quantitative understanding of how key rock properties vary as a function of space (depth and lateral distribution) and time, however, remains elusive.

This research has combined several analytical methods including light Polarized Light Microscopy (PLM), X-ray diffraction (XRD), backscattered electron (BSE) imaging, gas sorption (BET), and neutron scattering, as described in Chapter 3. These analyses can be interpreted to better understand the Coso geothermal system, and ultimately help to construct the effective reactive surface area of various minerals in the

system by estimating the association between the minerals and pores. In addition, they may contribute to an overall understanding of similar geothermal systems.

The objective of this study is to determine the alteration mineralogy, the mineral paragenesis, the pore mineralogy, and the development of porosity and fracture networks while considering the following the key questions: (1) How does the mineralogy change as a function of depth and spatial location? (2) What is the relative timing of primary and secondary mineralization based on texture and cross-cutting relationships? (3) What are the size, distribution, and total volume of pores as a function of depth and spatial location across the 4 wells? (4) What minerals are most likely to be associated with pores/fractures?

Chapter 2: Background

2.1 Regional Geology and Thermal History

The Coso geothermal area lies within the Walker Lane/Eastern California Shear Zone (WLSZ), which is a tectonically active area (Newman et al., 2008), and is a region of high heat flow and seismicity. On a regional scale, the Coso geothermal area is located in the Coso Range, which includes the eastern part of the Sierra Nevada to the western flank of the Basin and Range tectonic province. The Coso geothermal field is one of several high-temperature geothermal systems in California. The site is approximately 160 miles north-northeast of Los Angeles, and completely within the borders of the Naval Air Weapons Station, China Lake.

Fractured Mesozoic plutonic rocks with minor metamorphic rocks compose the basement of this reservoir in the Coso region (Newman et al., 2008). They range in composition from leucogranite, light colored granitic rocks with almost no mafic minerals, to gabbro. These rocks have been intruded by fine-grained dikes and are partially covered by late Cenozoic volcanic rocks, as shown in Figure 1. The reservoir rocks of this area are dominated by diorite, granodiorite, and granite (Newman et al., 2008; Kovac et al., 2004). Collectively, even though the plutons constitute part of the composite Sierra Nevada batholith, the rock units in Coso are structurally separated from the main body of the batholith along the Sierra Nevada fault zone (Duffield et al., 1980).

Over the past 600,000 years, volcanism has produced 39 rhyolite domes in the central region of the Coso field, together with basalt along the margins. The depths from which the rhyolites erupted have moved shallower with time, ranging from ~10 km (0.6 Ma magma) to ~5.5 km for the youngest (~0.04 Ma magma). These data suggest that the magma chamber has moved upward toward the surface (Manley and Bacon, 2000), and this partially molten magma body is believed to be the heat source for the present geothermal system (Newman et al., 2008). Moreover, frequent seismicity (Walter and Weaver, 1980) along with teleseismic P-delay tomography (Reasenberg et al., 1980) provides evidence for a magma body at ~5 km below the surface (Wilson et al., 2003).

A substantial influence on the Pleistocene volcanic rocks and fluids from the asthenosphere is documented by Monastero et al. (2005). The combination of a strong positive gravity anomaly and a strong asthenospheric signature in isotopic analytical results (Sr and Nd) indicates that the crust is thinned within the Coso region. The thinned crust in turn supports the assertion that crustal thinning in the Coso Range enabled mantle melts to reach to the shallow depths of approximately 3.5 to 4 km consistent with the observed temperature anomaly. The thinned crust overlies a more dense mafic body at depths of 10 km or less, and these mafic rocks may be cumulates left over from the fractional crystallization of rhyolite (Monastero et al., 2005).

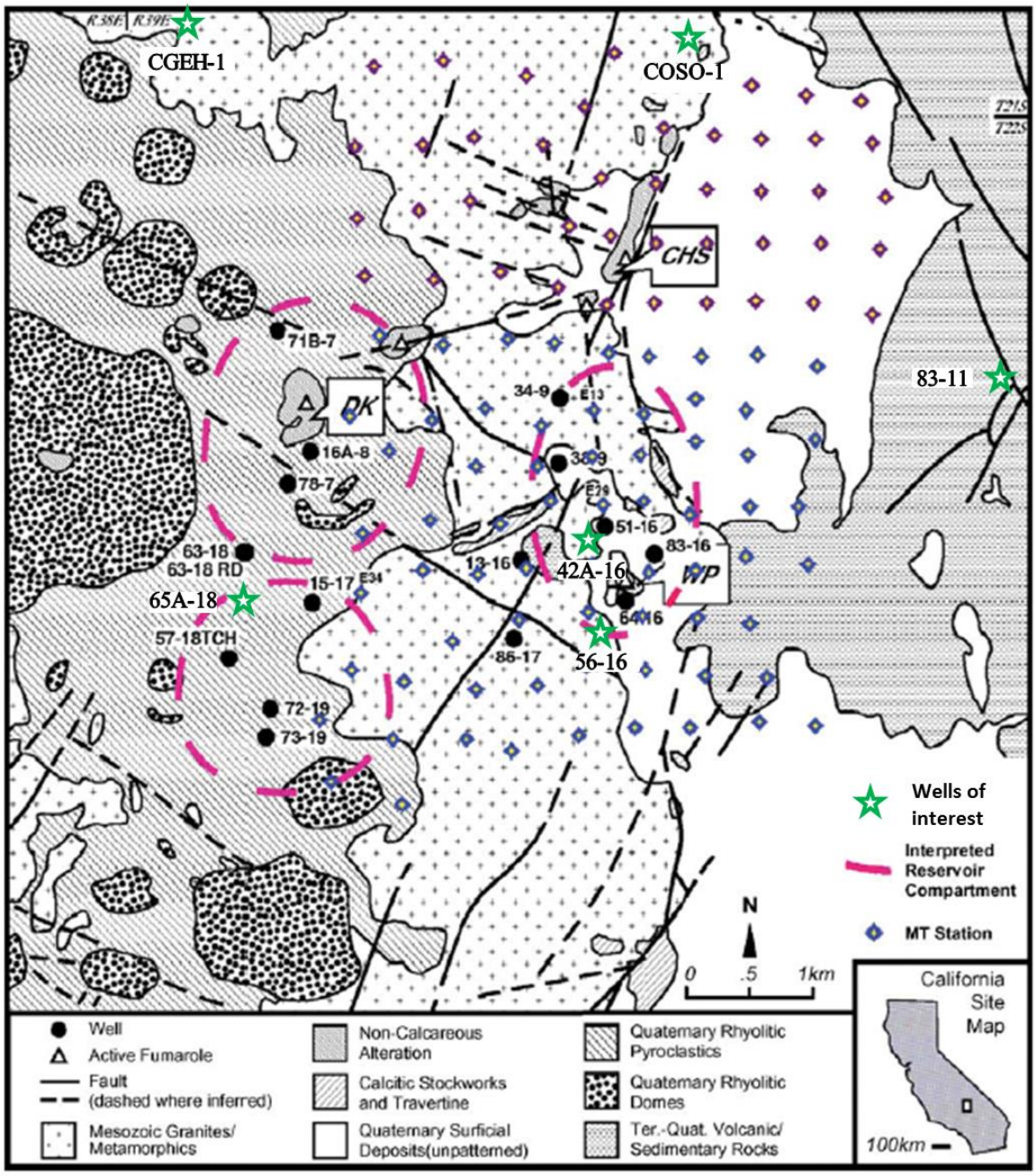

Figure 1. Geological map of the Coso geothermal area showing lithologies and structures on the surface, including faults. Green stars locate borehole wells of interest. Abbreviations: CHS (Coso Hot Springs), DK (Devil's Kitchen), WP (Wheeler Prospect), RD (Redrill), TCH (Thermal core hole). (after Newman et al., 2008; Adams et al., 2000; Whitmarsh, 2002).

Two main volcanic events have affected Cenozoic rocks in this system; the first event was between the middle and late Pliocene Epoch (4.0 to 2.5 Ma), and a more recent one occurred during the Pleistocene Epoch (~1.0 to 0.01 Ma) (Duffield et al., 1980). The Pliocene volcanic rocks represent approximately 88 percent of the total volume of extrusive rocks found in the Coso field and range from basalt to rhyolite in composition, but all belong to the calc-alkaline magma series. The Pleistocene volcanic rocks occur in a more limited area in the central and southern Coso Range. They make up only about 12 percent by volume of volcanic rocks, and are composed of either high-silica rhyolite or basalt. The rhyolites, which occur in the central part of the Coso Range, are pumiceous, perlitic, and endogenetic domes with ash-flow tuffs, block and ash flows, and air fall tuffs filling in between the domes. In comparison, the basalts occur mostly as flows with a considerable amount of pyroclastic material on the southern and western flanks of the Coso Range.

Additionally, three periods of recent geothermal activity are documented by Adams et al. (2000). The first, which occurred approximately 307 ka (0.3 Ma) ago, is associated with travertine deposits that may have been related to a large low- to moderate temperature geothermal system on the eastern side of the field. The second event produced a high temperature geothermal system triggered by magmatic activity beneath the dome field, and is associated with sinter deposits that formed at 238 ka (0.2 Ma) in the eastern and southern part of the present-day field. These fossil sinter and travertine deposits occur along a northerly trending fault zone on the eastern margin of the field (Figure 1). The most recent event, located in the southwestern part of the field, increased

the temperature of the system by at least 100°C in a major upflow zone, where heated, buoyant hydrothermal fluids ascended. The present day activity appears to be prograding (increasing in temperature) and may have begun within the last several tens of thousands of years (Kurilovitch et al., 2003). Thermal gradients range from 85°C/km to 120°C/km (Combs, 1980), which is substantially higher than the worldwide average of 25°C/km. Geothermal production wells encountered older greenschist facies metamorphism of quartz diorite in the reservoir rock (Kovac et al., 2005), which was produced by the initial thermal event, and mylonitic structures at 4 km depth, as documented by Monastero et al. (2005). Etzel et al. (2013) identified several zones of increasing $^{18}O/^{16}O$ depletion down each borehole near the north of Devil's Kitchen, suggesting that these zones in the rock reservoir have interacted and exchanged isotropically with significant quantities of geothermal fluid which means a higher ratio of water/rock in the past or current geothermal activity by higher permeability of the system with attainment of local equilibrium with geothermal fluids.

2.2 Heat Flow and Energy Resources

The Coso Geothermal Field has been producing geothermal power continuously since 1987, with four geothermal power plants that have a total of nine 30 Megawatt-electrical (MWe) turbine generator sets, yielding a total of 270 MWe of rated capacity (Figure 2). At 302 MWe, the net running capacity is higher than the rated capacity due to the region of high fluid pressures and temperatures encountered in this field (Monastero, 2002). The mass flow rate of injected fluid is more than 14 million pounds per hour from 80-90 production wells at a given time. Wellhead pressures range from 85-500 psig

(5.86-34.47 bar). According to a USGS report on geothermal energy resources (Williams et al., 2008), the mean estimated reservoir temperature of the Coso geothermal field is 285°C, the mean estimated reservoir volume is 30 km^3, and the mean estimated capacity of electricity production is 518 MWe. Given the rate of production historically, this geothermal field will likely continue to produce electricity for at least several decades.

Figure 2. The Navy 1 Coso geothermal power plant near Coso Hot Springs in southern Inyo County showing turbine generators producing electricity. Some of the 39 light-colored rhyolitic lava domes of the Coso volcanic field are shown in the background (Sobash et al., 2014).

2.3 Previous Work

2.3.1 Mineralogy

According to Bishop and Bird (1987), primary igneous minerals of the Coso subsurface rocks consist of quartz, alkali feldspar, plagioclase, biotite, and hornblende, with accessory apatite, titanite, pyrite, and magnetite. Metamorphic rocks, including primarily biotite schist and gneiss, consist of plagioclase, microcline, quartz, hornblende, biotite, epidote, chlorite, and muscovite with minor calcite and iron oxides. Epidote and muscovite are observed as porphryoblasts in metamorphic rocks and also as fine-grained replacement of calcium-rich zones in plagioclase (Bishop and Bird, 1987). Four distinct veining or fracture filling events have been characterized based on the cross-cutting relationships in rocks and minerals (Bishop and Bird, 1987). The oldest veins, which are referred to as Stage 1 of 4, contain extensive pyrite, magnetite, epidote, and quartz cross cut by calcite. Stage 2 exhibits calcite + hematite + chlorite as a form of sealed veins. Stages 3 and 4 are divided into two subgroups depending on depths; shallow (A) and deep (B) depths respectively. A boiling event in Stage 3 is identified based on the presence of intergrown euhedral quartz crystals and blade-shaped calcite. The last stage, Stage 4, is dominated by calcite vein assemblages. These are divided into two subgroups based on different morphologies which are verified by cross-cutting relationships. The mineralogy associated with each stage is shown in Figure 3 (Kovac et al., 2005).

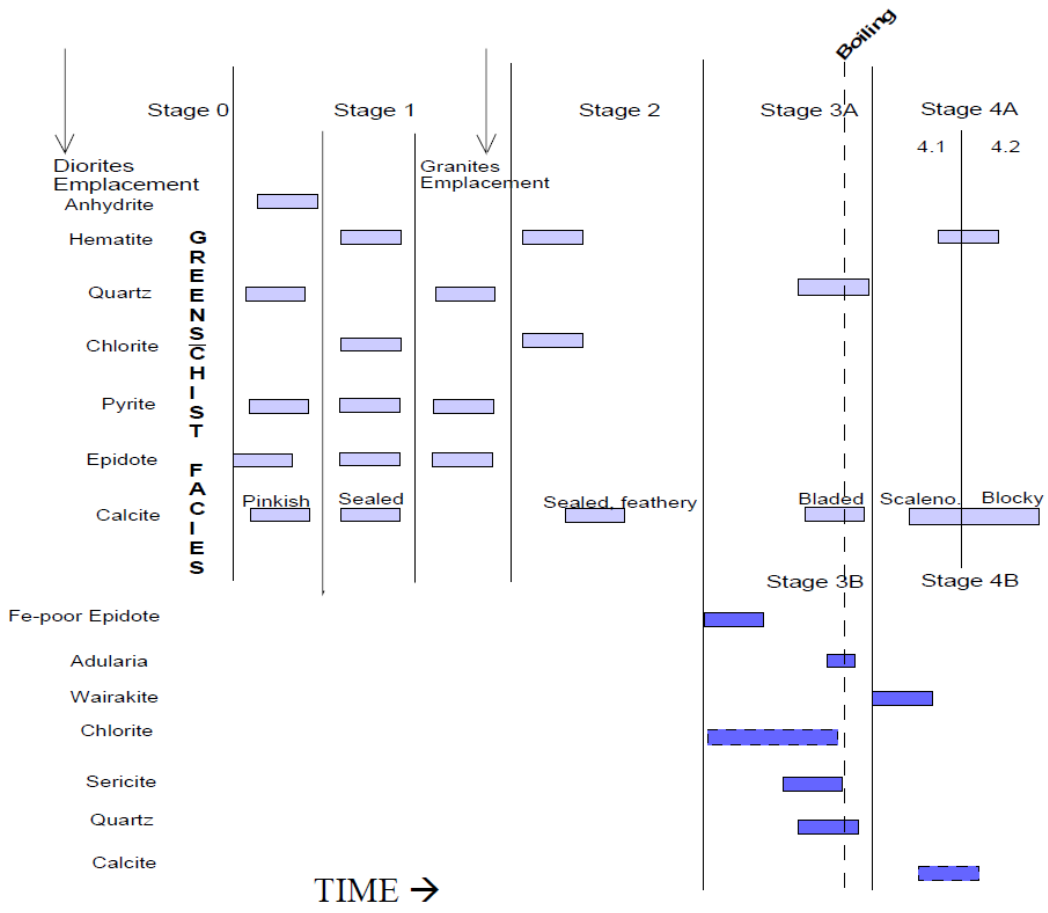

Figure 3. Paragenetic sequence of East Flank vein minerals showing 4 different alteration stages after greenschist facies metamorphism. Deep blue color refers to mineral assemblages in the deeper depths of Stages 3 and 4. (Kovac et al., 2005)

2.3.2 Fluid and Gas Chemistry

Predicting the evolution of the water-rock interaction of the geothermal system depends on knowledge of the fluid chemistry. A zone of superheated brines (H_2O), which extends from 8 to 12 km deep in the Coso geothermal region, was observed by Hauksson and Unruh (2007). The geochemistry of downhole water samples at Coso, California was

used to predict temperatures and characteristics beneath the surface. Fournier et al. (1980) discovered a body of uniformly chloride-rich hot water from two wells, and also estimated their reservoir temperatures at between 240-250°C in the vicinity of the Coso No. 1 well and about 205°C in the vicinity of the CGEH No. 1 well (both in the northern part of the map shown in Figure 1) using alkali cation and sulfate isotope geothermometers. The presence of a chloride-rich deep subsurface fluid at the Coso Geothermal system rather than a vapor-dominated system is concluded by Fournier et al. (1980), which is an important observation for aiding the interpretation of geophysical data and calculating the effectiveness of geothermal energy exploitation. Total dissolved solids range from 7,000-18,000 ppm. Non-condensable gases include air, helium, CO_2, and light hydrocarbons account for 6% of the gas fraction, of which 98% consists of CO_2 out of non-condensable gases. Hydrogen sulfide ranges from less than 10 to 85 ppm (Monastero, 2002).

2.3.3 Pore-Fracture System

Generally, fracturing and the development of permeability occur concurrently with the maturation of a geothermal system. An Enhanced Geothermal System (EGS) experiment at Coso caused a series of micro-earthquakes, which provide information about pre-existing and newly formed faults and hydraulic fractures. Julian et al. (2010) described the swarm of earthquakes activated as a result of an injection experiment, and that process is dominated by tensile failure. Moreover, the mineralogy and texture of faulted rock display a control on fluid flow and permeability together with the geometry of active faults in the geothermal field. Ultimately, chemical alteration along these

conduits leads to the breakdown of former minerals and the formation of alteration minerals such as clays, which can become fluid barriers (Davatzes et al., 2010). As shown by Anovitz et al. (2013), porosities of drill cutting samples from the Navy II well 42A-16 generally increase with depth, particularly for pore sizes between 1000 to 50,000 Å (100 nm to 5 μm), based on preliminary small- and ultra-small angle neutron scattering data. The pattern of increasing effective porosity with depth may indicate that deeper, hotter water-rock interaction preferentially creates porosity by the dissolution of some minerals and the closure of some pores as shallower depths by precipitation of secondary minerals (e.g. calcite).

Chapter 3: Methods

In order to interrogate a complex heterogeneous system such as Coso we employed a number of complementary methods to determine the mineralogy and the mineral-pore associations including standard Polarized Light Microscopy (PLM), Powder X-Ray Diffraction (XRD), scanning electron microscopy (SEM) with Energy Dispersive X-ray Spectroscopy (EDS or EDX) and Backscattered Electron Spectroscopy (BES), Quantitative Evaluation of Minerals by Scanning Electron Microscopy (QEMSCAN) , B.E.T. gas adsorption porosimetry, and Neutron Scattering (NS).

3.1 Sample Description

Thirty eight drill cutting samples, from 4 different wells at depths ranging from about 1000 to 9000 ft were obtained from Lawrence M. Anovitz of Oak Ridge National Laboratory (ORNL) and David Faulder, formerly of Terra-Gen Power. The Navy II well 42A-16 and the Navy II well 65A-18 are both production wells (Figure 1). Navy II well 56-16 is a well that is producing at a rate that is at the margin of profitability. BLNM well 83-11 is a non-productive well that can serve as a comparison to samples from the other three that exhibit different types of alteration and geophysical properties. The samples from each depth were homogenized and a sample splitter was used to divide approximately 5 grams of sample into four splits yielding as unbiased and representative

a sample as possible. A subset of some of these was prepared as standard thin sections by Spectrum Petrographic in Vancouver, Washington.

Prior to the grain splits described above, some of the cuttings had been blue-epoxy impregnated for the preparation of thick sections by researchers at ORNL. These thick sections (approximately 150 microns in grain thickness), were originally prepared for neutron scattering experiments, and were made available for this research by Dr. Anovitz.

3.2 Microscopy

A Leica DMS 1000 light microscope was used to select representative samples for thin section work and SEM/QEMSCAN study, mostly focusing on the samples from Navy II well 42A-16. This microscopy helped document the distribution of minerals with respect to depth and aided in determining properties such as the size range of grains, texture, and color.

The same thick sections that were analyzed by neutron scattering experiments for all Navy II well 42A-16, and some other wells have been subsequently analyzed using Polarized Light Microscopy (PLM) and Scanning Electron Microscopy (SEM) to confirm the primary rock types and to study the mineralogical evolution of the alteration minerals as a function of time – i.e., the paragenetic sequence of this system.

Standard thin sections (30 microns thick) of selected well cutting samples were prepared later to help support the mineralogy observations as determined by other methods. Thin sections of grain mounts were chosen based on interesting secondary

mineral assemblages at depth of 3000, 6000, and 9000 ft for Navy II well 42A-16, 56-16, and BLNM well 83-11, and at depth of 2000, 5000, 8000 ft for Navy II 65A-15. To overcome the limited quantity of samples, well cuttings (with individual grains averaging about 3 or 4 mm in dimension), which have been the challenges to characterize some of rock properties (specifically pore analysis), this research has utilized several analytical methods described below.

3.3 Powder X-Ray Diffraction (XRD)

A PANalytical X'Pert Pro X-ray Diffractometer, PDF 4+ database, and High Score Plus software were used to identify individual minerals and to semi-quantitatively determine their mass percentages in one split of each well cuttings sample. The samples were analyzed using randomly oriented powder mounts of approximately 1-2 grams of each sample. A mortar and pestle were used for grinding the samples. Powder mounts were scanned for a 2θ range of 5°-70° at a step size of 0.02° for 2 seconds/step. Semi-quantitative analysis calculates the estimated mass fractions of the acknowledged phases. The scale factor and the RIR (Reference Intensity Ratio) (Chung, 1974) values from the database are used to perform the calculation.

3.4 Scanning Electron Microscopy (SEM) and Quantitative Evaluation of Minerals by Scanning Electron Microscopy (QEMSCAN)

Scanning Electron Microscopy (SEM) uses a focused beam of electrons to produce a variety of signals at or the near the surface of solid samples. Two-dimensional SEM images have been acquired for selected Coso samples to obtain information about mineral textural relationships and mineral chemical composition. The latter is determined

using Energy Dispersive x-ray Spectroscopy (EDS) analysis of selected point locations on the samples. In addition, Quantitative Evaluation of Minerals by SCANning electron microscopy (QEMSCAN) allows automated high-resolution point counting of minerals and void spaces in a well-polished sample to create modal mineralogy. This has aided in determining the mineralogical compositions of the Coso samples targeted in this study. Thick sections of grain mounts previously analyzed using neutron scattering have been used for this analysis. Pixel counting is a limitation on the measurement precision when the pixel is on the phase boundary or a pit within minerals. In the former case, this assigns another mineral or others due to its similarity of chemical composition. For pits from grain plucking and other large surface scratches, signal is often deflected such that a reduced signal arrives at the EDS detector, and the mineral is not properly identified. Therefore, SEM, XRD, and PLM were employed complementarily to minimize error. Together, these methods aid in reconstructing mineral paragenesis. For the pore analysis, SEM data provides information to identify pore characteristics with respect to pore diameters and adjacent mineralogy, and helps to determine the association among pores/fractures and mineralogy.

3.5 Brunauer-Emmett-Teller (BET) Surface Area and Pore Size Analysis

Several methods are commonly used to determine specific surface area and porosity. The most widely used technique is the Brunauer–Emmett–Teller (BET) theory and equation, and the Barrett, Joyner, and Halenda (BJH) method, and equation, which involves physical adsorption and desorption of nitrogen gas molecules on the materials. These provide precise specific surface area, pore-size distribution, and connected pore

volume evaluation of materials. Therefore, it allows obtaining the average pore size in the material by the volume. Surface morphologies may be preliminarily studied using scanning electron microscopy (SEM). BET/N2 surface area and pore volume/size data have been collected and interpreted. All selected samples were first degassed in a degassing port at 120℃ using a Micromeritics ASAP 2020 apparatus for 2 hours prior to analysis.

3.6 Neutron Scattering (NS)

Neutron Scattering (NS) is a technique employed to characterize rock pore features and to quantify porosity in complex heterogeneous matrices. Small and ultra-small angle neutron scattering (SANS and USANS) are well suited in this study to probe the internal microstructure of the pore space over the range of nanometers to tens of micrometers. These techniques are used to detect all porosity, including connected and isolated pores, as compared to gas sorption analysis, which provides information on only connected pores. In USANS and SANS, a flux of neutrons has been used for pinhole experiment to determine the scattering contrast, which is derived from the difference in the coherent scattering length densities (SLD) of the rock and the pores (no scattering) within it by neutron beams (Anovitz et al., 2013). Unlike photons and electrons, thermal neutron beams are highly penetrating, with scattering occurring off of the interfaces between minerals and pores, hence a rock system can be treated as a two-phase system of matrix and pores.

Generally, SANS and USANS experiments do not cover the whole range of pore sizes in most of rocks. Thus, complementary method(s) may be needed to extend the

scattering curve beyond a few microns (see summaries of this method by Anovitz et al, 2011; 2013). BET method was used to compare porosities between different ranges of pore sizes, although BET measurement cannot detect disconnected pores.

Both SANS and USANS data were collected by L. M. Anovitz (ORNL) at the NIST center for Neutron Research (NCNR) using BT5 Perfect Crystal (USANS) and NG7 30 m small angle beam line (SANS) (http://www.ncnr.nist.gov/instruments). Coso samples from Navy II well 42A-16 are 150 μm thick sections consisting of polished epoxy-impregnated grains mounted on quartz glass slides. Samples were mounted on cadmium plates with 15.9 mm diameter apertures to outline the area of the incident beam (Swift et al, 2014).

3.7 Mercury Intrusion Porosimetry (MIP) and Micro-Computed Tomography (Micro-CT)

Pore analyses have been conducted using Mercury Intrusion Porosimetry (MIP) and Micro-Computed Tomography (Micro-CT) to aid the other pore analyses discussed above. MIP was used to determine pore connectedness for the sample from Navy II well 42A-16 at the depth of 1000-1010 ft. MIP is widely used to study porous materials, and determines the volume of mercury intruded into pore spaces at a number of pressure steps. Analyses were done on a Micromeritics AutoPore IV 9500 (software version 1.09). Micro-CT analysis was applied for scanning two individual well cuttings, one for a selected mafic grain and one for selected felsic grain, from Navy II well 42A-16 at the depth of 2000-2010 ft. While MIP shows only connected porosity by measuring pore-throats representing increasing pressure steps (higher pressures are necessary for smaller pore throats), micro-CT shows both connected and isolated pores and fractures, and is a

nondestructive method used to produce images of the pore network. Stacks of images obtained with micro-CT, processed by suitable software, can be used to create three-dimensional representations of the main objects of interest, which is powerful because damaged edges and boundaries in the samples can be excluded from the porosity calculation, to obtain more accurate porosity analysis.

Chapter 4: Results

4.1 Mineralogy

In this investigation, a semi-quantitative mineral analysis of all samples was made by powder XRD (Tables 1 through 4), supported by a more detailed assessment using QEMSCAN for the Navy II well 42A-16 (Appendix A) as a function of depth. Using both tools allows for more accurate result and reduces error, due to the fact that XRD provides phase identification based on crystal structure, and QEMSCAN shows visually mapped mineralogy using mineral standards based on EDS. Additionally, petrographic analysis was performed to confirm the mineralogy using Polarized Light Microscopy (PLM) with thin sections from selected samples. The common major constituent minerals identified in this study include quartz, plagioclase, K-feldspar, biotite, and amphibole. In addition, calcite, titanite (sphene), chlorite, and epidote are among the common minor mineral constituents in these samples.

4.1.1 BLNM Well 83-11: Non-Productive Well

Samples from BLNM well 83-11 contain most of the common minerals observed in samples from the production wells of Coso geothermal field, including quartz, plagioclase, K-feldspar, mica, chlorite, amphibole, calcite, and epidote together with accessory titanite, and iron oxide. A relatively greater quantity of titanite is detected with

XRD from three samples (depths 4390-5000 ft, 5990-6000 ft, and 6990-7000 ft) in this well (Table 1). At 6000 ft, the greatest amount of titanite is detected and decreases as the depth changes. Biotite is present at depth range 110 to 1000 ft, 4390-5000 ft, and 6990-7000 ft, but is absent at other depths. Iron oxides vary with depth from magnetite to goethite. Magnetite appears at 1990-2000 ft, 2990-3000 ft and 5990-6000 ft. Hematite is observed at 3990-4000 ft and goethite in samples collected from deeper in the well at 8990-9000 ft and 9470-9480 ft (Table 1). The presence of hematite and goethite may indicate that the addition of more oxidizing fluids circulated at depth in the system.

Table 1. Relative abundance (wt %) of minerals in BLNM well 83-11. Semi-quantification is based on RIRs from existing patterns in the PDF 4+ database.

Sample depths at BLNM well 83-11 (ft)	Qtz	Pl	Kfs	Mca	Chl	Am	Cal	Ep	Fe-ox	Ttn
100-110	16	65	14	2 ^{B,Ann}	-	3 ^{Mg}	1	-	-	-
990-1000	6	33	44	14 ^{B,M}	1 ^{Ch}	-	1	-	-	1
1990-2000	16	16	47	15 ^{M}	-	-	1	4	1 ^{Ma}	-
2990-3000	3	50	-	11 ^{M}	5	18 ^{Mg}	2	4	1 ^{Ma}	7
3990-4000	-	55	-	13 ^{M}	5	14 ^{Mg}	-	6	1 ^{He}	6
4390-5000	8	38	9	17 ^{B,M}	2 ^{Cl}	6 ^{Pr}	1	6	-	13
5990-6000	6	47	7	-	7 ^{Cl}	9	-	3	4 ^{Ma}	16
6990-7000	7	65	6	3 ^{B}	2 ^{Cl}	3	2	1	-	13
7990-8000	12	44	15	3 ^{P}	2 ^{Cl}	4 ^{Mg}	-	3	-	8
8990-9000	1	46	15	12 ^{M}	1 ^{Cl}	13 ^{Mg}	1	3	1 ^{G}	6
9470-9480	3	45	7	12	5 ^{Cl}	15 ^{E}	-	3	1 ^{G}	9

See Appendix B for Mineral abbreviations

Each superscript refers to a specific mineral in the group; Ann(annite), B(biotite), Ch (chamosite), Cl(clinochlore), E(edenite), G(goethite), He(hematite), M(muscovite), Ma(magnetite), Mg(magnesiohornblende), P(phlogopite), Pr(pargasite).

Table 2. Relative abundance (wt %) of minerals in Navy II well 56-16, Semi-quantification is based on RIRs from existing patterns in the PDF 4+ database.

Sample depths at NAVY II well 56-16 (ft)	Qt	Pl	Kfs	Mca	Chl	Am	Cal	Ep	F-ox	Ttn	Rt/A	Others
990-1010	14	12	34	13 ^{P,M}	4	10	1	3	<1 ^{Ma}	7	-	-
1990-2010	14	45	15	17 ^{B,M}	2 ^{Ch,Cl}	2 ^{Pr}	1	-	-	3	1 ^{Rt}	-
2990-3000	9	58	13	14 ^{B,M}	1 ^{Cl}	4 ^{Mg}	<1	1	-	-	-	<1 ^{Ccp}
3990-4000	13	21	18	38 ^{P,B,M}	2 ^{Cl}	3 ^{T}	<1	2	-	2	-	-
4990-5010	4	52	11	20 ^{P,M}	1 ^{Cl}	9 ^{Mg}	<1	2	-	-	-	-
5990-6000	6	61	4	4 ^{B}	3 ^{Cl}	19 ^{F,Ac,Pr}	-	3	-	-	-	-
6990-7010	10	41	34	10 ^{B,M}	3	1 ^{Pr}	1	-	-	-	<1 ^{A}	-
7990-8000	7	55	18	14 ^{B,M}	1 ^{Cl}	2 ^{Pr}	<1	2	-	-	1 ^{Rt}	1 ^{Crn}
8910-9010	9	38	20	24 ^{P,M}	3 ^{Cl}	3 ^{R}	1	2	-	-	<1 ^{Rt}	-
9970-9990	11	36	10	23 ^{P,M}	7 ^{Cl}	5 ^{F}	2	7	-	-	-	-

See Appendix B for Mineral abbreviations

Each superscript refers to a specific mineral in the group; A (anatase), Ac(actinolite), B(biotite), Ccp(chalcopyrite), Ch (chamosite), Cl(clinochlore), Crn(Corundum), F(Ferrotschermakite), M(muscovite), Ma(magnetite), Mg(magnesiohornblende), P(phlogopite), Pr(pargasite), R(richterite), Rt(rutile), T(tremolite).

Table 3. Relative abundance (wt %) of minerals in Navy II well 65A-18. Semi-quantification is based on RIRs from existing patterns in the PDF 4+ database.

Sample depths at Navy II well 65A-18 (feet)	Qtz	Pl	Kfs	Mca	Chl	Am	Cal	Ep	Ttn
980-1000	-	67	5	20 ^{P,B}	1 ^{Cl}	4 ^{R}	1	2	1
1970-2000	11	47	25	10 ^{P,B,M}	2 ^{Cl}	-	-	-	5
2970-3000	11	57	16	4 ^{B}	5 ^{Cl}	4	1	3	-
3970-4000	12	55	8	29 ^{B,M}	2 ^{Cl}	3 ^{R}	<1	1	-
4980-5000	10	54	10	19 ^{B,M}	2 ^{Cl}	3 ^{Ac}	-	1	-
5980-6000	7	56	7	22 ^{P,B,M}	2 ^{Cl}	5 ^{T}	<1	2	-
6970-7000	16	35	22	6 $^{P\ B}$	4 ^{Cl}	5 ^{Mg}	<1	7	4
7940-7970	11	33	14	33 ^{M}	2 ^{Cl}	5 ^{F}	<1	2	-

See Appendix B for Mineral abbreviations

Each superscript refers to a specific mineral in the group; Ac(actinolite), B(biotite), Cl(clinochlore), F(Ferrotschermakite), M(muscovite), Mg(magnesiohornblende), P(phlogopite), R(richterite), T(tremolite).

Table 4. Relative abundance (wt %) of minerals in Navy II well 42A-16. Semi-quantification is based on RIRs from existing patterns in the PDF 4+ database.

Sample depths at Navy II well 42A-16 (ft)	Qtz	Pl	Kfs	Mca	Chl	Am	Cal	Ep	Fe-ox	Ttn
1000-1010	11	66	5	4 ^{P}	6	4 ^{R}	2	2	-	-
2000-2010	11	54	12	13 ^{B,M}	5	4 ^{Mg}	1	-	-	-
3000-3020	23	44	20	7 ^{P}	3 ^{Ch}	-	3	-	1 ^{Ma}	-
4000-4020	7	39	36	3 ^{B}	1 ^{Ch}	7 ^{H}	-	-	< 1 ^{Ma}	7
5000-5020	9	36	8	24 ^{B,M}	8 ^{Cl}	4	3	4	1 ^{Ma}	2
6000-6030	10	63	9	8 ^{P}	3	3 ^{R}	-	-	1 ^{Ma}	3
7000-7020	4	49	27	16 ^{P,M}	1 ^{Cl}	2 ^{T}	1	-	-	-
8010-8040	5	44	18	24 ^{P,M}	5 $^{Ch, Cl}$	5 ^{Mg}	1	-	-	-
8900-8930	4	40	19	21 ^{B,M}	2 ^{Ch}	7 ^{Ac}	1	4	1 ^{Ma}	1

See Appendix B for Mineral abbreviations

Each superscript refers to a specific mineral in the group; Ac(actinolite), B(biotite), Ch (chamosite), Cl(clinochlore), H(hornblende), M(muscovite), Ma(magnetite), Mg(magnesiohornblende), P(phlogopite), R(richterite), T(tremolite).

4.1.2 Navy II Well 56-16: Marginal Production Well

For Navy II well 56-16, the mineralogy is similar to the other Coso wells in this study (Table 2). There is no strong mineral zoning but titanium dioxide (Figure 4), TiO_2, is observed as two polymorphs, rutile and anatase (approximately 1% by weight in the sample) from some of the depths, as identified by XRD. Rutile and anatase are both tetragonal but different [100] intensity peaks in XRD analysis; approximately 27.4° 2-Theta and 25.5° 2-Theta respectively. Even though it is a minor quantity, these polymorphs are good indicator minerals that may exhibit changes in temperature with depth in this well. While anatase is a metastable mineral, rutile is stable at relatively higher temperatures, so anatase has a tendency to transform to rutile at temperatures greater than about 480°C (Hanaor and Sorrell, 2011), and also anatase indicates either an acid or a neutral pH hydrothermal environment. Anatase is found at 6990-7010 ft and rutile is found at 1990-2010 ft, 7990-8000 ft, and 8910-9010 ft. Figure 4 shows that rutile (based on the XRD data for this depth) formed as a vein-filling product, which indicates the secondary vein-filling event occurred at high temperature (greater than 480°C). Another scenario for this rutile is that it is a primary mineral that was affected by metamorphism so that its crystal habit was modified, giving it an elongate shape. However, several needle-shaped rutile crystals within biotite cleavage planes were also observed, so it is more likely to be secondary mineral infilling cleavages in biotite by a thermal event. Also, magnetite was found only in the shallowest depth, 990-1010 ft, and is not detected in samples acquired from the other depth ranges.

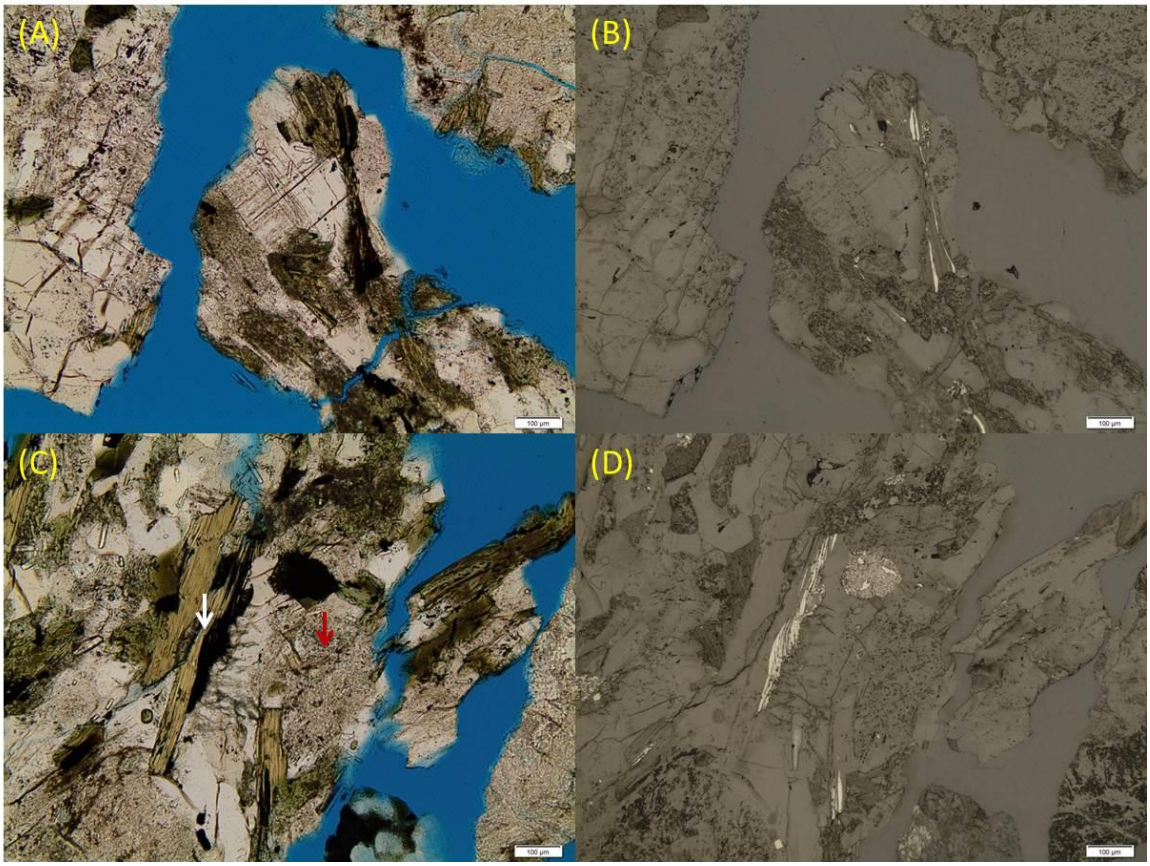

Figure 4. Plane polarized light (PPL) images and matching reflected light images from Navy II well 56-16 (8990-9010 ft) showing relatively low relief altered feldspar and biotite. Accessory rutile occurs as a vein filling product with dark red/black color in the PPL images (white arrow in (C)) and bright grey in reflected light images. Alteration to sericite, (cloudy fine-grained patches in silicates) is indicated by the red arrow in (C). Presumably, small needles of rutile formed as a result of a thermal event along the cleavage planes in biotite. Field of view is 1.3 mm.

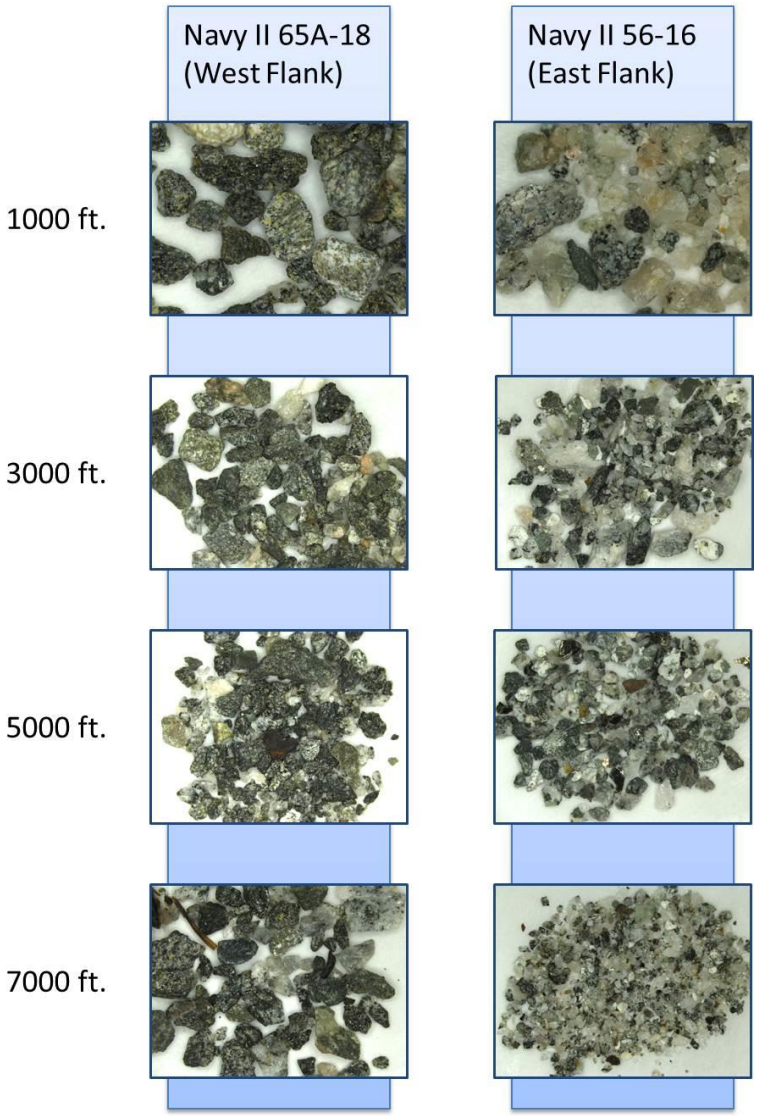

Figure 5. Comparison of well cuttings from the West (Navy II well 65A-18) and the East (Navy II well 56-16) flanks of the Coso Geothermal Field (location is available in Figure 1), showing that samples from the West Flank have more mafic minerals and much more extensive propylitic alteration.

4.1.3 Navy II Well 65A-18: Production Well

Navy II well 65A-18 (Table 3) is the only well located in the West Flank of the Coso geothermal field. Eight samples were obtained at approximately 1000 ft depth intervals. Amphibole and epidote were observed for all samples except a sample from 2000 ft depth, and chlorite is encountered in all eight samples. These minerals contribute to the green color observed for samples from this well, and chlorite is considered to be a secondary mineral caused by propylitic alteration (Figure 5). The propylitic mineral assemblage usually contains varying amounts of chlorite, epidote, illite and calcite in the presence of fresh or weakly altered feldspar crystals as the result of low- to moderate pressure-temperature alteration (Bove et al., 2007).

In the amphibole group, actinolite and tremolite are calcic amphibole end members that form an Fe-Mg solid solution series. Actinolite is the Fe-rich end member, whereas tremolite is the Mg-rich end member. The amount of iron varies among specimens, causing different intensities of green in pleochroism observed in PPL (plane polarized light). More iron will tend to give a specimen a darker color. Changes in amphibole species at different depths are observed by XRD in this well, and may indicate changes in fluid composition. Actinolite is a very common amphibole in medium-grade metamorphic rocks. Tremolite, which is observed in depth of 5980-6000 ft in this well by XRD, is commonly but not always found in carbonate-rich metamorphic rocks in contact metamorphic zones. Also these minerals are common hydrothermal minerals that indicate a formation temperature greater than 280°C (Reyes, 1990). Figure 6 shows an

intergrowth of plagioclase and amphibole which is a characteristic of metamorphic texture.

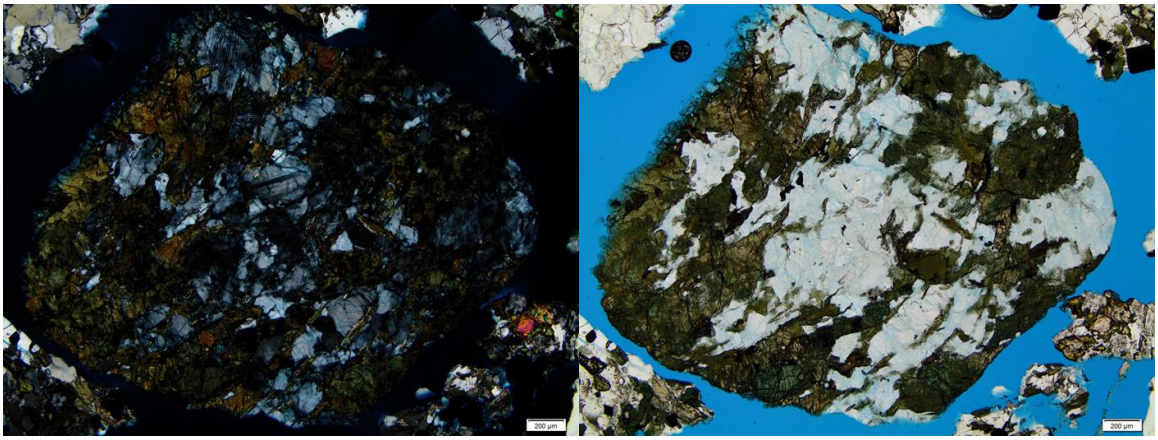

Figure 6. Cross-polarized light (XPL) (left) and plane polarized light (PPL) (right) images showing intergrowth of amphibole and plagioclase which is a metamorphic texture at Navy II well 65A-18 4980-5000 ft. Strong pleochroism of amphibole may indicate hornblende. Field of view is 3.5 mm

Out of eight samples in Navy II well 65A-18, a sample from 4980-5000 ft was chosen (the most extensively altered sample observed by Leica DMS 1000 light microscope) to perform a detailed petrographic study including light microscopy, SEM and mineral mapping analysis. The major minerals include quartz, plagioclase feldspar, K-feldspar, and biotite, which comprise nearly 85% of total mineral volume (as counted by QEMSCAN pixels to yield modal mineralogy). A fine-grained micrographic intergrowth of quartz and plagioclase feldspar is shown in **Figure 7**, interpreted as the

last product of crystallization in some igneous rocks which contain high or moderately high percentages of silica, and may represent residual melt. Commonly it has no definite form of its own, but fills up the irregular interstices between the earlier crystallized minerals. The compositions of these residual crystallization products may represent eutectic compositions, the mixtures (quartz plus feldspar plus minor amounts of other minerals) that have the lowest fusion point.

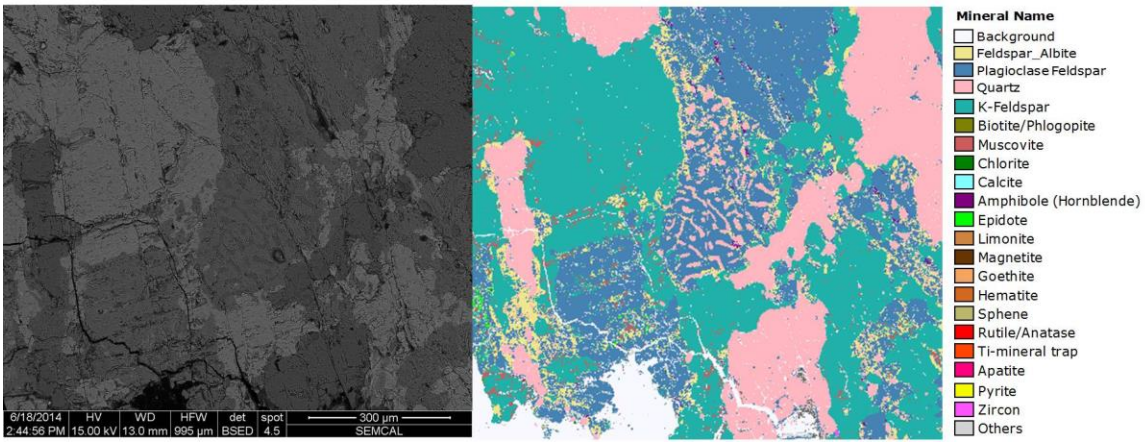

Figure 7. BSE (left) and corresponding QEMSCAN (right) images showing myrmekite which is micrographic intergrowth of plagioclase and quartz (symplectite of quartz in plagioclase) (Passchier and Trouw, 1996) at Navy II well 65A-18 4980-5000 ft.

In addition to major minerals, several minor minerals are also observed by SEM in Navy II well 65A-18 (4980-5000 ft). These include epidote contained a rare earth element (REEs) apparently replacing titanite (Figure 8), which is not observed in Navy II well 42A-16. While mineral mapping data show cerium in the epidote, EDS analysis

confirms the presence of lanthanum and neodymium in addition to cerium. In contrast epidotes in Navy II well 42A-16 (East Flank) are generally iron-rich, whereas the REE-epidote is rare but is identified either localized in one well (Navy II well 42A-16; 2000-2010 ft), or more disseminated (Navy II well 42A-16; 8010-8040 ft).

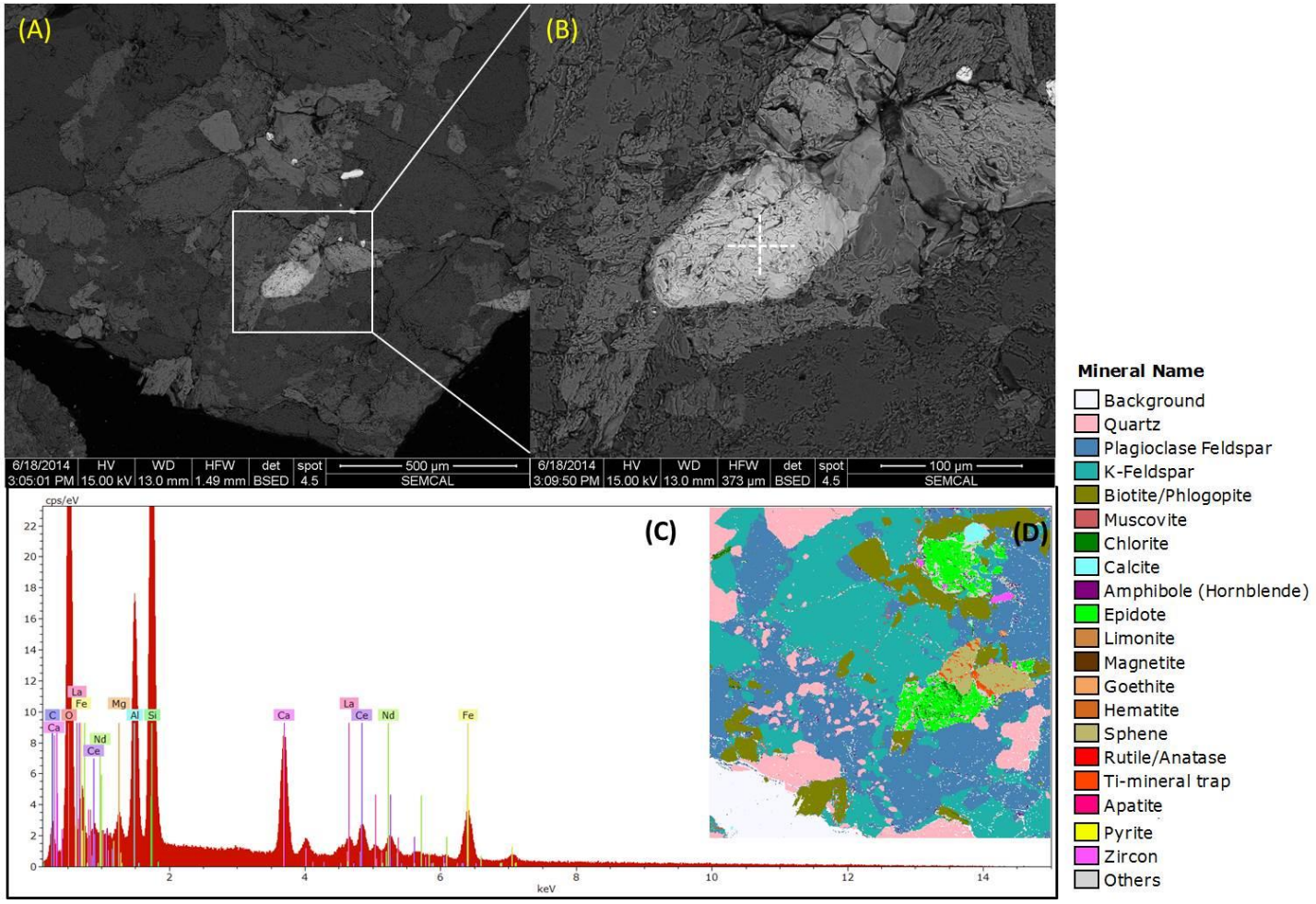

Figure 8. REE-bearing epidote replacing titanite and biotite in Navy II well 65A-18 4980-5000 ft. The white rectangle delimits the close-up in B.

Minor titanite, apatite, and zircon are also found at 4980-5000 ft in Navy II well 65A-18 (Figure 9). Zircon is usually a primary crystallization product in igneous or metamorphic rock. Apatite exhibits several types of textural and mineral assemblage associations. In some cases apatite grains formed after biotite displaying cross-cutting relationships as shown in Figure 9. Other occurrences include precipitation in vugs supporting the idea that apatite is a secondary mineral. Some apatite grains (i.e. below right side of second image in Figure 9) occur as euhedral crystals, which may indicate that they are either a primary or secondary mineral phase.

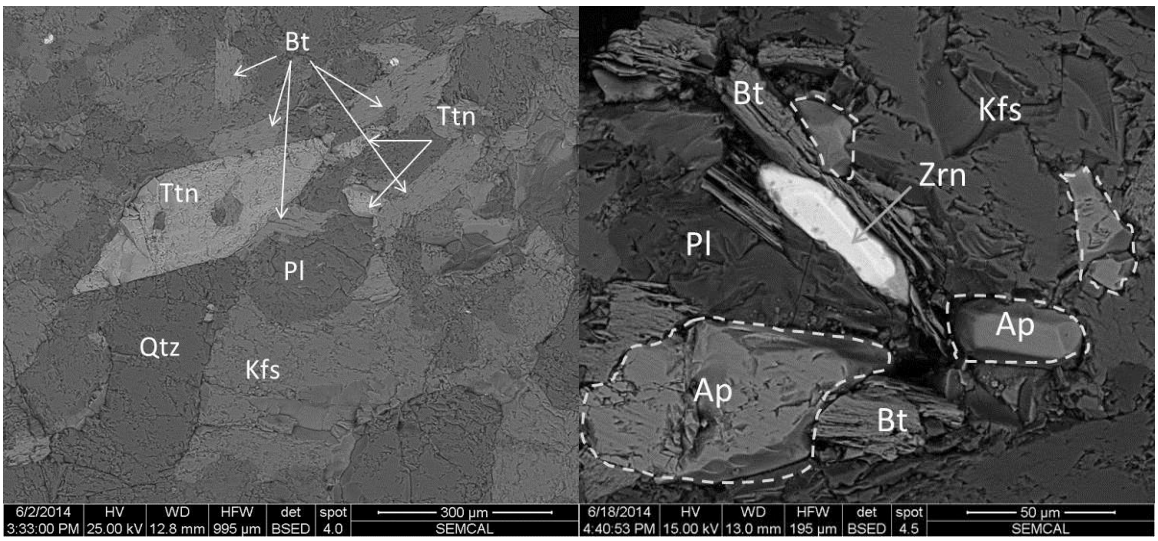

Figure 9. Accessory (minor) minerals including wedge- and elongated rhomb-shaped titanite (left), zircon, and apatite crystals (right) in Navy II well 65A-18 4980-5000 ft. List of Mineral Abbreviations is given in Appendix B.

4.1.4 Navy II Well 42A-16: Production Well

Samples analyzed from Navy II well 42A-16 with both XRD and QEMSCAN show that the most common minerals include plagioclase, potassium feldspar, quartz, and biotite, which are the main constituent of quartz diorite and granodiorite host rocks (Table 4). According to formation log information from this well (Jess McCulloch, TerraGen, pers. comm.) lithology varies with depth from diorite to quartz-diorite and granodiorite. In shallower depths between around 1000-4020 ft granodiorite and quartz diorite are the dominant rock types. At 3000-3020 ft granite (23%) occurs with quartz diorite (77%). At 5000-5020 ft quartz diorite (55%) and diorite (35%) are present, and then at 6000-6030 ft diorite is the most dominant (81%). At 7000-8930 ft, quartz diorite is dominant rock type (more than 97%). Our observations based on petrographic studies are very similar to the lithologies identified from the log data but in addition we find abundant mica schist grains at 6000-6030 ft which is the most common rock type in this sample (Figure 10). The random orientation of biotite implies that these are post-tectonic and grew after formation of the schistose fabric. Furthermore, calcium silicate is also found (approximately 10%) in this depth at 6000-6030 ft. This calcium silicate has a lot of sphere pores and partially filled with calcite. Supposedly these grains may be amorphous silica (perlite) altered by carbonate bearing fluid.

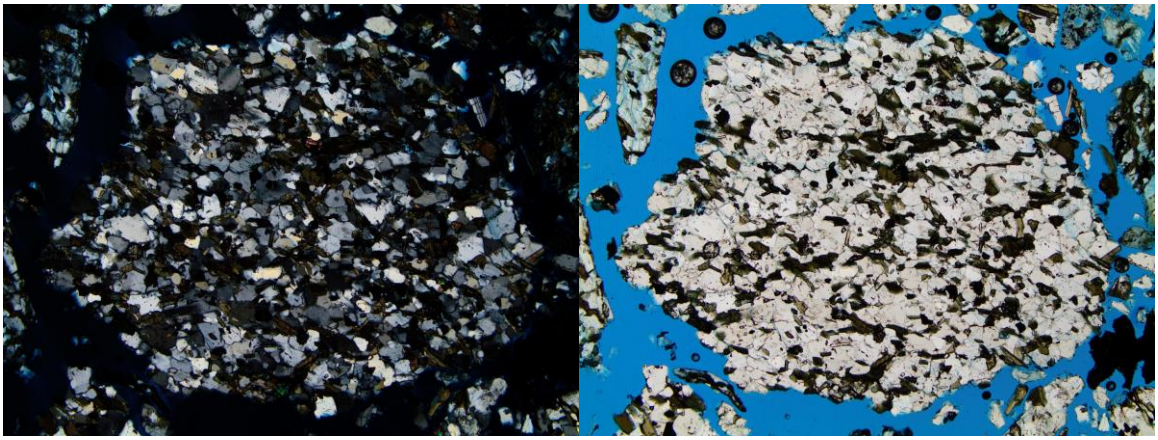

Figure 10. XPL (left) and PPL (right) images showing relatively clean and less altered plagioclase, quartz, and sub-parallel oriented grains of biotite. This is the low-grade mica bearing schist (Ernst, 1963), and is one of the most common types of rock in the 6000-6030 ft depth sample from Navy II well 42A-16. Field of view is 3.5 mm

In deeper portions of this well (from approximately 7000 to 8930 ft) a greater amount of amphibole is present (~14%) as compared to shallower depth (~5%). Also, muscovite is dominant in the depth range from 2000 to 2010 ft, and sericite is encountered in every sample, but is particularly abundant in the depth range from 5000 to 5020, where it exhibits distinctive alteration textures. According to QEMSCAN analysis (Appendix A), iron oxide is more abundant in deeper samples mostly as a form of limonite and goethite; specifically 8010-8040 ft and 8900-8930 ft. Conversely, calcite is the most abundant in the shallowest depth (1000-1010 ft). Although the extent of heterogeneity encountered in many of the Coso samples is great, some trends of mineralogy can be seen (Figure 11).

Figure 11. Light microscope images of well cutting samples from Navy II well 42A-16, illustrating some trends of mineralogy with depth. Grains identified include black biotite, dark-gray hornblende, off-white plagioclase, and translucent gray quartz. Chloritization is present (5000-5020 ft), as well as yellow iron oxide staining (6000-6030 ft), and multiple alteration is identified at deeper depth range.

Chloritization is evident at 5000-5020 ft (green phyllosilicate), iron oxide (yellow staining) at 6000-6030 ft, and more extensive multiple alteration types occur in deeper samples (8010-8040 ft and 8900-8930 ft). Iron oxides tend to occur as single fragments (grains) in the deeper samples, but they have a tendency to be adjacent to and still form grain boundaries with other minerals in the 6000-6030 ft depth sample (including plagioclase, quartz, biotite, and apatite). Some single grains of iron fragments were detected by QEMSCAN that are actually iron filing contamination resulting from well boring. Apatite generally occurs as clear stubby or slender prisms light optically, and concentrates rare earths, especially the middle REE, and may concentrate scandium, yttrium, uranium, and thorium. Samples from this well are selected for SEM and QEMSCAN analysis with an emphasis on alteration characterization.

4.2 Alteration

In a geothermal environment, primary minerals tend to alter to different secondary minerals, depending on reservoir temperature, pressure, and fluid-rock composition. In the Coso geothermal field, the reservoir rocks on the East Flank are dominated by diorite, quartz diorite, and granodiorite with a few intervals of granite and schist. The granite is likely to be much less altered, veined, and fractured than the other rock types, and consequently probably a poor hydraulic stimulation target (Kovac et al., 2005). Petrologic study by Kovac et al. (2004) summarizes the relative ages of these rock types: the diorite and the quartz diorite are the oldest of the reservoir rocks, the granodiorite is intermediate in age, and granite is the youngest of the three rock types. In Navy II well 42A-16, granite occurs extensively at approximately 3000-5020 ft, but is not encountered at other

depth ranges in the samples. Hydrothermal alteration minerals appear both as replacement of the primary minerals as well as fillings in vesicles, vugs and fractures throughout the well. In this effort, the alteration mineralogy and its distribution were obtained from standard light optical methods and the SEM which included detailed EDS mineral mapping.

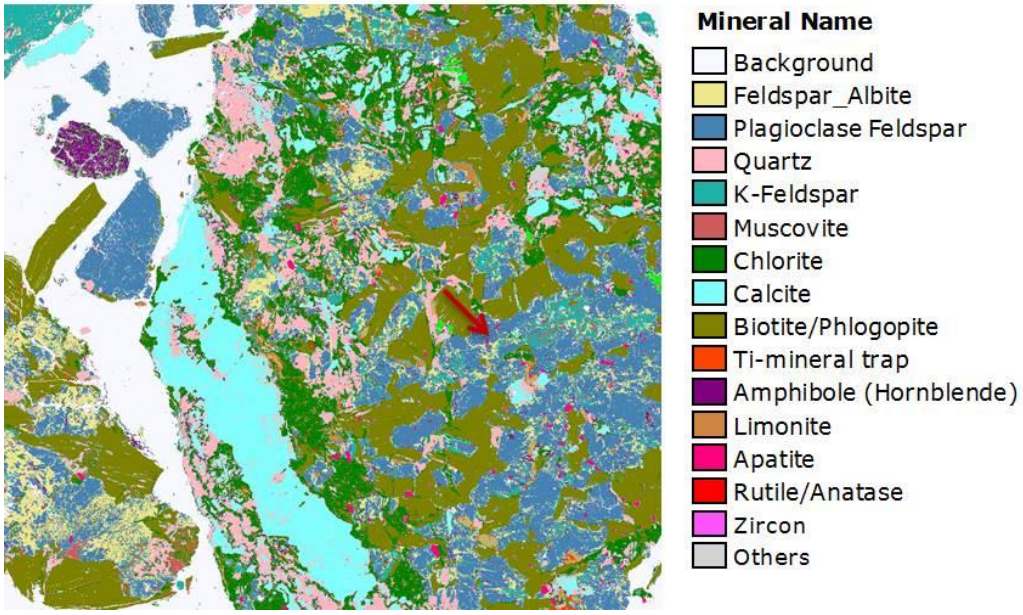

Figure 12. This QEMSCAN mineral map from Navy II well 42A-16 (depth 4000-4020 ft) shows several alteration types, including albitization, chloritization, and carbonate alteration. Red arrow is the region showing hydrothermal albite along with potassium feldspar. Field of view is 2.0 mm.

In general terms alteration of primary minerals occurs throughout the depth ranges of samples from the Coso wells we studied, but some are unique to specific depth

ranges. Seven alteration facies are recognized: 1) albitization 2) potassic alteration 3) sericitization, 4) propylitic alteration, 5) carbonate alteration 6) silicification, and 7) oxidation.

4.2.1 Albitization

Hydrothermal albite is an alteration mineral that preferentially replaces plagioclase (Figure 12). For example, albite forms by reaction of silicic acid and sodium ion with calcium plagioclase (Merino, 1975):

$$NaAlSi_3O_8 \cdot CaAl_2Si_2O_8 + H_4SiO_4 + Na^+ = 2NaAlSi_3O_8 + Al^{+3} + Ca^{+2} + 4OH^- \quad (1)$$

All samples from Navy II well 42A-16 include secondary hydrothermal albite, which is also often associated with potassic alteration. This is typically due to fluids that have lost potassium ions by potassic alteration and gained sodium ions. For that reason hydrothermal albite often occurs along grain boundaries of potassium feldspar which suggests that it is a secondary phase as shown in Figure 12 (red arrow).

4.2.2 Potassic Alteration

Hydrothermal alteration resulting from potassium metasomatism commonly accompanied in calc-alkaline rocks by removal of calcium and sodium. Potassic alteration, which is characterized by the replacement of primary minerals with secondary K-feldspar, biotite or chlorite, sericite, and quartz, is commonly associated with albite, anhydrite, Fe-Mg carbonate, apatite, sulfides (pyrite, chalcopyrite) and magnetite (Bashar and Garba, 1999). Specifically, potassic alteration results in the formation of micaceous, potassic minerals such as biotite in iron-rich rocks, muscovite mica or sericite in felsic

rocks, and potassium feldspar (orthoclase, adularia, and microcline). Thus, potassic alteration has a strong relationship with albitization and sericitization in composition. In Navy II well 42A-16 at 5000-5020 ft, extensive potassic alteration was observed with sericite and accessory minerals including iron oxides, pyrite, monazite, and anhydrite (Figure 13).

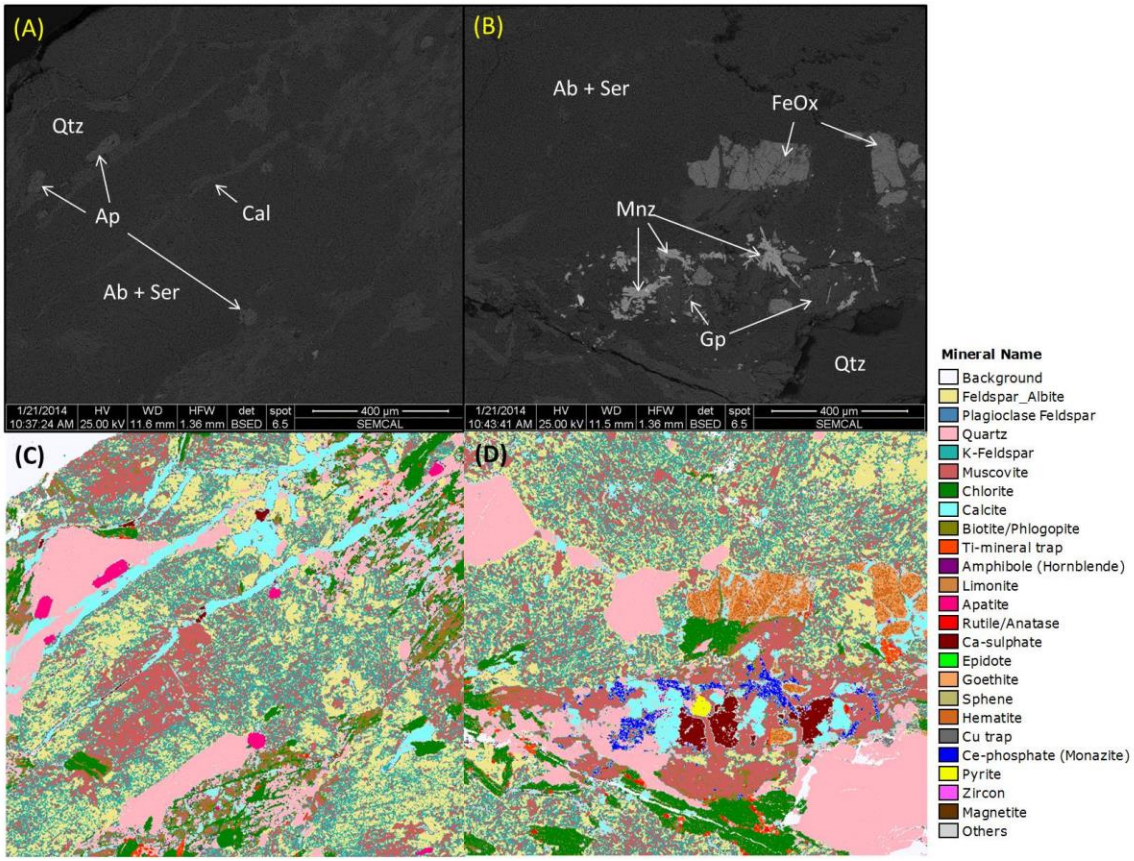

Figure 13. BSE images and matching mineral maps showing secondary alteration in Navy II well 42A-16 (5000-5020 ft). Secondary sericite and albite are apparent, as well as a calcite veining event.

4.2.3 Serictization

Sericitic alteration typically involves primary feldspars converted to the mineral sericite, which is very fine grained white mica formed by reaction below (Que and Allen, 1996).

$$(xNa, yCa)AlSi_3O_8 + K^+ + Na^+ + Fe^{+3} + Mg^{+2} + H_2O \rightarrow$$

$$(K, Na)_2(Al, Fe, Mg)_4Si_6O_{20}(OH)_4 + (x{+}mNaAlSi_3O_8, y{-}mCaAlSi_2O_8) + 2mCa^{+2} \qquad (2)$$

Sericite is observed as a fine dust-like (dotted) appearance on plagioclase or K-feldspar (Figure 14). It is encountered in nearly every sample but is less abundant in granites, which tend to be less altered as compared to other rock types. In particular, Navy II well 42A-16 (5000-5020 ft) exhibits the most abundant sericitization, together with larger-grained secondary muscovite, which also is associated with potassic alteration (Figure 13). Sericitic alteration implies lower pH (acidic) conditions (Lagat, 2007). In the legend for QEMSCAN mineral maps, muscovite refers to muscovite as well as a proxy for K-mica (sericite).

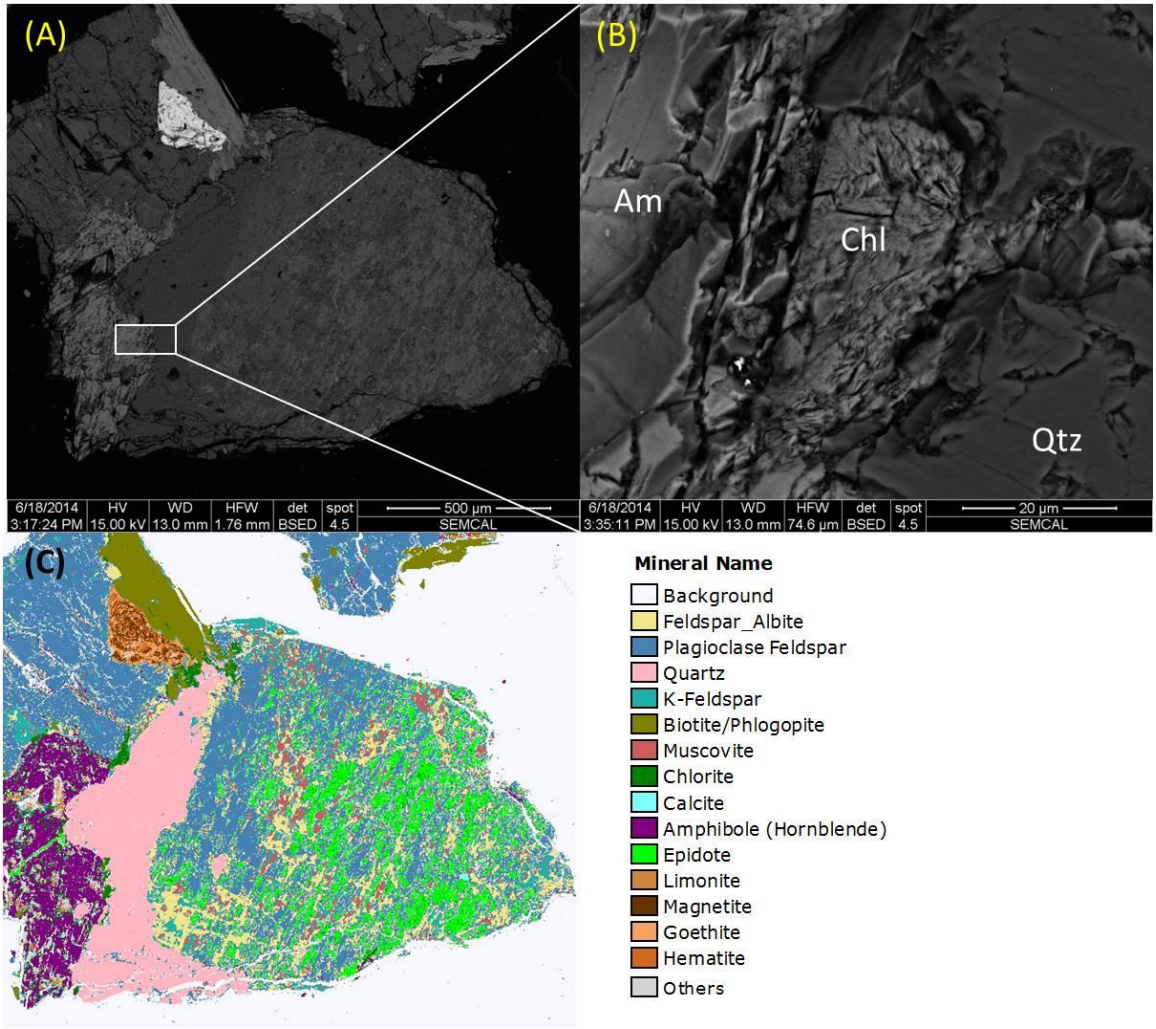

Figure 14. BSE images and a matching QEMSCAN mineral maps from Navy II well 65A-18 (4980-5000 ft). (A, C): Epidotization and serictization along with albitization of plagioclase is observed. Chlorite is found along grain boundaries formed between quartz and amphibole, plagioclase, and biotite. (B): Higher magnification image of portion of (A) showing chlorite occurs along the boundary between quartz and amphibole.

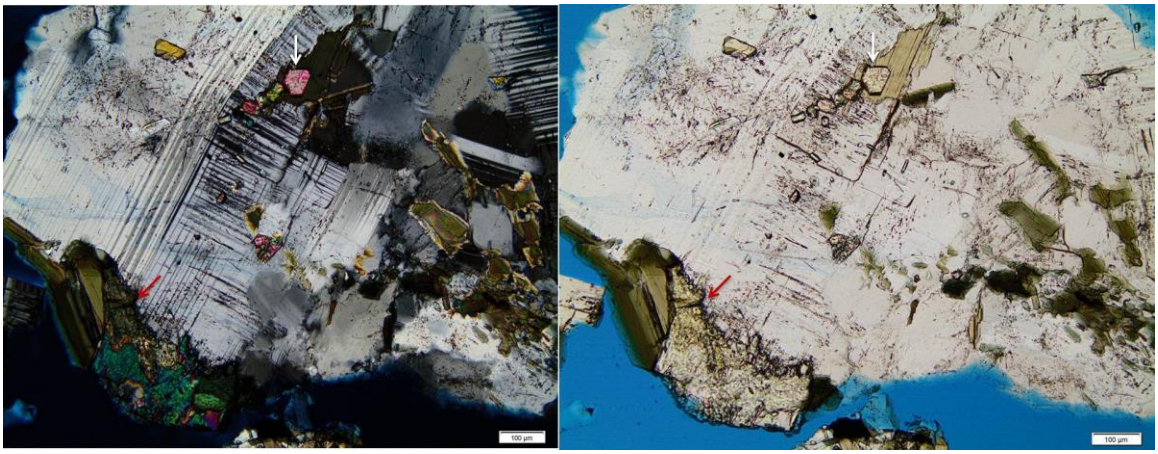

Figure 15. XPL (left) and PPL (right) images from Navy II well 65A-18 (4980-5000 ft) showing the poikilitic texture (upper center) of epidote in K-spar and biotite (white arrow) which is a common texture in igneous and metamorphic rocks, and epidotization of biotite (lower left corner). The biotite also is altered to chlorite (red arrow). Field of view is 1.3 mm.

4.2.4 Propylitic Alteration

Propylitic alteration turns rocks green, because the secondary minerals associated with this type of alteration (including chlorite, epidote, actinolite, and tremolite), are green. In the Coso geothermal system, propylitic alteration is caused by iron- and magnesium-bearing hydrothermal fluids replacing feldspar (Figure 14), or the decomposition of Fe- and Mg-bearing minerals such as biotite (Figure 15, Figure 16, and Figure 17), and amphibole (Figure 18). For example, one possible chemical reaction is tremolite reacting with albite to form clinozoisite and clinochlore (Reed, 1997):

$$Ca_2Mg_5Si_8O_{22}(OH)_2 + 5NaAlSi_3O_8 + 5H^+ + H_2O$$

(tr,ss) (ab) (aq) (aq)

$$\leftrightarrow Ca_2Al_3Si_3O_{12}(OH) + Mg_5Al_2Si_3O_{10}(OH)_8 + 5Na^+ + 17SiO_2 \quad (3)$$

(cz, ss) (clchl, ss) (aq) (aq)

where ‘ss’ refers to solid solution and ‘aq’ to an aqueous constituent. It is not uncommon to observe epidote–chlorite–quartz as distinct clusters, veins or fracture fillings along with pyrite. Chlorite is widespread, occurring in every sample in Navy II well 42A-16 (Figure 12, Figure 13) and also is observed in other wells studied except the sample from the non-production BLNM well at 100-110 ft and 1990-2000 ft.

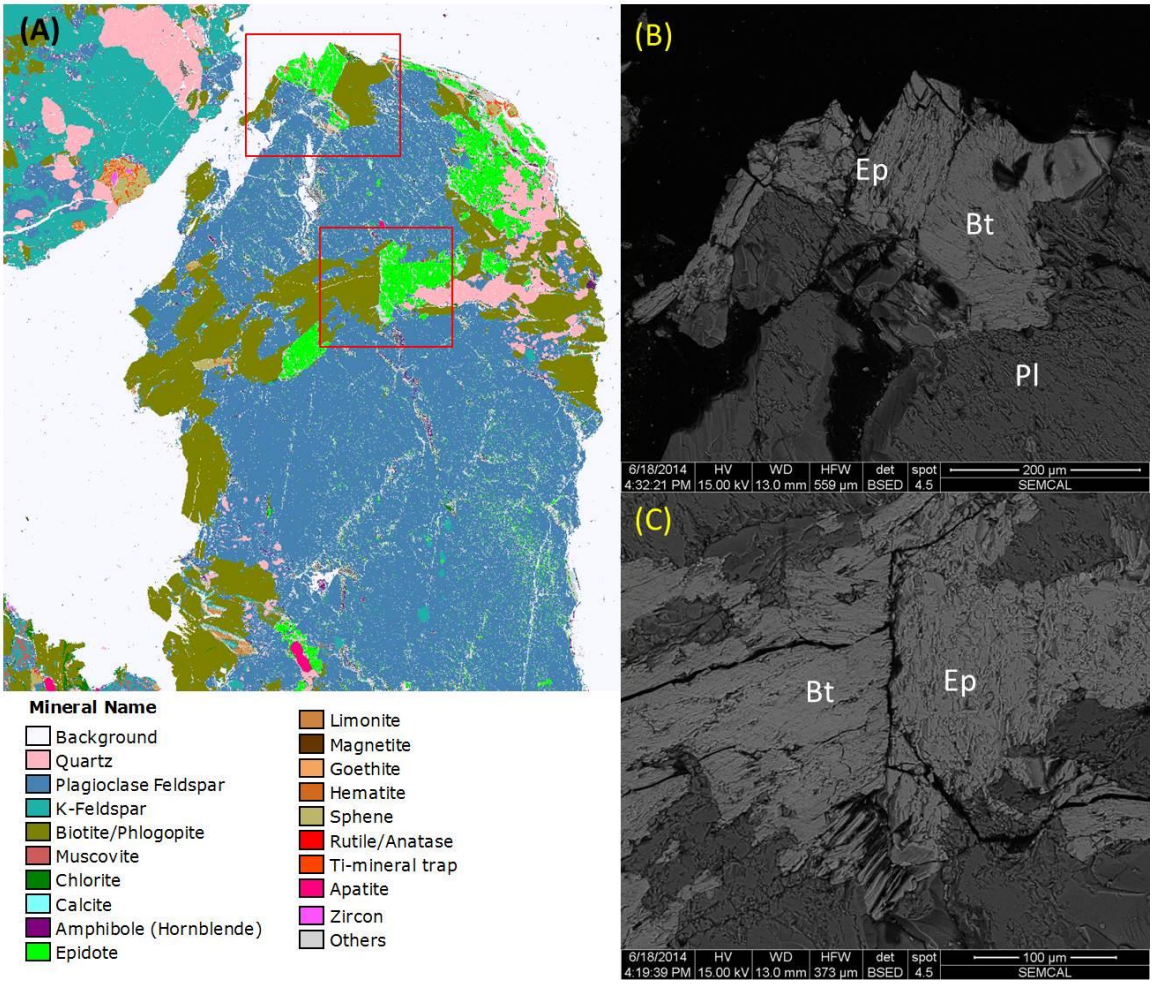

Figure 16. BSE images and a matching QEMSCAN mineral map from Navy II well 65A-18 (4980-5000 ft) showing secondary epidote associated with biotite. The red rectangles delimit the close-up images (B) and (C).

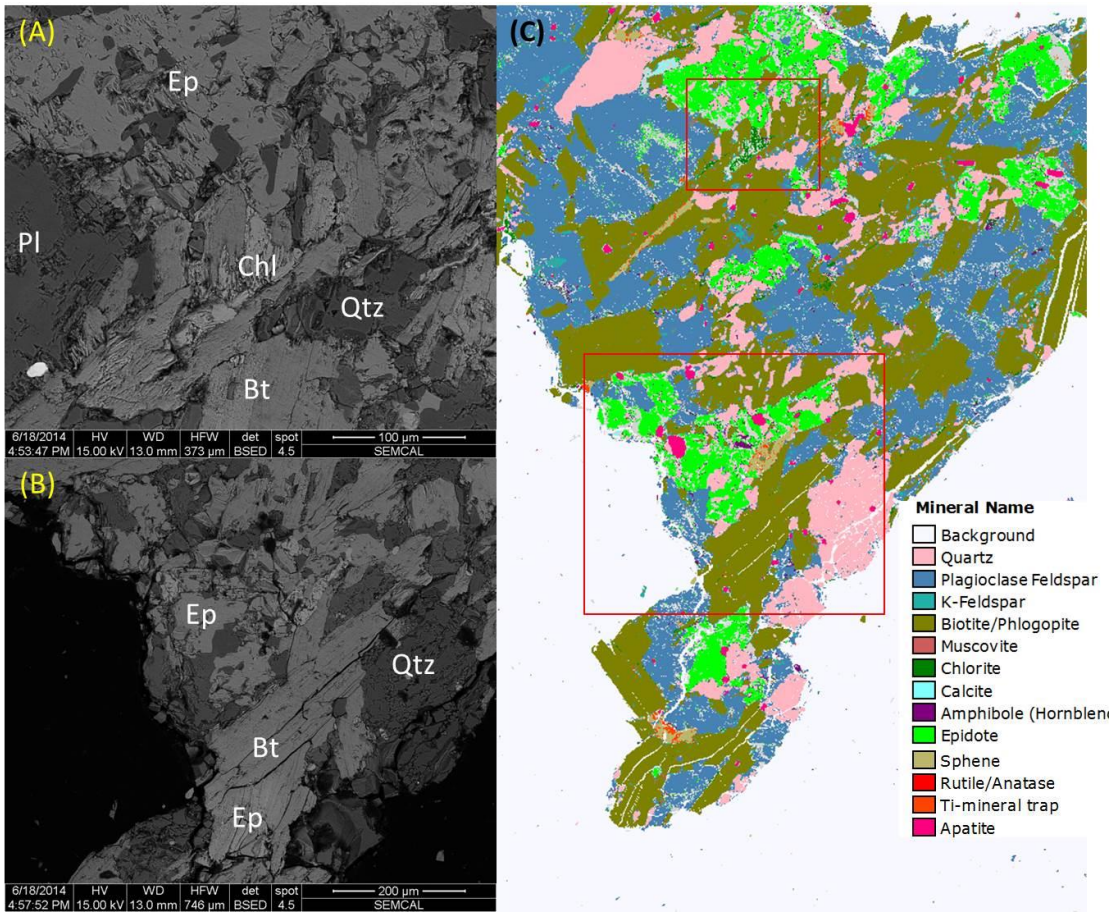

Figure 17. BSE images and a matching QEMSCAN mineral map from Navy II well 65A-18 (4980-5000 ft), showing secondary epidote after quartz and biotite. Red rectangles delimit the close-ups images (A) and (B). (A): Secondary epidote, and fibrous chlorite along a fracture in biotite. (B): Secondary epidote, apatite, and sphene (titanite).

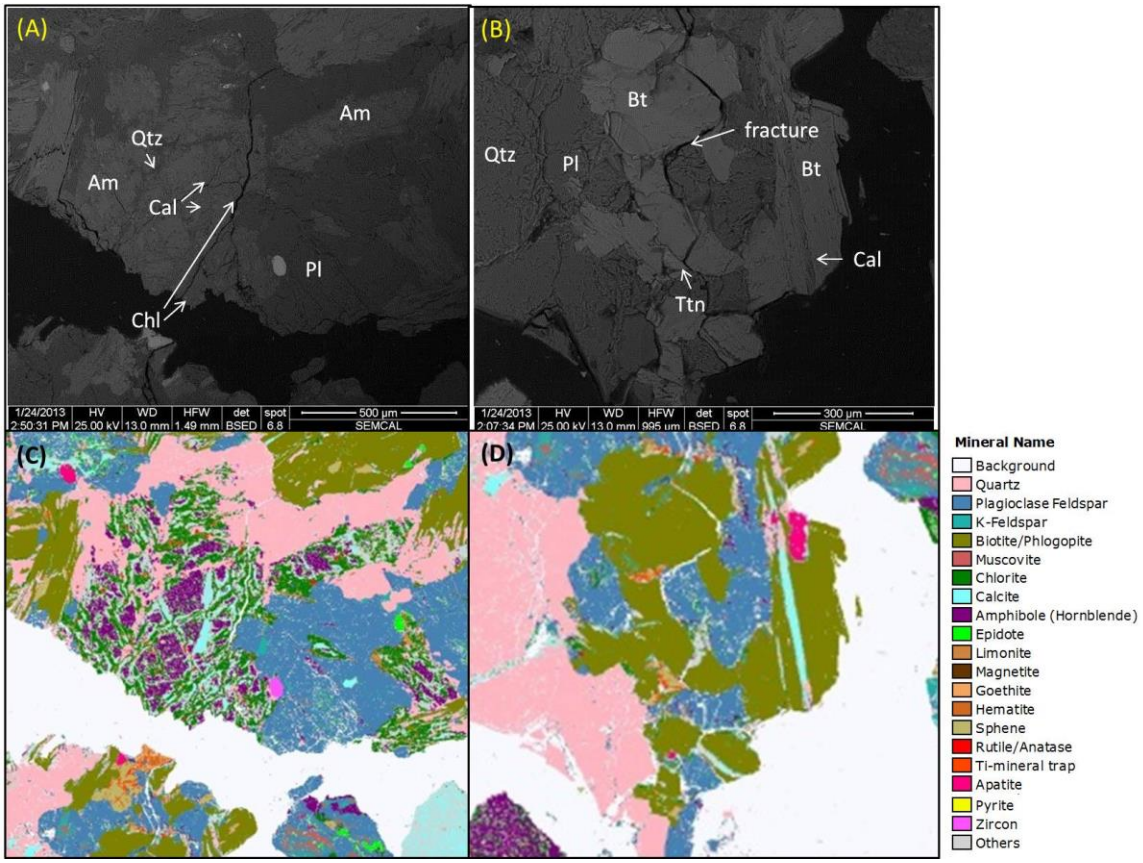

Figure 18. BSE images and matching QEMSCAN mineral maps from Navy II well 42A-16 (1000-1010 ft) show several alteration types. (A, C): secondary sphene (titanite) occurs along fractures and cleavage planes of biotite. Quartz, chlorite and calcite veins cut across an extensively altered amphibole grain. (B, D): secondary calcite fills space between cleavage planes within biotite grains.

4.2.5 Carbonate Alteration

Secondary carbonate is found in every depth from the Navy II well 42A-16, and is the most abundant vein mineral. Calcite veins are more abundant in the shallowest depth sample (1000-1010 ft), as shown in Figure 18. In other wells, carbonate veins also are observed, but they are volumetrically less important when compared to the shallowest

depth sample (~7.5% in volume from QEMSCAN data). In deeper wells, calcite veins are strongly associated with quartz crystals and also quartz veins (Figure 19). Calcite replaces quartz and plagioclase, and locally extends across entire grains in cutting (Figure 20, Figure 21). Calcite veins commonly fill fractures, cleavage planes, and pores in mineral grains of the Coso samples. In addition, most of the calcite has a strong association with chlorite when it is adjacent to biotite (Figure 20).

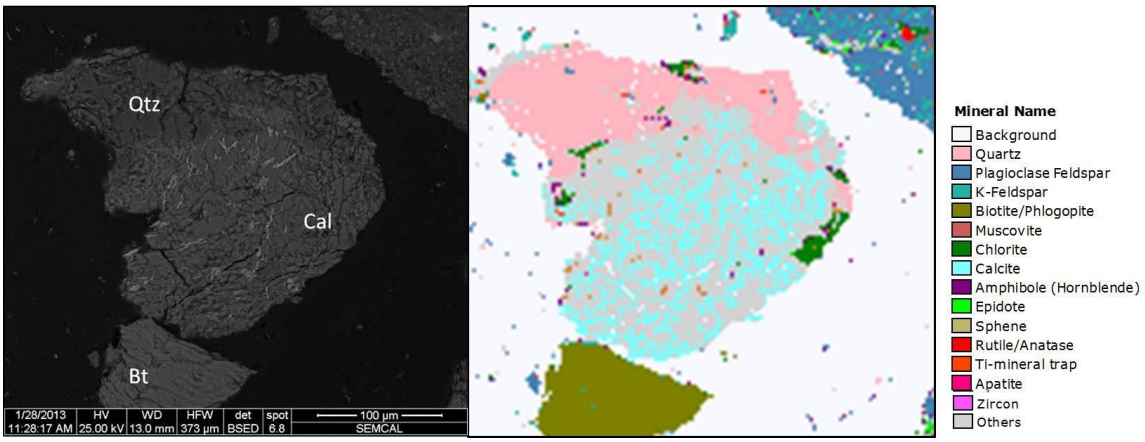

Figure 19. BSE image and matching QEMSCAN mineral map from Navy II well 42A-16 (7000-7020 ft), showing quartz grain with calcite alteration. In the BSE image (left), acicular iron-antimony oxide (iron antimonate) is observed 'Others' in the legend also includes calcite and calcium silicate.

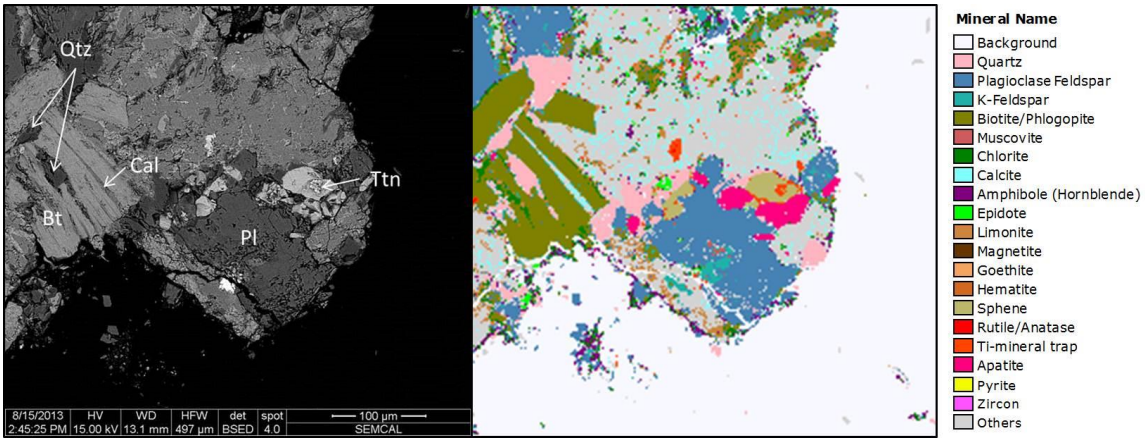

Figure 20. BSE image and matching QEMSCAN mineral map from Navy II well 42A-16 (4000-4020 ft), showing calcite veins along cleavage planes of biotite, and "calcium silicate" observed over quartz (legend indicates calcium silicate as 'others' here)

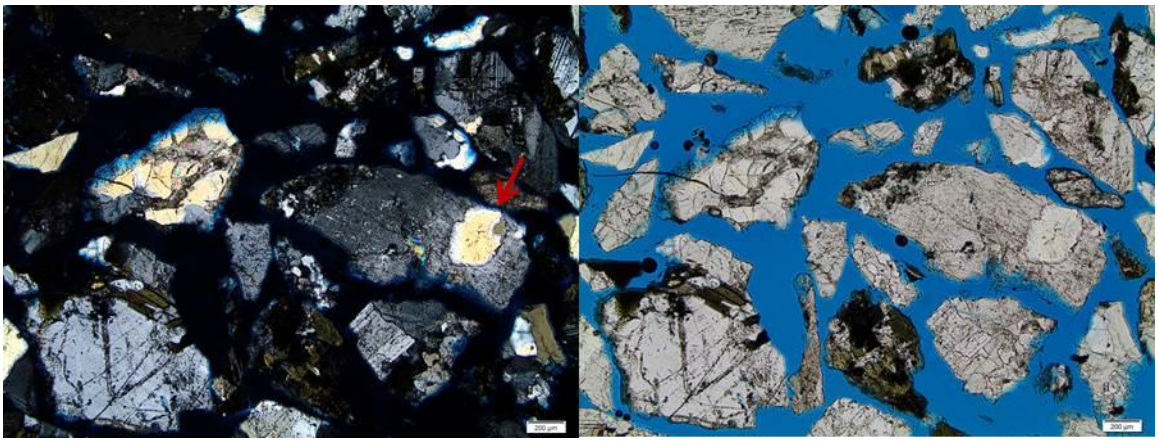

Figure 21. XPL (left) and PPL (right) views from Navy II well 42A-16 (3000-3020 ft), showing a rounded phenocryst of quartz (arrowed), and calcite veins filling fractures of minerals (lower left corner). Field of view is 3.5 mm.

4.2.6 Silicification

Silicification is the addition of secondary silica that is encountered in nearly every sample. Generally this results in the formation of fine-grained quartz, chalcedony or opaline silica, which may fill pores and replace existing minerals (Bustillo, and Alonso-Zarza, 2007). Abundant quartz veins are observed together with calcite veins in Navy II well 42A-16 (7000-7020 ft and 8900-8930 ft), and also silica replacement is detected from characteristic X-ray analysis of the iron oxides (magnetite), but QEMSCAN detected this iron oxides as mixed layers of limonite and goethite (Figure 22) On the other hand, in the sample from depth (1000-1010 ft), quartz veins are volumetrically less important, and calcite veins are much more abundant.

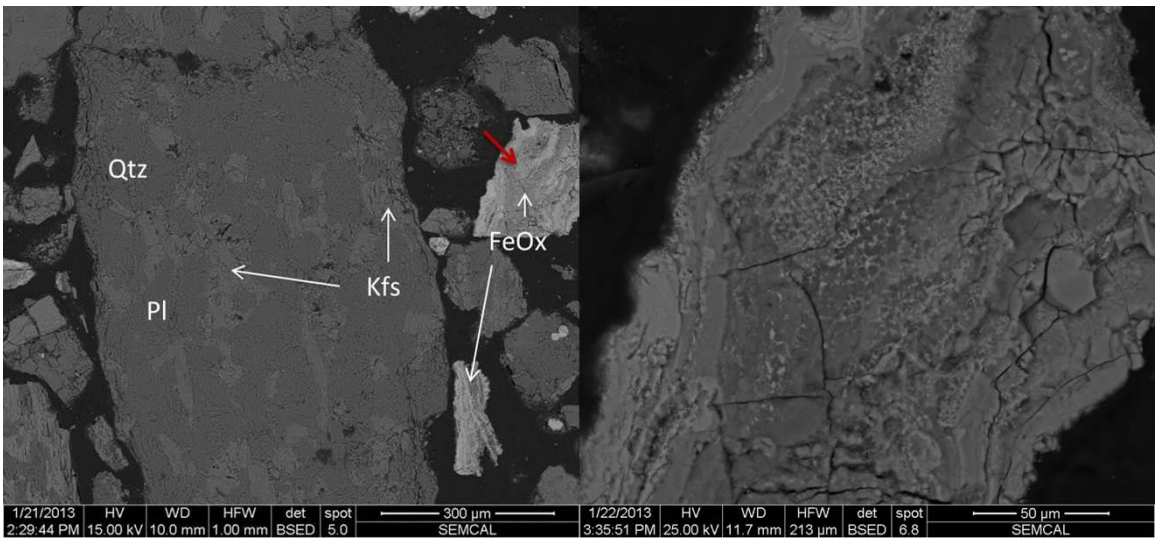

Figure 22. BSE images of large granodiorite grain (left) and iron oxide partially replaced with silica presenting a layered texture in Navy II well 42A-16 (8900-8930 ft). Red arrow points to the grain shown at higher magnification (right image).

4.2.7 Oxidation

Iron and titanium oxide minerals (limonite, magnetite, goethite, hematite, and rutile/anatase) are found associated with alteration zones and are indicative of the oxidation state of fluids from which these minerals formed. In Navy II well 42A-16, more abundant oxide minerals are found at greater depths (Figure 23). Secondary iron oxides are observed filling fractures (Figure 24) less than 1μm wide. Rutile/anatase is very rare in the Navy II well 42A-16 (less than 0.1% in volume from QEMSCAN). Titanium oxide from sample depth 2000-2010 ft is observed as a secondary mineral replacing quartz and mica (Figure 25). Sulfide minerals often weather easily because they are susceptible to oxidation and replacement by iron oxides (Figure 25). Oxides form most easily in the surface or near surface environment, where oxygen-rich fluids are more readily available (Lagat, 2007). Also very rare iron antimony oxide is found in Navy II well 42A-16 (7000-7020 ft). In particular, BSE images show Fe-Sb oxide as small, bright, needle-shaped crystals (Figure 19). Iron antimony oxide indicates a formation temperature of around 350°C in some laboratory experiments (Mitchell et al., 2000).

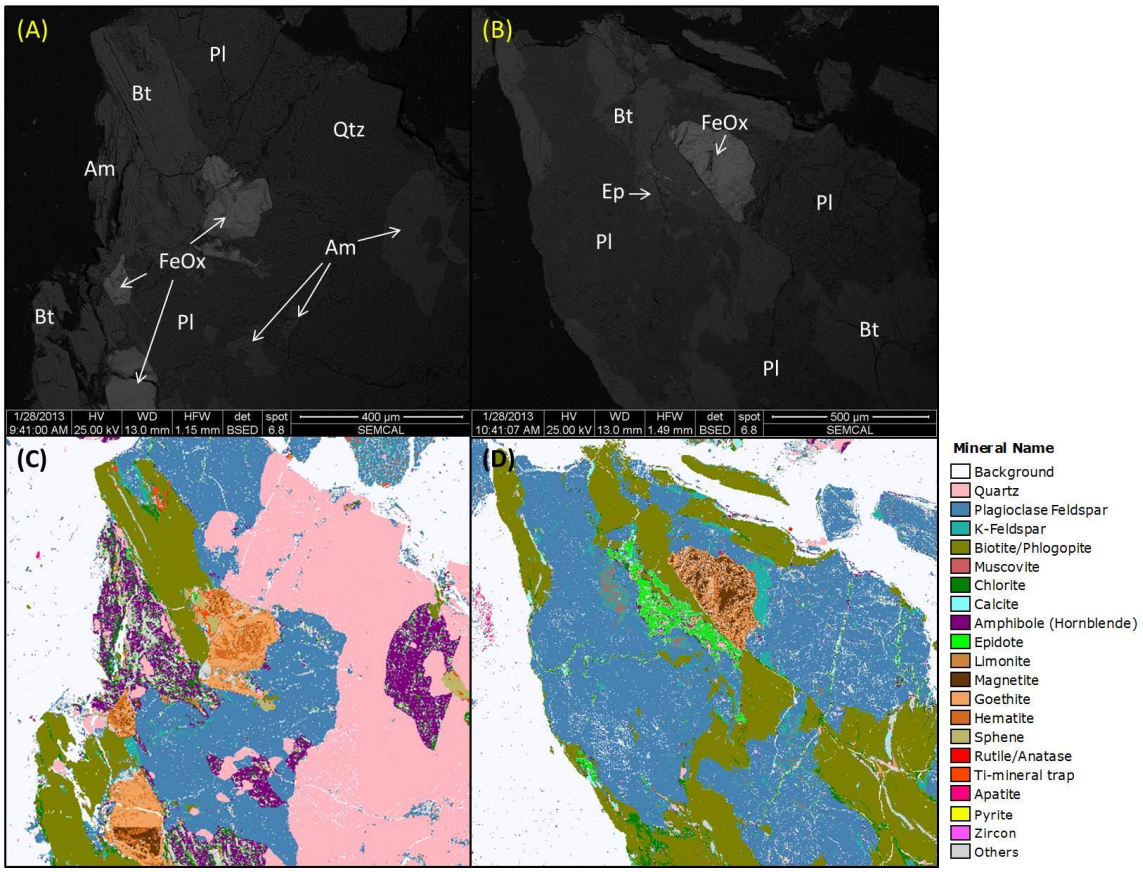

Figure 23. BSE images and QEMSCAN matching mineral maps from Navy II well 42A-16 (7000-7020 ft) showing iron oxides (goethite) associated with secondary sphene (left)) and epidote (right).

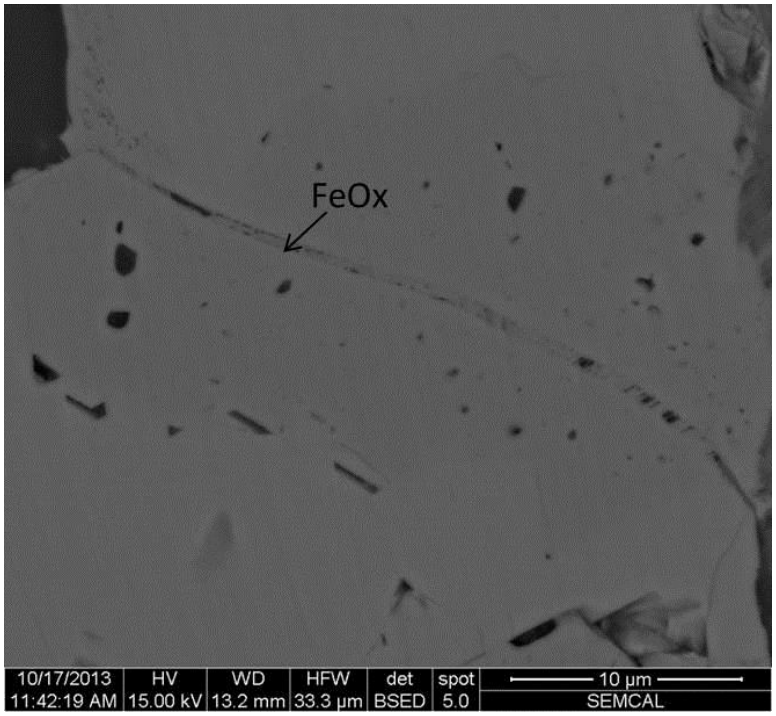

Figure 24. BSE image of iron oxides, including an apparent secondary iron oxide along a fracture line in Coso Navy II well 42 A-16 (2000-2010 ft).

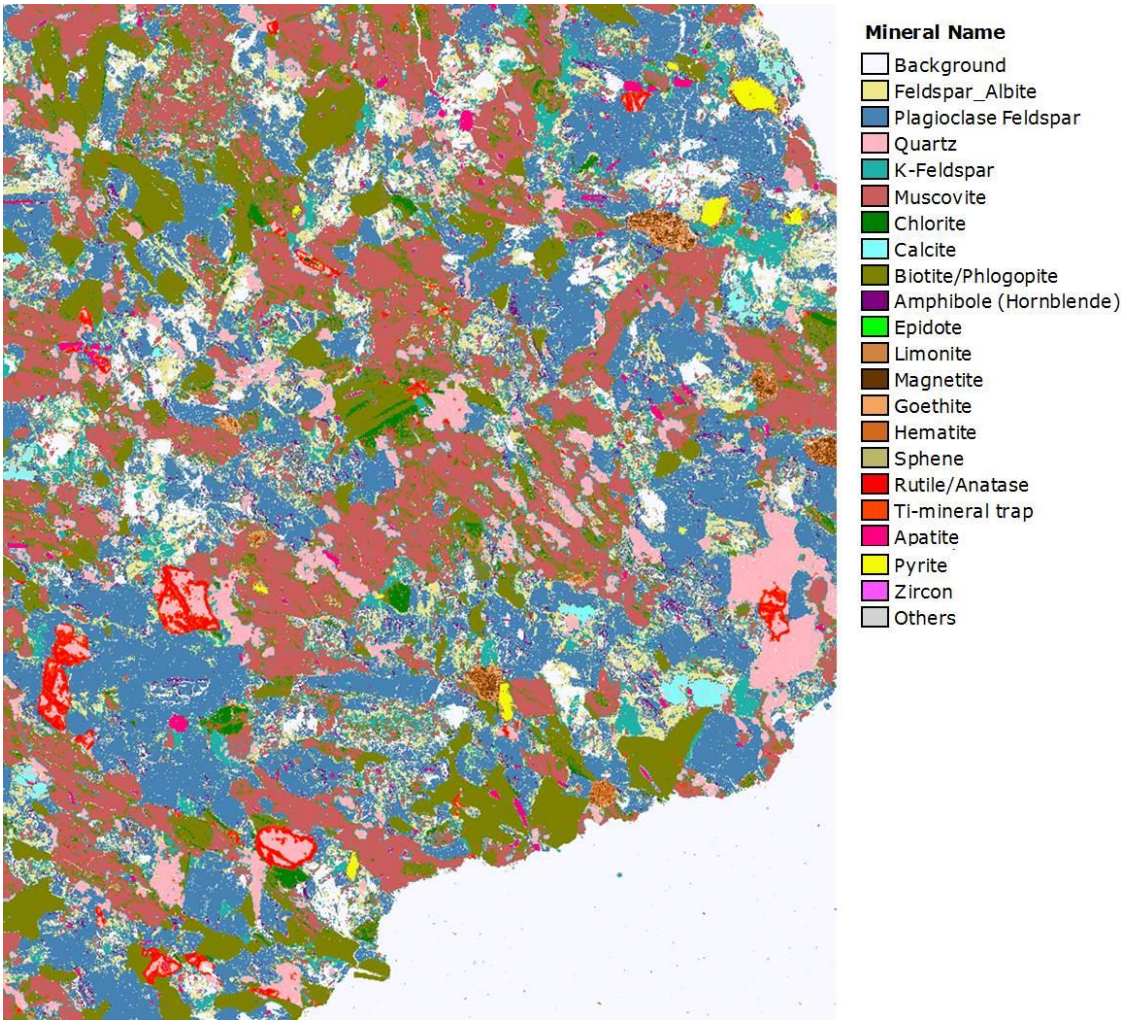

Figure 25. QEMSCAN mineral map showing secondary replacement textures of oxide minerals. Rutile/anatase forms rims around several quartz grains, and iron oxides form a rim around pyrite in Navy II well (2000-2010 ft). Dissolution features adjacent to albite and other plagioclase are dominant. Field of view is 2.0 mm.

4.3 Porosity and Pore Features

BET/N_2 surface area and pore volume/size data have been obtained and interpreted and then compared to neutron scattering data given in Anovitz et al (2013);

the latter can detect wider range of pores including isolated pores. SEM study is employed as a guide to assess pore types based on textural information. Porosity of the materials was determined on the basis of the following classification of the International Union of Pure and Applied Chemistry (IUPAC, 1985) concerning pore sizes: microporous (pore diameters of less than 2 nm), mesoporous (pore diameters between 2 nm and 20 nm), and macroporous (pore diameters greater than 20 nm).

4.3.1 BET Pore Analysis and Neutron Scattering

The BET method extends from micropores and mesopores to part of the range of macropores (1.7 nm -0.3 microns). All the samples measured produced similarly shaped adsorption and desorption isotherms, which show typical Type IV isotherm characteristics (IUPAC, 1985) for mesoporous materials. This isotherm linear plot (Type IV) (Figure 26) is a hysteresis loop, which is associated with capillary condensation taking place in mesopores. Four to six samples from four different wells were selected for BET analysis (Table 5). BJH method is used for the average pore volume and the average pore width, and is the most often used for estimating mesopore size distribution. This model is based on the Kelvin equation and corrected for multilayer adsorption using statistical film thickness (see details of this method by Barrett et al., 1951).

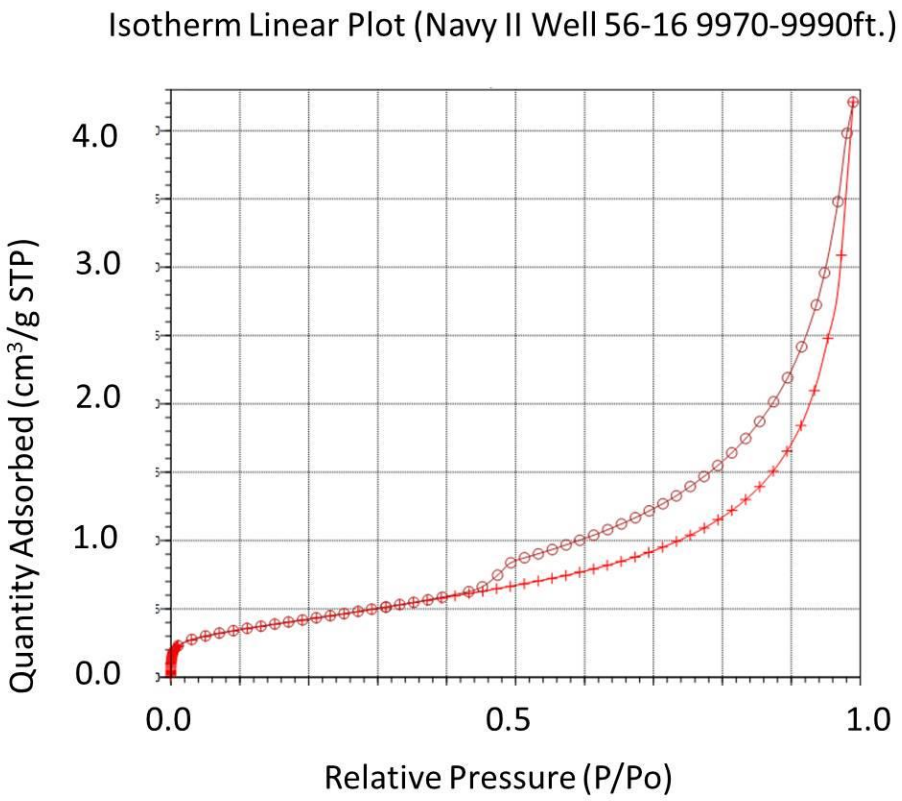

Figure 26. This representative isotherm linear plot for a sample from the Coso geothermal field shows the basic type of adsorption isotherm. + indicates adsorption; circles indicate desorption. Note there is some hysteresis behavior in this sample.

The average of BET/N_2 surface area in this study is 1.0931m^2/g, the average t-Plot external surface area is 1.2980 m^2/g, the average pore volume is 0.0062cm^3/g, the average pore width is 153 Å (15.3 nm), and pore width ranges from 106 Å (10.6 nm) to 279 Å (27.9 nm) (Table 5). The greatest total pore volume, 0.013514 cm^3/g, was determined from sample BLNM well 83-11 (100-110 ft), and the smallest total pore volume, 0.001883 cm^3/g, was determined from Navy II well 65A-18 (5980-6000 ft). In

Navy II well 42A-16 which we are focusing on, total pore volume and pore width tend to generally increase with depth. The exception to this trend is a larger pore volume for depth range 1000 to 1010 ft. and 6000 to 6030 ft, but the average pore width for these depths follows the trend. For the other wells, BLNM well 83-11, Navy II well 56-16, and Navy II well 65A-18, there is no trend found; the pore volume and the average pore width tend to be more or less random.

Table 5. Summary of gas adsorption data using BET measurement

Sample ID	Depth (ft)	Surface Area		Pore Volume		Pore Size	
		BET Surface Area (m^2/g)	t-Plot External Surface Area (m^2/g)	BJH Adsorption cumulative volume of pores, 17-3000Å (cm^3/g)	BJH Desorption cumulative volume of pores, 17-3000Å (cm^3/g)	BJH Adsorption average pore width (4V/A)(Å)	BJH Desorption average pore width (4V/A)(Å)
BLNM Well 83-11	100-110	2.84	3.39	0.0130	0.0135	216	161
BLNM Well 83-11	2990-3000	1.36	1.41	0.0071	0.0074	215	107
BLNM Well 83-11	5990-6000	0.92	1.19	0.0061	0.0062	244	198
BLNM Well 83-11	8990-9000	2.09	2.49	0.0096	0.0099	174	139
NAVY II Well 56-16	990-1010	0.78	0.92	0.0039	0.0040	191	129
NAVY II Well 56-16	3990-4000	0.30	0.56	0.0028	0.0028	287	158
NAVY II Well 56-16	6990-7000	1.31	1.45	0.0068	0.0070	201	143
NAVY II Well 56-16	9970-9990	1.59	1.73	0.0062	0.0065	152	112
NAVY II Well 65A-18	980-1000	0.50	0.69	0.0054	0.0054	305	117
NAVY II Well 65A-18	1970-2000	0.67	0.67	0.0045	0.0046	256	159
NAVY II Well 65A-18	2970-3000	1.59	1.47	0.0084	0.0086	174	128
NAVY II Well 65A-18	5980-6000	0.31	0.46	0.0019	0.0019	272	193
NAVY II Well 65A-18	7940-7970	0.45	0.61	0.0023	0.0024	220	167
NAVY II Well 42A-16	1000-1010	0.76	0.93	0.0047	0.0048	189	114
NAVY II Well 42A-16	2000-2010	0.68	0.84	0.0033	0.0034	196	136
NAVY II Well 42A-16	4000-4020	0.90	1.07	0.0044	0.0045	196	137
NAVY II Well 42A-16	5000-5020	1.26	1.39	0.0069	0.0071	208	158
NAVY II Well 42A-16	6000-6030	1.74	2.29	0.0093	0.0095	219	178
NAVY II Well 42A-16	7000-7020	0.72	1.08	0.0086	0.0088	425	279

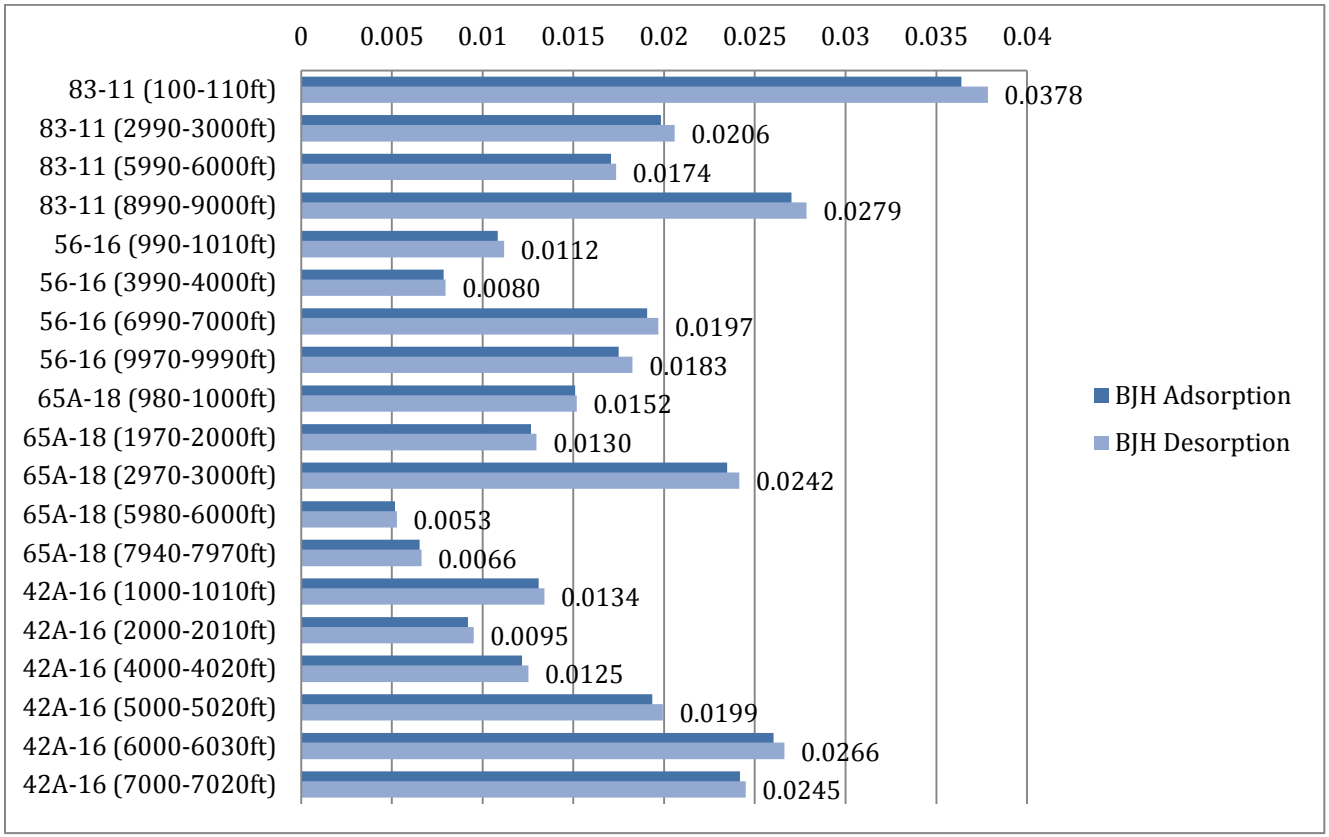

Figure 27. Mesoporosity of the Coso samples based on gas absorption data with rock density. Data are arranged by increasing depth. This calculated porosity only includes pore widths between 17-3000Å (1.7-300 nm).

Reasonable density estimates for the rocks in the Coso Range vary from 2.65 g/cm^3 for leucogranite to 3.0 g/cm^3 for gabbro (Telford et al., 1976; Carmichael, 1990). Using percentages of the various rock types encountered in drill holes in the Coso geothermal area as a guide, Monastero et al. (2005) suggests that a reasonable average density for the mixed complex is 2.80 g/cm^3. Therefore, the mesoporosity of each of the samples is generated by calculating total pore volume multiplied by the average rock density (Figure 27).

Figure 28 shows the pore size distribution in Navy II well 42A-16 as a function of pore size for two different depths. As can be seen in this graph, the deeper sample contains more pores between 17-3000 Å (1.7-300 nm). Both curves show a similar trend, which may indicate a mineralogical relationship due to the fact that both samples contain significant amounts of quartz diorite (see the section 4.1.4).

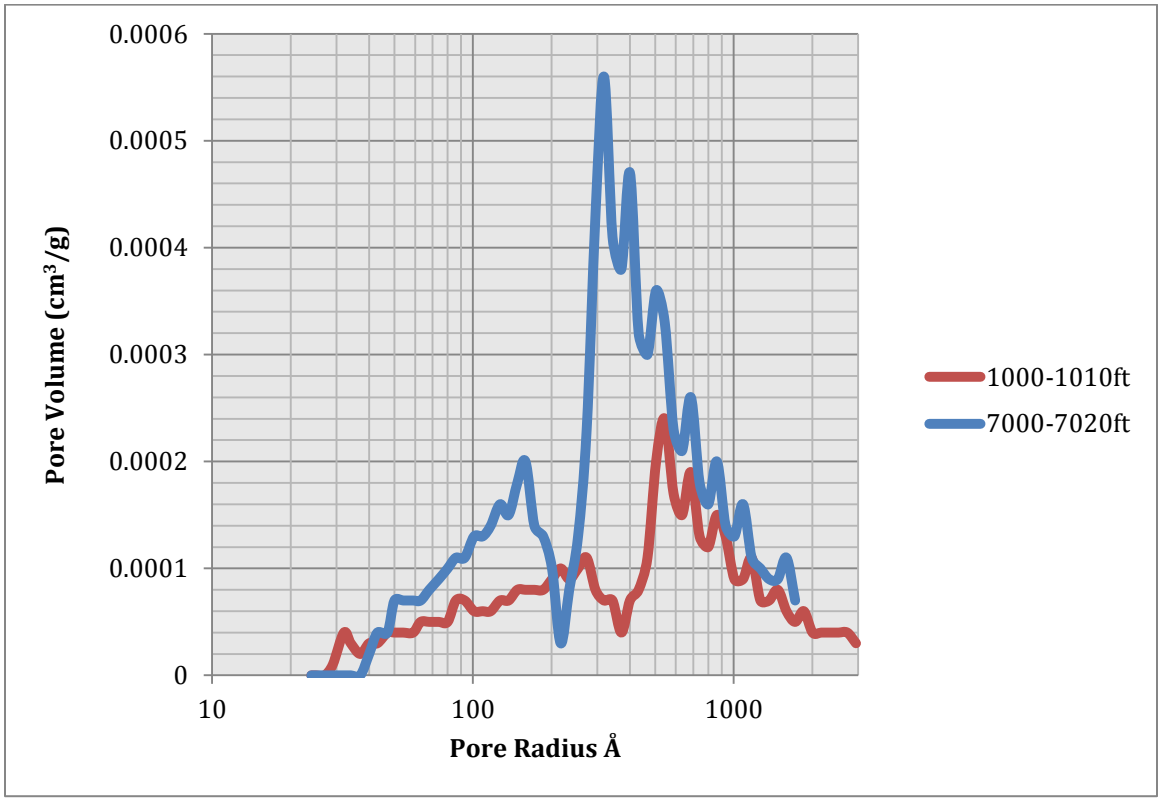

Figure 28. Incremental pore volume as a function of pore radius plot for Navy II well 42A-16 (1000-1010 ft and 7000-7020 ft). Note that mesopores range from approximately 2 to 200 nm (20 to 2000 Å). Approximately 550 Å (55 nm) pores dominate the shallowest sample, while 310 Å (31 nm) pores are abundant in the deeper sample. The average pore size in this diagram is 621 Å (62.1 nm) and 782 Å (78.2 nm) for 1000-1010 ft and 7000-7020 ft respectively.

As discussed in Chapter 3, neutron scattering measures all the pores, including connected as well as unconnected pores, and a wider range of pores (approximately 1.5 nm to 24 μm) as compare to the BET measurements. Figure 29 shows the pore volume as a function of pore radius, calculated from small and ultra-small angle neutron scattering data for the 1000 ft and 8900 ft samples, the shallowest and deepest samples available

form 42A-16 well. There is a gap within each curve between 10^3 and 10^4 Å (100 nm and 1 μm) in pore radius in Figure 29 which is the boundary between SANS (left) and USANS (right) measurements.

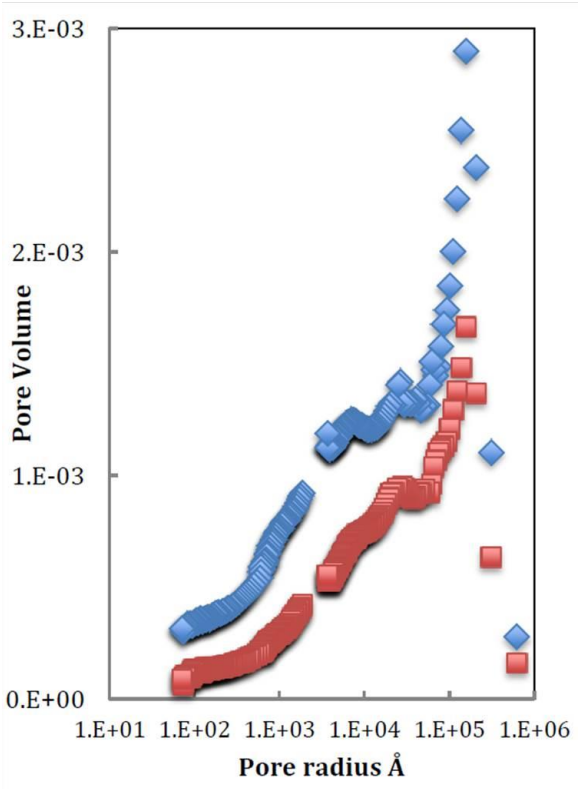

Figure 29. Total pore volume as a function of pore radius for the 1000 ft sample (red) and the 8900 ft sample (blue). (From Anovitz et al., 2013)

Comparison between neutron scattering data and BET measurement data allows an estimation of unconnected porosity which does not contribute to transport (Figure 30). Because neutron scattering data (SANS) detects all the void spaces between 70 and 2000

Å (7 and 200 nm) size in this graph, the difference between two curves indicates the volume of unconnected porosity in this sample. As can be seen, there is a significantly large gap between two curves suggesting that most of the porosity present in these chip samples is unconnected. However, this result needs confirmation using other analytical methods such as micro–computed tomography (μCT) which offers a three dimensional view of materials.

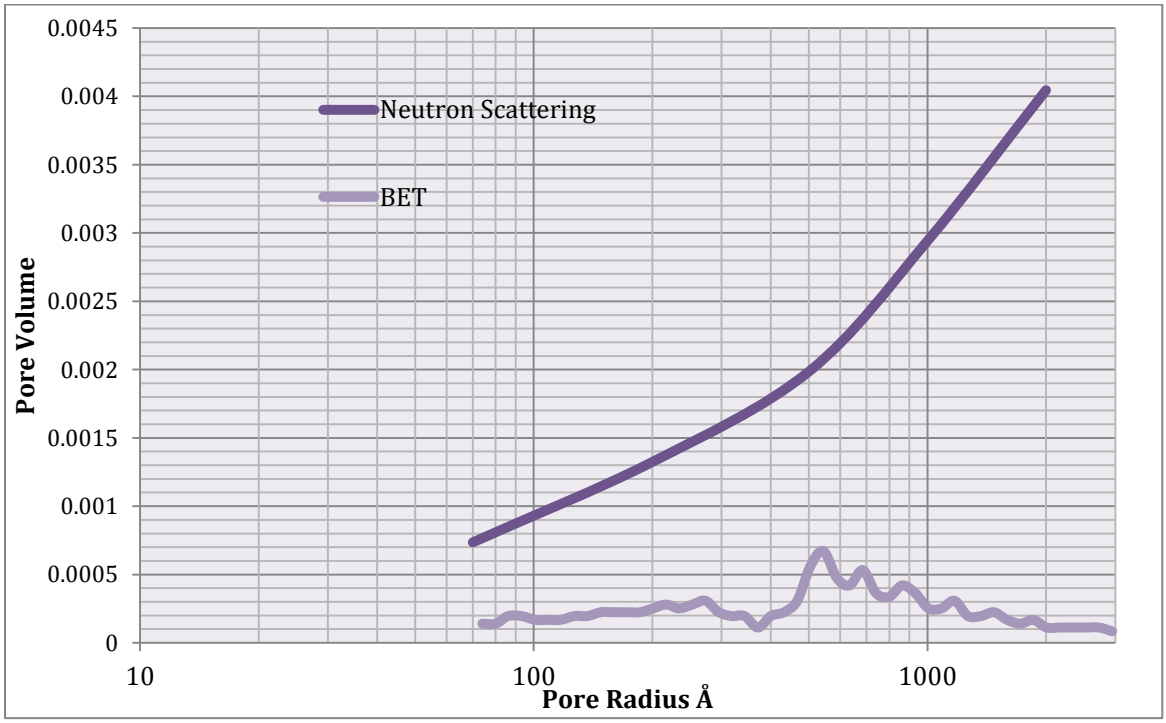

Figure 30. Neutron scattering and BET pore analysis data for Navy II well 42A-16 (1000-1010 ft). Neutron scattering data are from the left portion of 1000-1010 ft graph in Figure 29. The unit of pore volume in this graph is cm^3/cm^3 (fraction).

4.3.2 Macropores in SEM images

Macro-sized pores are defined as cavities that are larger than 20 nm which is suitable for observation using SEM. Because gas sorption and neutron scattering are not able to detect pores bigger than 0.3μm and ~240 μm, respectively, in principal SEM examination can help construct overall pore size distribution in the Coso system. More importantly, SEM also contributes to our understanding of the relationships among pores, fractures, and mineralogy when considered along with QEMSCAN analysis.

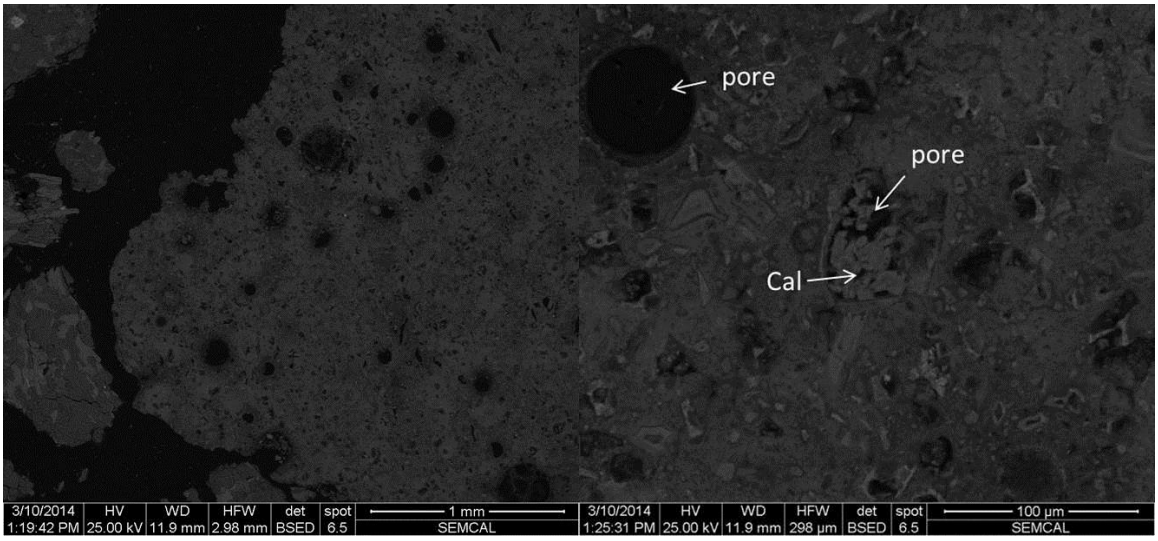

Figure 31. BSE images showing circular shaped vesicular pores ranging up to 40 $\boldsymbol{\mu}$m at Navy II well 42A-16 (6000-6030 ft). Some calcite crystals are found inside or along the edges of the pores.

Vesicular pores are found at two depth rages, 6000-6030 ft, and 8900-8930 ft in Navy II well 42A-16 (Figure 31, Figure 32), and these represent the largest pore sizes

found in this well. Vesicular porosity usually forms due to gas release, and this type of pore is commonly considered to be primary porosity. These circular shaped pores resemble pores in basalt and indicate that gas trapped in rocks escaped and formed the pores. This porosity may contribute to great portion of the overall mesoporosity. According to Anovitz et al. (2013), samples from the deepest depth exhibit the highest total porosity, as observed by neutron scattering, and meanwhile, BET data show that the sample from 6000-6030 ft has unexpectedly high effective mesoporosity, contrary to the increasing trend of porosity with depth (see above section 4.3.1).

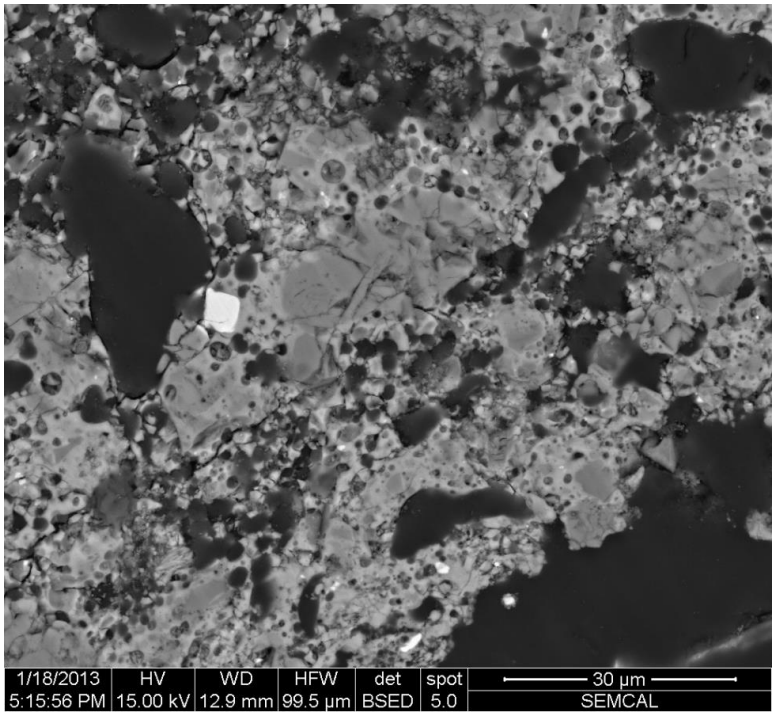

Figure 32. BSE image of pores from Navy II well 42A-16 (8900-8930 ft). Pore size ranges from a few microns to tens of microns.

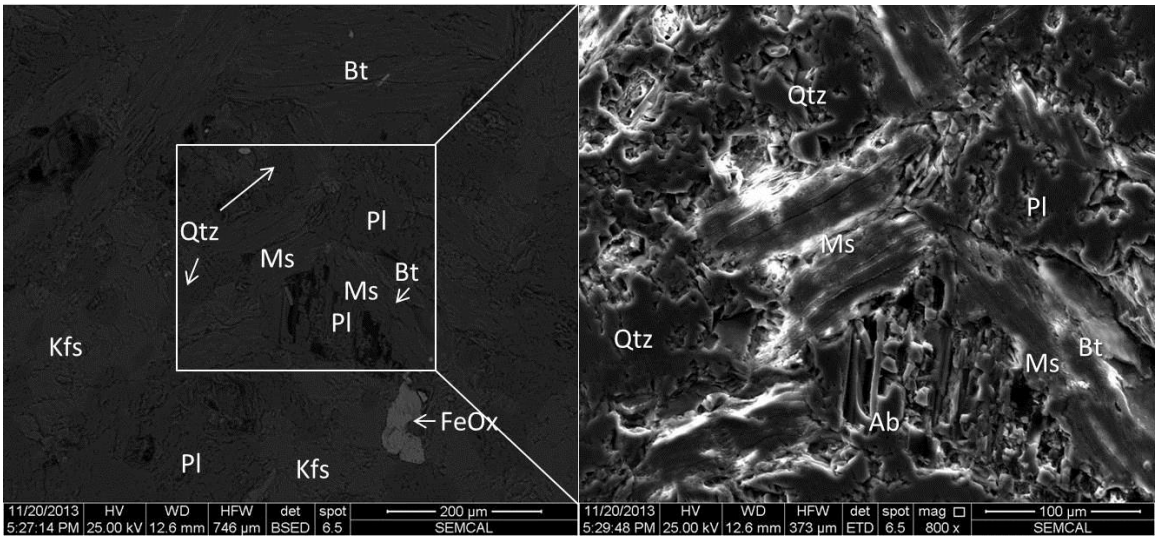

Figure 33. BSE (left) and ETD (right) images showing dissolution pits in an albite grain from Navy II well 42A-16 (2000-2010 ft). The pore width is up to ~0.1μm. The white rectangle delimits the higher magnification ETD image (right).

Dissolution porosity is defined as porosity caused by the dissolution of mineral grains during diagenesis or as secondary porosity caused by thermal events, such as in geothermal fields. Such pores can form during hydrothermal events, and are commonly found in plagioclase (Figure 33), and quartz (Figure 34). Moreover, intragranular micron-sized pores are found in biotite (Figure 35). Cleavage planes, especially in phyllosilicates, offer an avenue for hydrothermal fluids to move through, and form larger pores for mineral precipitation along the cleavages. Additionally, in a deep sample form Navy II well 42A-16 (8900-8930 ft), intragranular pores are associated with linear microfissures in amphibole, with 1-2 μm apertures (Figure 36). Pores observed in SEM are mostly secondary pores related to water-rock interaction. More data are needed to associate

porosity and mineralogy, as described in the Discussion chapter below. Quantifying connected versus unconnected pore mineralogy is the subject of future work.

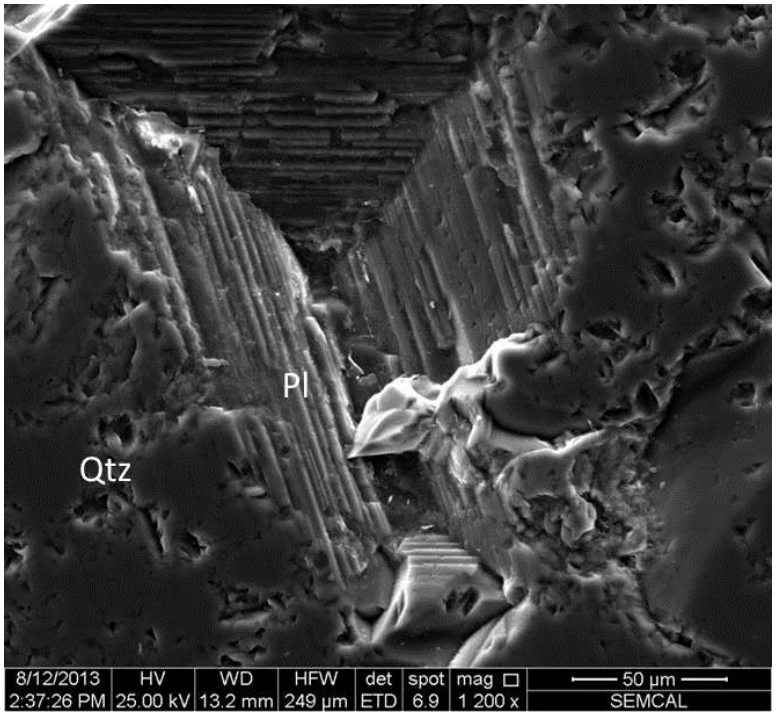

Figure 34. ETD image showing dissolution pits approximately 1 μm in size (Navy II well 42A-16; 2000-2010 ft).

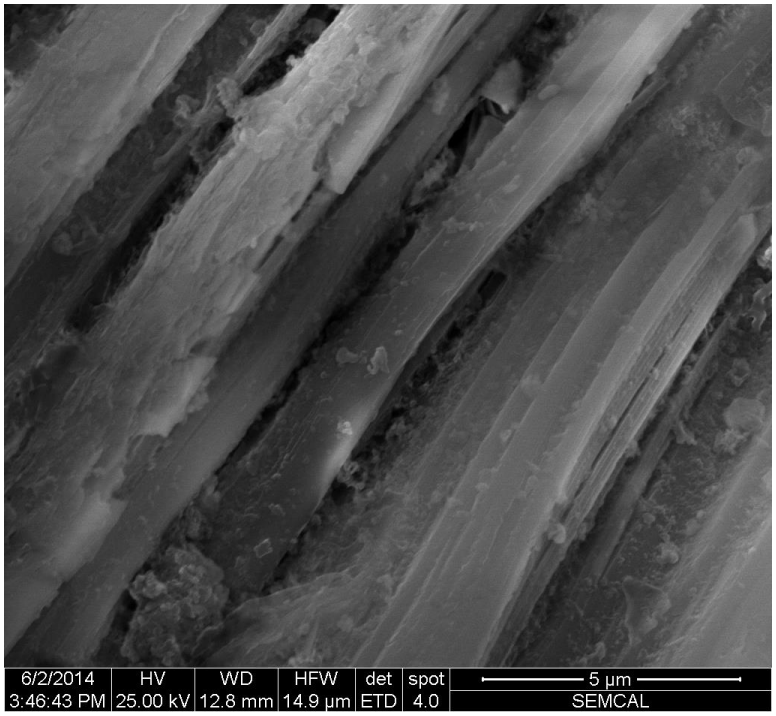

Figure 35. ETD image showing pores within biotite layers. Apertures range up to 0.5 μm in scale at Navy II well 65A-18 4980-5000 ft.

Figure 36. PPL image from Navy II well 42A-16 (8900-8930 ft) shows a long fracture in an amphibole grain. The width is approximately 1-2 µm. The blue proxy is shown inside of the fracture (red arrow). Field of view is 0.3 mm

Chapter 5: Discussion

A number of important parameters are needed to understand water-rock interaction including temperature (T), pressure (P), fluid and gas chemistry (major anions and cations – e.g. ionic strength, CO_2 and other acid gas composition), pH, mineralogy of unreacted rocks and their hydrothermally altered equivalents. Not all of the parameters above have been used for this study due to the limits of sample and data availability. Specifically, fluid data for other Coso wells were taken from previous studies (Fournier et al., 1980; McLin, 2012). Borehole temperature in Navy II well 42A-16 is available from the Coso operator (Appendix E) (Jess McCulloch, pers. comm.) as well as those reported for older wells.

As a first step to understanding water-rock interaction in Coso, fluid chemistries are used as input in geothermometer equations to estimate subsurface temperatures, which then can be compared to measured down-hole temperatures using data from the literature. The second step is to use the characterization of time-dependent coexisting mineral assemblages (from paragenetic assessments) to construct activity-activity diagrams that will help map out the changes in fluid-rock chemistries as a function of temperature to be compared to mineral paragenetic evolution. Collectively these steps will provide a sense of the conditions of mineral alteration and evolution that can be compared and contrasted against the physical features of the rocks namely porosity.

Finally we introduce radial diagrams showing the relationship between minerals and pores, leading to a discussion of porosity and permeability of the Coso geothermal system based on the combined results from BET and NS data as well as new methods, micro-CT, mercury intrusion porosimetry (MIP), and a porosity-permeability nomogram, introduced here.

5.1 Chemical Geothermometry

The compositions of geothermal fluids depend on their geologic setting (depth, rock type, temperature, and pressure), source of recharge waters and the contribution of gases from magmatic or metamorphic sources. Maximum subsurface temperatures experienced by geothermal waters can be recorded ("frozen in") by ionic ratios in solutes and the water itself. Such information is important in geothermal resource evaluation. It also reflects the depth of groundwater circulation, based on an understanding of regional tectonics and geothermal gradients. Geochemical geothermometers developed over the past three decades rely on the assumptions that the two species or compounds coexisted and have equilibrated within the geothermal reservoir that temperature is the main control on their ratio, and that re-equilibration has not occurred during ascent and discharge. The principal drawback to these chemical geothermometers is that given enough time or low water-rock ratios, re-equilibration can occur through exchange reactions at lower temperatures during fluid ascent.

Thus, assessment of geothermometers can lead to (a) a quantitative understanding of reservoir temperatures in the Coso geothermal field, (b) an estimate of how water-rock

interactions changed as a function of space and perhaps even time and (c) a prediction of the evolution of the system as it continues to be exploited for energy. In this study, several geothermometer equations were used to estimate subsurface temperatures based on fluid data reported by Fournier et al (1980) and McLin (2012) (Appendix D). I used geothermal equations in Karingithi's paper (2009) which provided a nice overview of geothermometers and its mechanism. However, some equations (Na-K (1) by Fournier (1979) and Na-K-Ca by Fournier and Truesdell (1973) geothermometers) were improperly documented, and therefore we used the same equations in Fournier (1980). The waters from Coso are of the uniformly chloride-rich category (Fournier et al., 1980). According to the fluid inclusion study by Moore et al. (1990), fluid inclusions in the Coso geothermal system record a broad range of temperature from 76°C up to 328°C. Also, down-hole temperature data for Navy II well 42A-16 well are also available (193-288°C) (Appendix E).

The correlations between temperature and various geochemical parameters (e.g., Si, Na/K, Na-K-Ca, Na/Li and K-Mg) as dictated by mineral-fluid equilibria form the basis of the chemical geothermometers. The equations used to calculate the reservoir temperature in Coso geothermal field are provided in (Table 6). The results of these calculations are depicted in a series of figures (Figure 38, Figure 39).

Table 6. Temperature equation (in °C) for geothermometers (concentrations in mg/L)

Geothermo-meters	Source	Equations
Quartz	Fournier (1977) (no steam loss)	T (°C) = 1309 / (5.19 - log (SiO_2)) - 273.15
Chalcedony	Arnorsson et al. (1983)	T (°C) = 1112 / (4.91 - log (SiO_2)) - 273.15
Amorphous silica	Fournier (1977)	T (°C) = 731 / (4.52 - log (SiO_2)) - 273.15
Na-K (1)	Fournier (1979)	T (°C) = 1217 / (1.483 + log (Na / K)) - 273.15
Na-K (2)	Giggenbach et al. (1988)	T (°C) = 1390 / (1.75 + log (Na / K)) - 273.15
Na-K-Ca	Fournier and Truesdell (1973)	T (°C) = 1647 / [log (Na / K) + β {log $\left(\frac{\sqrt{Ca}}{Na}\right)$ + 2.06} + 2.47] - 273.15 $\log(\frac{\sqrt{Ca}}{Na}) + 2.06 < 0 \; and \; t > 100^0$C, β = 1/3 $\log(\frac{\sqrt{Ca}}{Na}) + 2.06 > 0 \; and \; t < 100^0$C, β = 4/3
Na-Li	Fouillac and Michard (1981)	T (°C) = 1195 / (0.130 - log (mNa / mLi)) - 273.15 (Valid for Cl concentrations of >0.3 mol/kg)

5.1.1 Silica Geothermometers

The silica geothermometers are based on quartz/chalcedony/amorphous SiO_2 solubility and appear to be the one of the most reliable indicators of reservoir temperature.

Figure 37 shows that quartz, chalcedony, and amorphous silica geothermometer curves along with measured downhole temperatures for '1977 CGEH well No. 1' and '1967 Coso well No. 1' (location of wells is available in Figure 1).

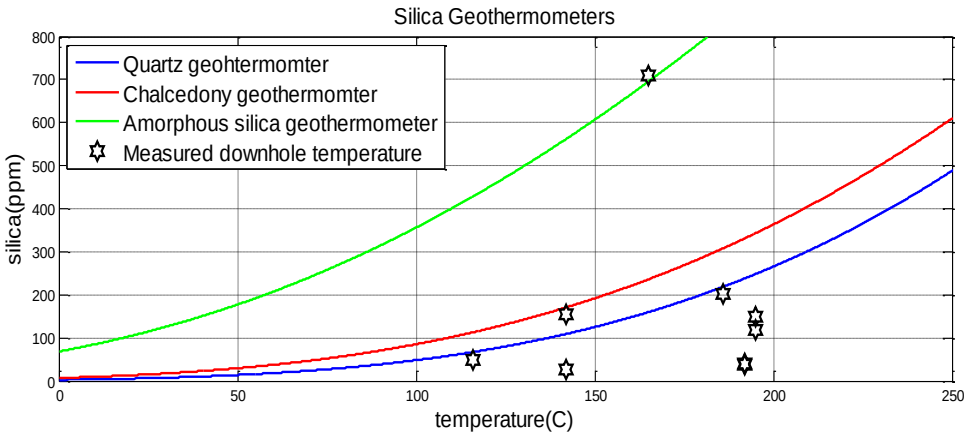

Figure 37. A diagram showing silica geothermometry curves and measured downhole temperature in Coso geothermal field. Silica concentration and temperature data are from Fournier et al. (1980). References for each geothermometer are in the text

According to the silica geothermometer study by Schettler et al. (2013), alkali-feldspar alteration releases silica, whereas the albitization of anorthite consumes silica. In addition, silica solubility does not correlate with pH, but the concentration of silica is temperature dependent. The basic reaction of silica dissolution is

$$SiO_2\,(qtz) + 2H_2O = H_4SiO_4 \quad (4)$$

Silica geothermometers are based on; 1) the regression of experimental quartz solubility in pure water along the liquid-vapor saturation curve; 2) the assumption that the dissolved Si in the aquifers is in equilibrium either with quartz, chalcedony, or amorphous silica.

As can be seen Figure 38 and Figure 39, among the silica geothermometers the quartz geothermometer of Fournier (1977) yields reservoir temperatures 180^0C for one sample in CGEH well No. 1, and range from 258°C to 277°C for Coso well 28-33 well. The Coso well 28-33 is located in near the Dixie Valley power plant where which is southeast of the Stillwater Range. The reason why the calculated temperature of silica geothermometer is not plotted for the most of the samples from CGEH No.1 and Coso well No.1 is because the calculated results are not within the concentration range of the silica geothermometer can measure is best suited for. Compared with quartz geothermometer, the chalcedony geothermometer of Arnorsson et al. (1983) yields much lower reservoir temperatures ranging between 119-135°C for three samples from CGEH well No. 1 and Coso well No. 1, and 110^0C for one sample from Coso well 28-33 well. Since chalcedony, rather than quartz, tends to control silica saturation at temperatures less than 180°C (Fournier, 1991), it appears that among the silica geothermometers, the chalcedony geothermometer better predicts the reservoir temperatures for fluid sampled from CGEH well No. 1 and Coso well No. 1, whereas quartz geothermometer is better suited in the Coso well 28-33 well. Amorphous silica geothermometer in Figure 37 has been tested, but the results are negative or close to negative, thus the values are excluded in the results presented in Figure 38 and Figure 39. Fournier et al. (1980) noted that there may be some error associated with select analyses of silica contents from CGEH well No.

1 and Coso well No. 1 so the geothermometer values may be suspect in some case. This will be further checked by using the cation geothermometers.

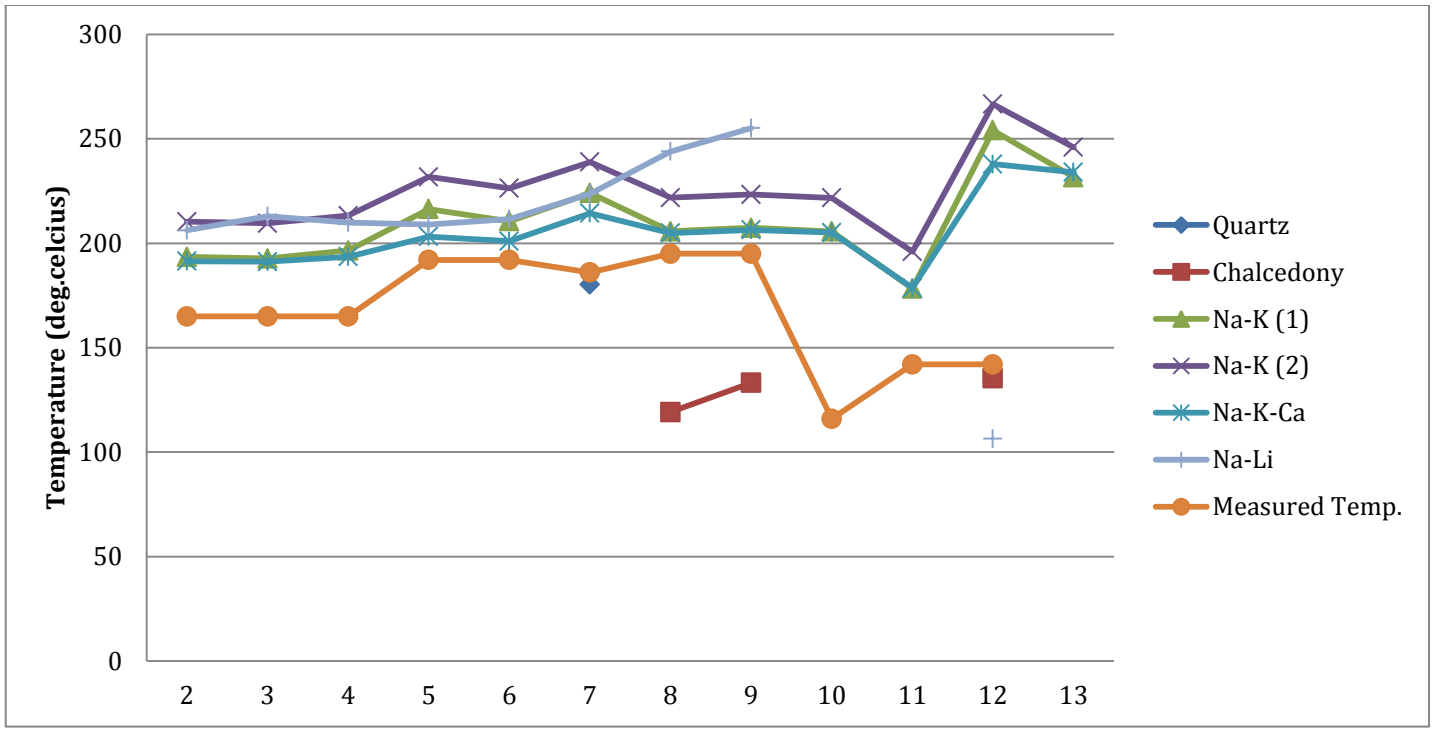

Figure 38. The results of chemical geothermometers. Fluid data are from Fournier et al. (1980). X axis refers to each sample ID; from 2 to 9 are from 1977 CGEH well No. 1, from 10 to 13 are from 1967 Coso well No. 1 over time. (see Appendix D for the information of sample collecting date and fluid chemistry)

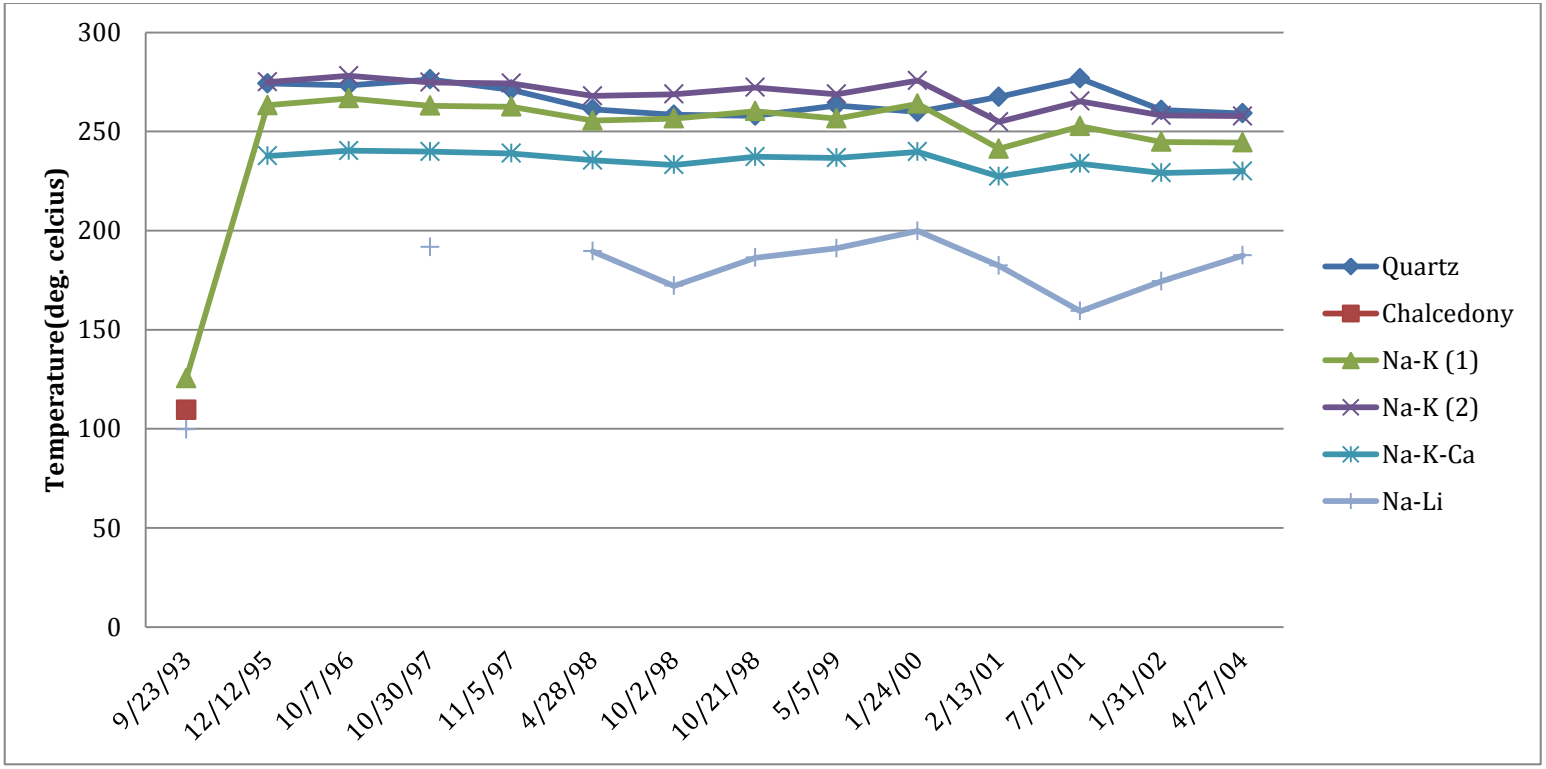

Figure 39. Estimates of reservoir temperatures based on chemical geothermometers as a function of sample date for well 28-33. Fluid data are from McLin (2012) and originally reported by Goff et al. (2002) and Terra-Gen (unpublished).

5.1.2 Cation Geothermometers

The reservoir temperatures computed from the cation geothermometers for each sample are higher than those of silica geothermometers as shown in Figure 38. Conversely, Na-K geothermometers are good agreement with quartz geothermometer for the Coso well 28-33 (Figure 39). The Na-K geothermometers are suitable for the high temperature reservoirs (180°C) composed of chloride-bearing waters, consistent with the type of waters sampled from the Coso geothermal field. The temperature dependence of the cation exchange ratio between K-feldspar and albite indicates the ration decreases with increasing temperature and forms the basis of this geothermometer.

$$NaAlSi_3O_8 \text{ (albite)} + K^+ = KAlSiO^8 \text{ (K-feldspar)} + Na^+ \quad (5)$$

Based on the two Na-K geothermometers described by Fournier (1979) and Giggenbach et al. (1988) estimated reservoir temperatures range from 178-254^{0}C and 196-267^{0}C, respectively, for CGEH well No. 1 and Coso well No. 1 (Figure 38). As can be seen in Figure 38, the temperatures of Na-K (1) (Fournier, 1979) are slightly higher (approximately 16.4 ^{0}C higher) than those of Na-K (2) (Giggenbach et al., 1988), but shows similar trend for each sample.

Interestingly the Na-K geothermometers yield temperatures similar to those obtained from the Na-Li geothermometer (Fouillac and Michard, 1981) for the CGEH well No. 1 (sample from 2 to 9). The sodium-lithium geothermometer used here is empirical and based on the Na/Li ratio from the general reaction:

$$\text{Clay-Li} + H^+ = \text{Clay-H} + Li^+ \quad (6)$$

The result of Na-K geothermometer calculation for Coso well 28-33 yields temperature of 241-267°C for Na-K (1) and 255-278°C for Na-K (2) respectively and the calculated temperature tends to decrease over time.

The Na-Li geothermometer yields temperatures lower than those obtained from the quartz, Na-K, and other geothermometers for Coso well 28-33. This may be because some Li is lost from solution to alteration minerals (e.g., mica) or during cooling. The K-Mg geothermometer of Giggenbach (1988) was excluded for this study because the results exhibit unrealistically low negative temperatures. These differences between the result of the K-Mg and other geothermometers may indicate shallow conditions of mixing with groundwater.

In order to account for mineral-fluid reactions involving Na-Ca-bearing feldspars Fournier and Truesdell (1973) developed the Na-K-Ca geothermometer. When using this geothermometer, one first calculates the value of "$\log(\frac{\sqrt{Ca}}{Na}) + 2.06$" with cation concentrations expressed as mg/kg or ppm. If the calculated value ends up positive, β = 4/3 is used, if negative, one uses β = 1/3 to calculate this geothermometer (Fournier and Truesdell, 1973). The reservoir temperatures for samples 9 to 13 in Figure 38 yield the temperatures which are very similar to those of the Na-K (1) geothermometer and slightly lower than those of Na-K (2) and Na-Li geothermometers (Figure 38). For the Coso well 28-33 well, the results of the Na-K-Ca geothermometer shows constant or slightly decreasing values over time from 240 to 230°C (Figure 39).

On the basis of the above observations, it is found that the temperatures calculated from some of the geothermometers are in reasonably good agreement with measured temperatures in Figure 38. Based on a comparison of measured temperatures with the temperatures calculated using different geothermometers such as Na-K, Na-K-Ca, and Na-Li, it is evident that, with the exception of sample from the Coso well No. 1, the values obtained from the CGEH well No. 1 are in relatively close agreement with the measured temperatures. Specifically, the calculated temperatures are all within about 50°C of the measured temperatures, and except the samples collected at wellhead (see Table 8 in Appendix D), calculated temperature is much closer to measured temperatures (36°C). Some of the samples in the Coso well No. 1 collected from wellhead (4 out of 5) may be not the representative for the reservoir temperatures. For the Coso well 28-33, no downhole temperature data are available to compare with, but the good agreement of four geothermometers including quartz, Na-K (1), (2), and Na-K-Ca may provide a reasonable estimate of the temperature over time.

From the application of six different geothermometers to 27 samples, we found that Na-K-Ca geothermometer (Fournier and Truesdell, 1973) can be used in some of the Coso geothermal samples, but perhaps not for all. The temperatures calculated using these geothermometers, and the Na-K (1) and (2) geothermometers are fairly consistent with the measured temperatures for most of the samples. However, less strong relationships have also been found between temperatures from silica geothermometers and those from other geothermometers for CGEH well No. 1 and Coso well No. 1, and between temperature from Na-Li geothermometer and those from other geothermometers

for the Coso well 28-33. In fact, silica composition and Na/Li ratio are influenced not only by temperature, but also by other parameters such as the redox conditions of the precipitating solutions, the bulk composition of the host rock, the mineral assemblage present, etc. In the case of CGEH well No. 1, the results of the silica and cation geothermometers are in fairly close agreement with the present-day temperatures.

5.2 Paragenetic Sequence of Alteration and Vein Mineralogy

In previous studies, Rose et al. (2003) and Kovac et al. (2005) interpret the paragenesis of the vein and alteration minerals in order to develop a conceptual model of the thermal history of the Coso geothermal system. As shown in Figure 3, Kovac et al (2005) provide a paragenesis diagram for the East Flank based on petrographic and petrologic study and several fluid inclusion analyses. The results of this study indicate that the oldest vein minerals are epidote and pyrite and the most recent veining mineral is calcite. Furthermore, fluid inclusion data show that the modern geothermal system is superimposed on rocks altered in an older, lower temperature thermal regime (Kovac et al., 2005).

Figure 40 and Figure 42 summarize the general paragenetic sequence of alteration and vein minerals in Navy II well 42A-16, and 65A-18, respectively, based on crosscutting relationships and the successive replacement and overprinting of alteration and vein minerals. In Figure 40, the paragenesis diagram includes every depth range that well cuttings are available from Navy II well 42A-16. The paragenesis graph for Navy II well 65A-18 only includes the depth ranging from 4980 to 5000 ft based on SEM and

QEMSCAN data availability. The depth from 4980-5000 ft was targeted because this depth interval is where the most extensively altered sample was observed by optical microscopy and, like the same depth at Navy II well 42A-16, where evidence of extensive propylitic alteration is observed. However, the rock types at Navy II well 42A-16 and 65A-18 from same depth (5000 ft) are different; sodic granite is dominant in Navy II well 42A-16, whereas granodiorite and quartz diorite are dominant in 65A-18.

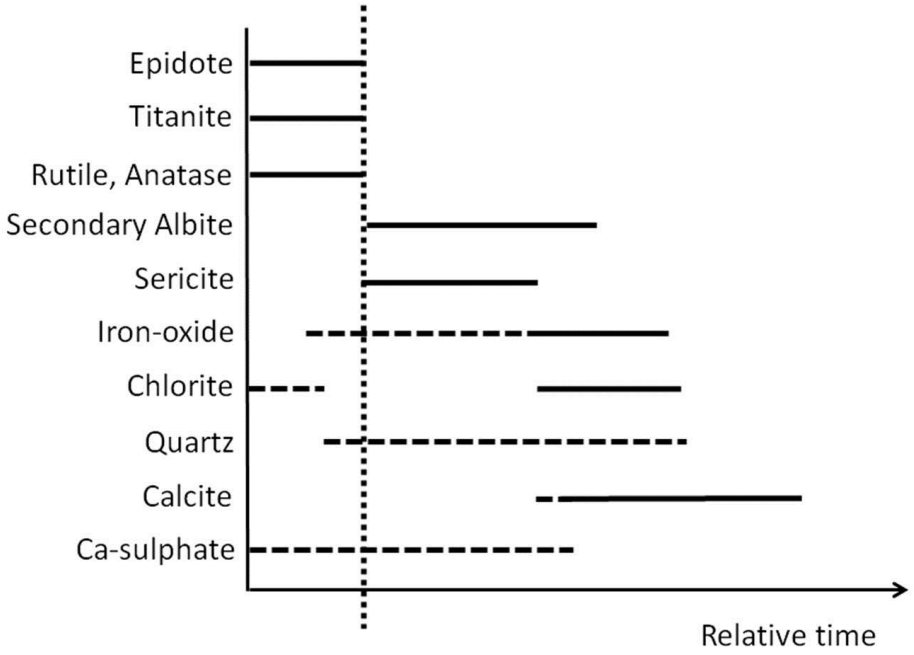

Figure 40. Paragenetic sequence of alteration and vein mineralization in Navy II well 42A-16. Horizontal dashed lines indicate that timing of mineral formation is less certain. A vertical dotted line represents the last stage volcanism. Ca-sulphate is only observed in the sample from depth 5000-5020 ft.

Among the earliest minerals to form were epidote, titanite, rutile/anatase, and chlorite; whereas the most recently deposited minerals were calcite, and chlorite for the Navy II well 42A-16 (Figure 40). A vertical line indicates the latest volcanism, which means mineral formation to the left side of this line may have a metamorphic origin. As can be seen in Figure 17, secondary titanite occurred within the biotite planes, and chlorite, quartz and calcite replaced or embedded into primary amphibole and biotite. Secondary rutile/anatase was observed at 2000-2010 ft (Figure 25), and the rutile replaces the edge of the quartz and sometimes muscovite (Figure 41, A). Albitization and sericitization are encountered all the samples, but dominate at 5000-5020 ft (Figure 13). These alterations types are more likely to occur together in granodiorite and quartz diorite (Figure 12) with the reactions expressed in equation (1) and (2) in Section 4.2 alteration section. Conversely, granites tend to be less altered as shown in Figure 41, (B) compared to other rock types such as granodiorite and quartz diorite. This may be because the granites are a later-stage rock, thus having been exposed to circulating hydrothermal fluids for a shorter duration of time. Chloritization is observed at every depth, and occurs as either a replacement of feldspar and mica (Figure 13), or sometimes occurred within calcite veins (Figure 12, Figure 18). For example, the basic reactions of chloritization are (Cathelineau, 1986):

$$2\ NaAlSi_3O_8 + 8H_2O + 2Mg^{2+} + 3Fe^{2+} \rightarrow Chl + 3\ SiO_2 + 2Na + 8H^{+} \quad (7)$$

$$CaAlSi_3O_8 + SiO_2 + 8H_2O + 3Mg^{2+} + 2Fe^{2+} \rightarrow Chl + Ca^{2+} + 8H^{+} + 6Bi + 2OH^{+} \quad (8)$$

$$6Bi + 20H^{+} + 2Na^{+} \rightarrow 2Chl + 2Ab + 6Fe^{2+} + 2Mg^{2+}\ 20H_2O + 6K^{+} \quad (9)$$

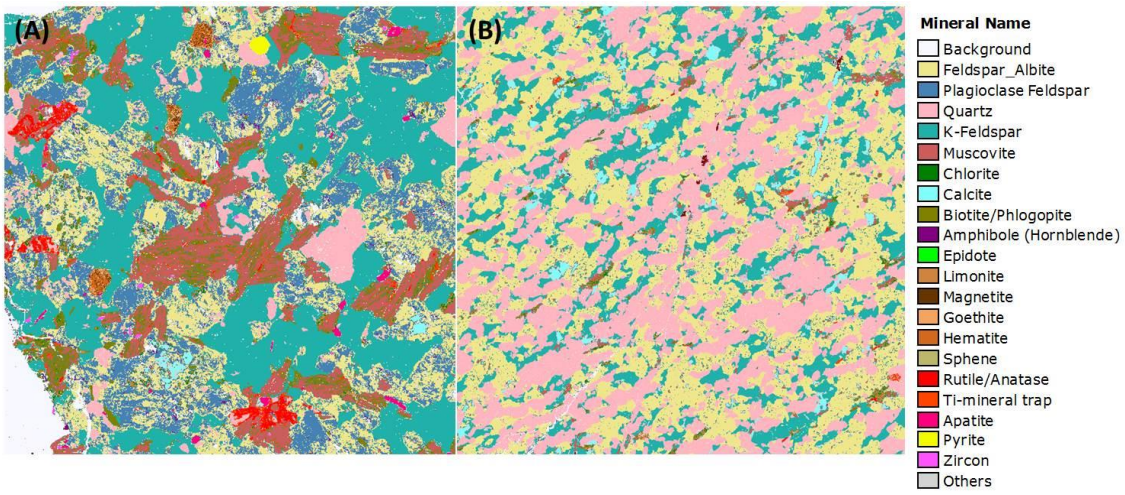

Figure 41. QEMSCAN mineral maps shows (A): secondary replacement textures of rutile/anatase which forms rims around several quartz and mica grains, and albitization with calcite filling in Navy II well 42A-16 (2000-2010 ft). (B): Less altered grain (granite) with secondary calcite veins in Navy II well 42A-16 (5000-5020 ft) Field of view is 1.8 mm.

From the chemical equations above, chlorite can be formed as a replacement of plagioclase (shown in Figure 14 for Navy II well 65A-18) and biotite reacting with Mg and Fe-bearing fluid. These secondary minerals are observed in the middle stage of a paragenetic sequence in this part of the Coso system. Mineral solubilities of Ca-sulfate and calcite decrease with increasing temperature (retrograde solubilities) which may the temperature regime over which these minerals formed. Ca-sulfate is observed only at depth 5000-5020 ft, and its relative timing of formation remains somewhat uncertain, although it does appear before the latest stage of calcite. A number of calcite veining

events are observed (Figure 13, Figure 18), based on cross-cutting relationships (Figure 41.A). Early-formed calcite is associated with chlorite and quartz, but in order to verify that these are indeed different generations of calcite, fluid inclusion analysis is needed.

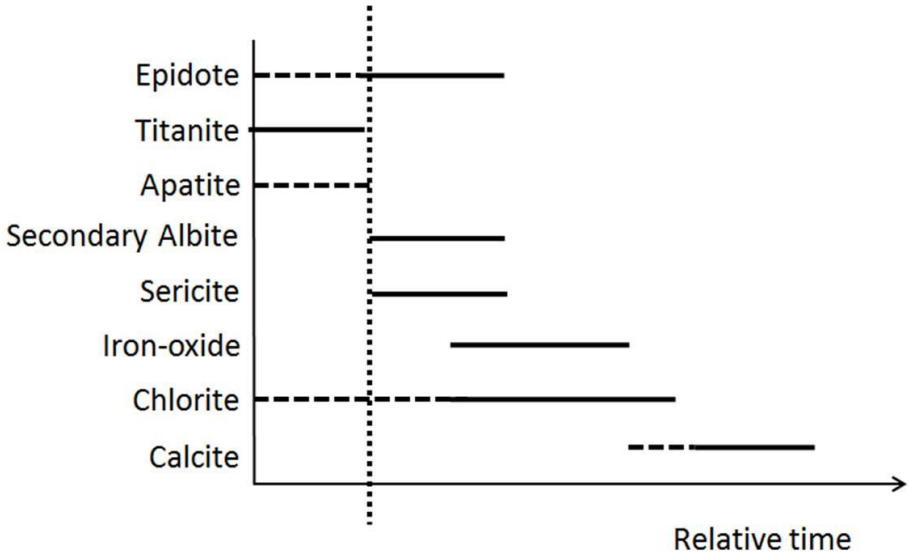

Figure 42. Paragenetic sequence of alteration and vein minerals in Navy II well 65A-18 (4980 to 5000 ft). Horizontal Dashed lines indicate that the approximate timing of mineral formation is less certain. A vertical dotted line represents the last stage volcanism.

For the Navy II well 65A-18 (4980 to 5000 ft), most of the paragenetic sequence is similar to that for the Navy II well 42A-16. Due to the fact that it is based on sample from only one depth range, fewer alteration types can be sequenced (Figure 42). The earlier mineral assemblage is titanite, and perhaps epidote, apatite, and chlorite (Figure 8 ,

Figure 9, and Figure 17). Epidotization is observed along with albitization and sericitization (Figure 14), and the possible reaction is (Strens, 1964):

$$4SiO_2 + 4CaAl_2Si_2O_8 + H_2O + (Na, K)_2CO_3$$

$$\rightarrow 2CaAl_3Si_3OH + 2(Na, K)AlSi_3O_8 + CO_2 \quad (10)$$

where quartz plus calcic-plagioclase breakdown to form a calcic-epidote and alkali feldspar.

Kovac et al. (2005) report that vein assemblages can include epidote (Fe-poor) + sericite + quartz +/- chlorite and adularia, which, according to them, implies temperatures in excess of ~250°C. Given that similar alteration dominates the mineral assemblages in Navy II well 65A-18 as well as 42A-16, temperatures in excess of 250°C may also be controlling reactions. The main difference between the two diagrams is that no early stage of calcite is apparent in Navy II well 65A-18 for this depth. The sequence of mineral paragenesis is similar to Navy II well 42A-16. Calcite represents the last stage of secondary alteration in both wells.

One can ask how we can reconcile the geothermometer temperatures (Section 5.1) that seem to predict reasonable "present-day" downhole temperatures based on silica and feldspar-based reactions with what we know about the paragenetic sequence of these key phases. Both quartz and feldspar-based alteration reactions occur early or in the middle of the paragenesis for Coso. Despite the fact that these phases have already formed does not preclude their participation in subsequent water-rock reactions if we assume the Coso system is "rock-buffered", which it likely is, where fluid cation chemistry is controlled by

the dominant mineral assemblage. Hence, present-day dissolution of key silicate phases such as the feldspars could contribute the Na-K-Ca cations used in the geothermometer calculations yielding reasonable subsurface temperatures.

5.3 Fluid-Mineral Equilibria

The results discussed above indicate that despite variability in the rock types the associated alteration mineralogy of quartz, Na-Ca feldspar, K-feldspar, and K-mica influence the composition of thermal waters via fluid-mineral equilibria reactions. The nature of fluid-mineral equilibria can be used to explain the formation of hydrothermal minerals and mass transfer in response to water-rock interaction. To investigate the fluid-mineral equilibria in the Coso geothermal field, activity (stability) diagrams were constructed for key phases and their reactions over a range of temperatures. The operative temperature ranges that could be targeted include 220-265°C calculated from the chemical geothermometers, 193-288°C from the temperature profile in Navy II well 42A-16 (Appendix E), and up to ~328°C from fluid inclusion homogenization data in the Coso geothermal field (Moore et al., 1990).

Activity diagrams allow simple graphical analysis of mineral stabilities as a function of a limited set of fluid species in multicomponent system. They are useful for representing fluid-mineral equilibria and predicting mass transfer governed by temperature-dependent minerals, especially in rock-dominated (rock-buffered) environments (Giggenbach, 1997). The activity diagrams have been produced using the software package The Geochemist's Workbench (Bethke, 1992), which is based on the thermodynamic database created at the Lawrence Livermore National Laboratory

(Delany and Lundeen, 1990). In the calculations, activity of water is assumed to be unity, and activity diagrams were computed with Act2 software in the Geochemist's Workbench (GWB). In order to show the temperature effect on the mineral boundaries, the diagrams in Figure 43 were drawn at 200°C, 250°C and 300°C. In producing the activity diagrams, three different chemical systems were considered: Na_2O-K_2O-Al_2O_3-SiO_2-H_2O, CaO-K_2O-Al_2O_3-SiO_2-H_2O, and HCl-H_2O-Al_2O-CaO-MgO-FeO-SiO_2 to assess the phase behavior of the key alteration minerals, albite, muscovite (sericite), K-feldspar, chlorite, and epidote.

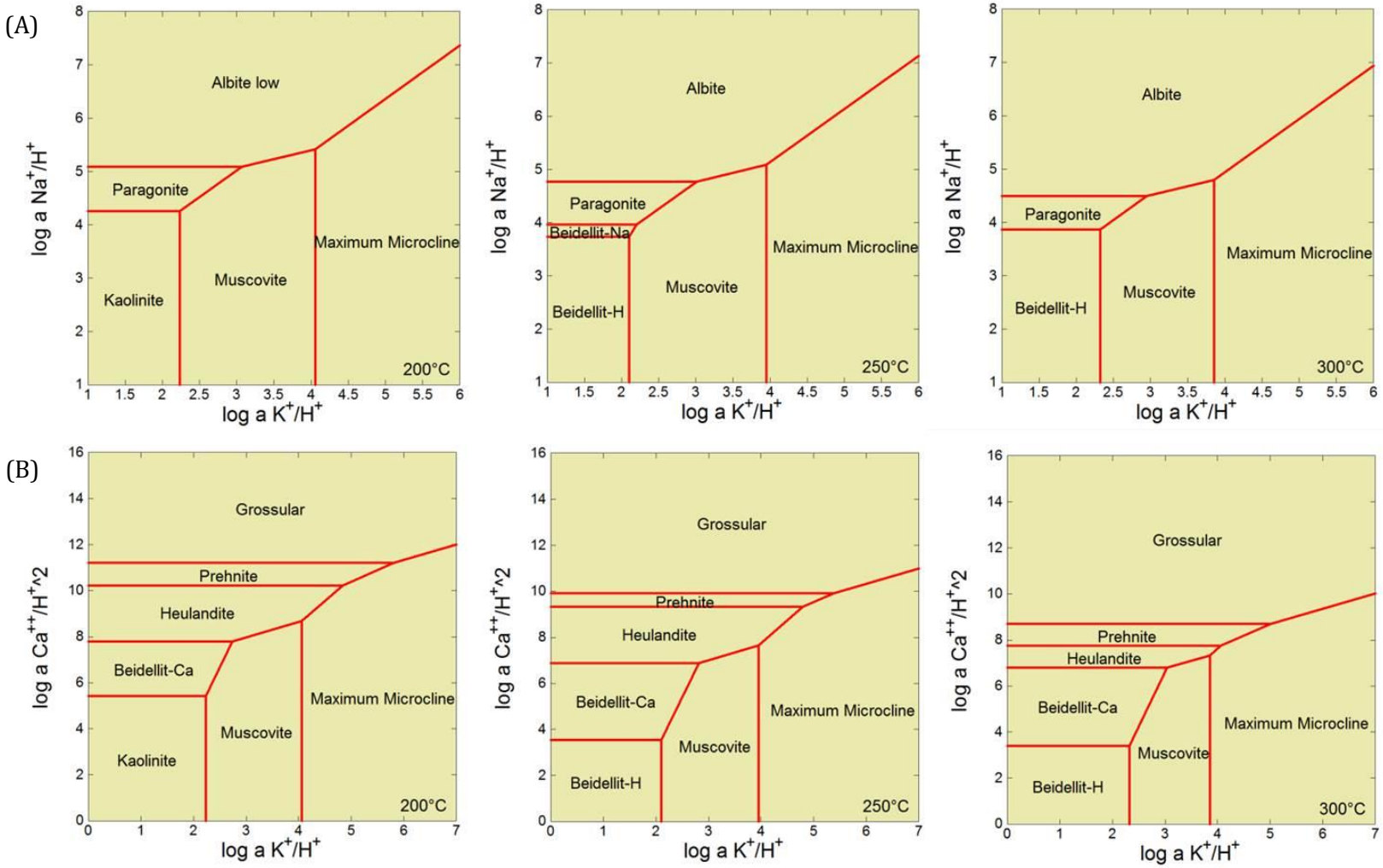

Figure 43. Activity diagrams for important mineral assemblages in the Coso geothermal system. (Continue)

(C)

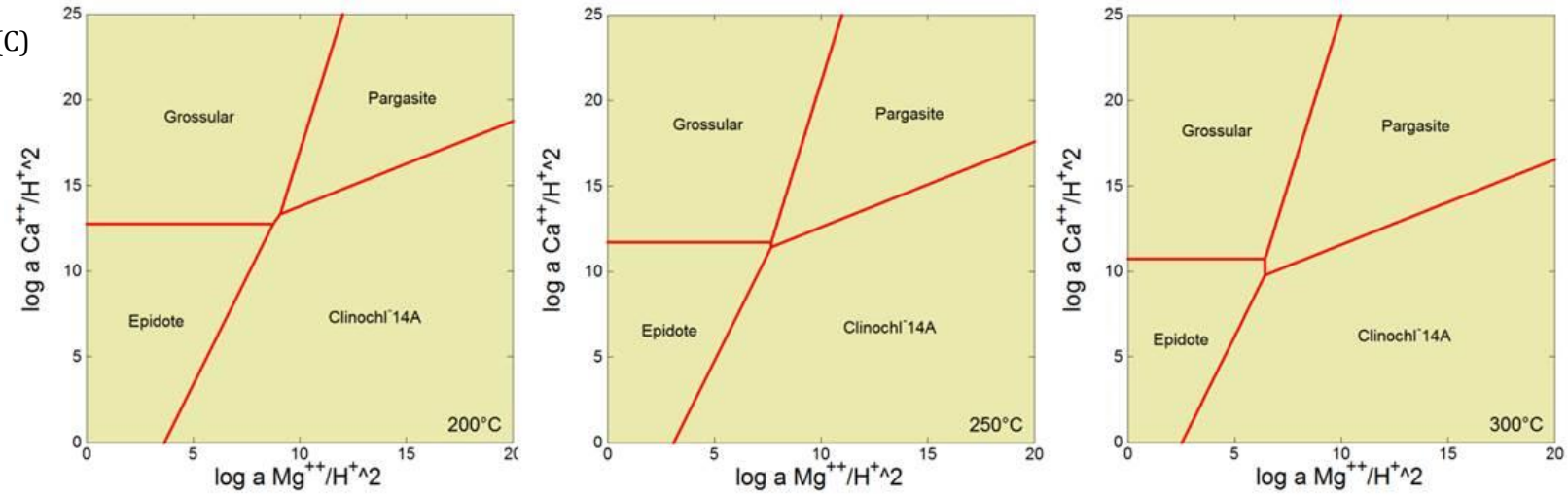

Figure 43. Activity diagrams for important mineral assemblages in the Coso geothermal system at 200, 250, and 300^{0}C in the systems of (A): Na_2O-K_2O-Al_2O_3-SiO_2-H_2O, (B): CaO-K_2O-Al_2O_3-SiO_2-H_2O, and (C): HCl-H_2O-Al_2O-CaO-MgO-FeO-SiO_2 showing the stabilities of each mineral at hydrothermal conditions. The data for muscovite were used as a proxy for K-mica (sericite) in (A), (B).

According to petrographic studies, fluids in this system may be close to equilibrium with the assemblage comprising albite, K-feldspar, and muscovite (mostly in form of sericite) which are the earlier replacement phases in this system. Although fluid chemistry data of the wells studying here is not available, the chemistry perhaps lie near the triple point albite/muscovite/K-feldspar phase fields, reflecting alteration of primary plagioclase, according to reactions such as (Figure 13):

$$\text{albite} + K^+ + H_2O = \text{K-mica} + \text{K-feldspar} + Na^+ \qquad (11)$$

This diagram also can suggest change in mineral stability fields as temperature changes. For examples, as can be seen in Figure 43, (A), the albite stability field expands with increasing temperature at the expense of the muscovite and microcline stability fields. So, albite should relatively more stable in the system during higher temperature hydrothermal alteration.

The principle phases controlling the potassium and sodium ions are Na-K feldspar, K-mica (mostly sericite) and to some extent K-clay, specifically illite/smectite reported by Bishop and Bird, (1987) and Kovac et al. (2005). For the log $Ca^{2+}/(H^+)^2$ and log K^+/H^+ diagram (B), aside from muscovite, K-feldspar which are minerals we found in this study, heulandite is a zeolite group mineral which was reported by Davatzes et al. (2010) in the Coso geothermal system, but has not been identified in the wells studied here. Thus, phases in the Coso geothermal system are likely to be equilibrated within K-feldspar, muscovite, heulandite, and beidellite (smectite). The kaolinite stability field disappears as temperature goes up in these activity diagrams (it appears only in the figure for 200°C).

Muscovite and microcline and also the heulandite stability fields shrink as temperature increase. The lines where the grossular and microcline meet changed to more horizontal oriented line which suggests that the stabilities fields between two minerals is more likely to be influenced by log $Ca^{2+}/(H^{+})^{2}$.

Also shown in activity diagrams Mg-Ca (Figure 43, C) represents an equilibrium trend of propylitic alteration in the Coso geothermal system (e.g. Figure 17). To apply to the paragenetic sequence for Navy II well 42A-16 (Figure 40)), fluid activity composition may lie within the epidote phase field at first and then move to chlorite phase (clinochlore in the graph) for the middle and late stages of paragenesis. As can be seen in Figure 43, C, the clinozoisite and clinochlore stability fields become slightly smaller, and the pargasite (amphibole) field expands with increasing temperature. Moreover as temperature increase from 200°C to 300°C the mineral assemblages at the triple points are changed: 1) when 200°C, grossular-epidote-clinochlore and grossular–pargasite-clinochlore assemblages exist 2) 250°C, two triple points in two assemblages nearly meet together, and 3) 300°C, mineral assemblages in the triple points are changed to grossular-epidote-pargasite and pargasite-clinochlore-epidote, thus this combination of minerals exhibits higher temperature environment in this system.

Paragonite (upper three diagrams in Figure 43, (A)), which is a sodium-bearing hydromica, has not observed in this study. Similarly, prehnite (bottom three diagrams in Figure 43, (C)) has not been observed. More data are needed regarding the chemical composition of hydrothermal minerals (e.g., solid solutions, detailed stoichiometry) in order to better quantify the physical-chemical characteristics of the reservoirs. Also if

reliable modern-day the fluid data from the wells in this study can be obtained, thermodynamic fluid speciation can be calculated and compared to the phase behavior depicted in the activity diagrams to test how mineralogy controls fluid chemistry at depth in the reservoir.

5.4 Mineralogy Associated with Pores

In the Section 4.3, data on porosity and pore connectivity were presented based on complementary analytical tools, including optical petrography, BET, neutron scattering, and SEM. However, it is possible to address what physical-chemical characteristics contribute the most to controlling the porosity and permeability in this system. As discussed in Sections 5.2 and 5.3, mineral phases and their relative quantities vary spatially and temporally as the result of continued water-rock interaction over the life-time of Coso. In hydrothermal systems, porosity, pore and fracture morphology, and their evolution are directly related to the formation or destruction of hydrothermal minerals. One the one hand, hydrothermal alteration sometimes can lead to more porous and fractured rocks through dissolution of lithic fragments and minerals. Conversely, secondary authigenic mineralization can occur via recrystallization or precipitation in pores and fractures so the rock porosity decreases and the rock can self-seal. Therefore, mineralogy and porosity are closely intertwined, and influenced by one another. The association between (alteration) mineralogy and porosity is difficult to quantify using well cutting samples, but it is possible to qualify which minerals exhibit a stronger correlation with pores (or fractures) than others.

QEMSCAN analysis was conducted to explore the relationship between mineralogy and pores by automatic point counting to identify voids within minerals or those adjacent to minerals. As summarized in figures below (and also in Appendix C), the contribution of each mineral to total porosity and relative contribution to pores for each mineral were determined using QEMSCAN data of Navy II well 42A-16 in the Coso geothermal system. The digital images produced by QEMSCAN can be processed to quantify mineral association and association between minerals and pores and fractures which is separate from the damaged pore/fracture along the edge of the cuttings. The blue line in the radial diagrams shows the area percent of mineral pixels adjacent to pore (void space), which are called "association with background" in I-discover software, and herein referred to as "contribution to total porosity", so this is related to overall porosity. The QEMSCAN data can also be used to generate the relative ratio of mineral area percent (red line), which is mineral area percent adjacent to pore, divided by total mineral area percent. Accordingly, the red line indicates the "ratio of association with background" in the software, referred to as "relative contribution to pores per each mineral". In other words this yields estimates of the extent of porosity encountered by individual minerals which has been normalized to its area percent.

Minerals commonly observed in nearly every sample include plagioclase, quartz, and K-feldspar. These phases contribute the greatest portion of total porosity, which may be associated with the dissolution of primary minerals or alteration to secondary mineral/vein events. For example formation of secondary and quartz in paragenesis at the mid-stage of the paragenesis in Navy II well 42A-16 (Figure 40) produces observable

pore space. As shown in Figure 44, plagioclase makes a significant contribution to porosity especially in the depth range from 2000-2010 ft (blue line). This is verified by SEM observation, which reveals dissolution features within plagioclase (Figure 25). Additionally, both the QEMSCAN image in Figure 41, (A), and BSE image in Figure 33 show good examples of dissolution features in plagioclase, which resulted from albitization through the reaction between Ca-plagioclase and sodium bearing fluid ($NaAlSi_3O_8 \cdot CaAl_2Si_2O_8 + H_4SiO_4 + Na^+ = 2NaAlSi_3O_8 + Al^{+3} + Ca^{+2} + 4OH^-$) (1). As can be seen this image, calcite is also partially filling the pores but they are not completely sealed, so this partial calcite filling event may not seal off all vein porosity in this rock. The higher relative contribution to pores per calcite (red line) and its occurrence later in the paragenetic sequence suggest that the calcite may be the dominant phase controlling fluid access to current matrix pores and fractures. Figure 45 show plagioclase pits in the sample from Navy II well 42A-16 (2000-2010 ft). Overall, contribution to total porosity of plagioclase is fairly high in other samples in Navy II well 42A-16. However, phases in granitic grains are exception. As can be seen in Figure 41, (B), granite grains are observed to be less altered compared to other rock types in Navy II well 42A-16, and the depths where the granite grains are abundant range from 3000 to 5020 ft. In most cases, calcite sealed pores in granite grains, thus it is hard to find void space at coarse as well as finer length scales. For that reason, one diagram (5000-5020 ft in Appendix C) shows a lower contribution to total porosity of plagioclase and calcite, and lower relative contribution to pores of calcite. This result may be biased due to the

limited QEMSCAN data which only cover granite grains (not quartz diorite and diorite in this depth).

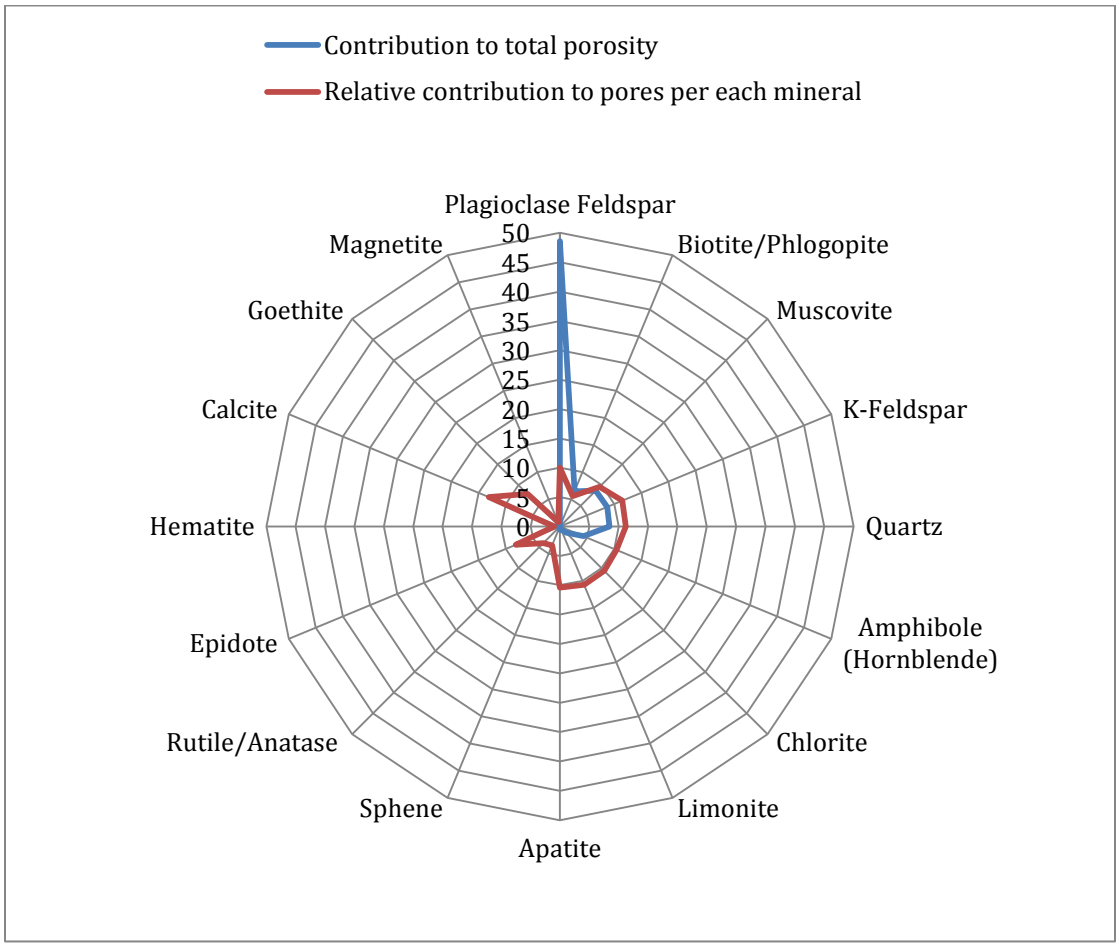

Figure 44. Association between mineralogy and pores and fractures for Navy II well Coso 2000-2010 ft. Note that plagioclase contributes to a significant amount of the porosity at this depth.

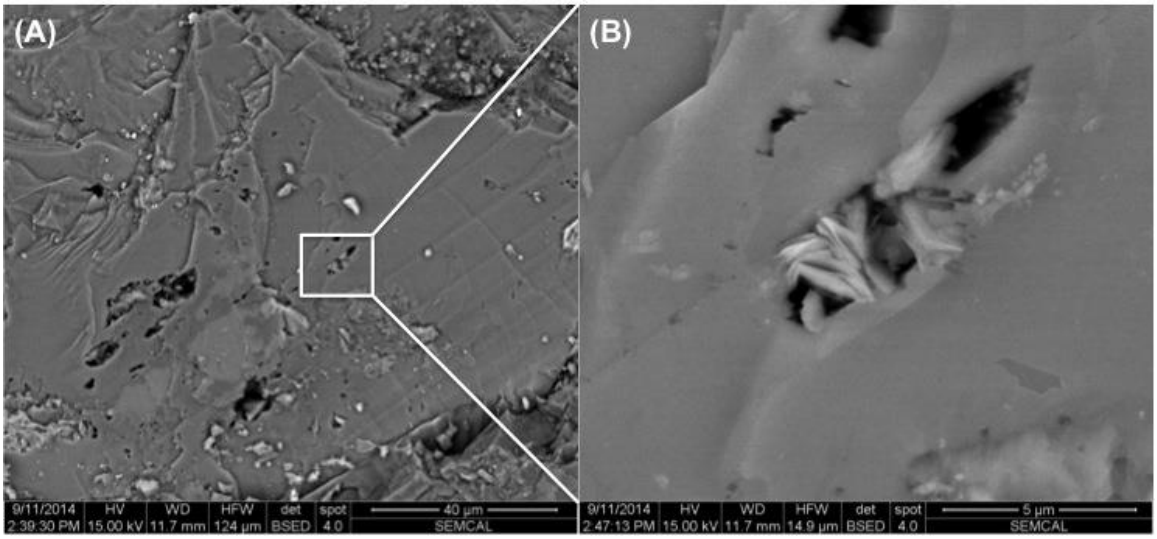

Figure 45. BSE images showing etch pits within a plagioclase grain from Navy II well 42A-16 (2000-2010 ft). The white rectangle outlines the higher magnification image (B). Some pits are in filled with clay (B).

Aside from major minerals, some similarity of association between minerals and pores are found among minor minerals in terms of depths. Iron oxides are porous, compositionally complex and exhibit layered textures involving a mixture of limonite, magnetite, goethite, and hematite. As can be seen, Figure 46 goethite and limonite show relatively high ratios of relative contribution to pores (as normalized to their areas) at this depth as well as at other depth ranges, which is confirmed by study conducted by Anovitz et al. (2013).

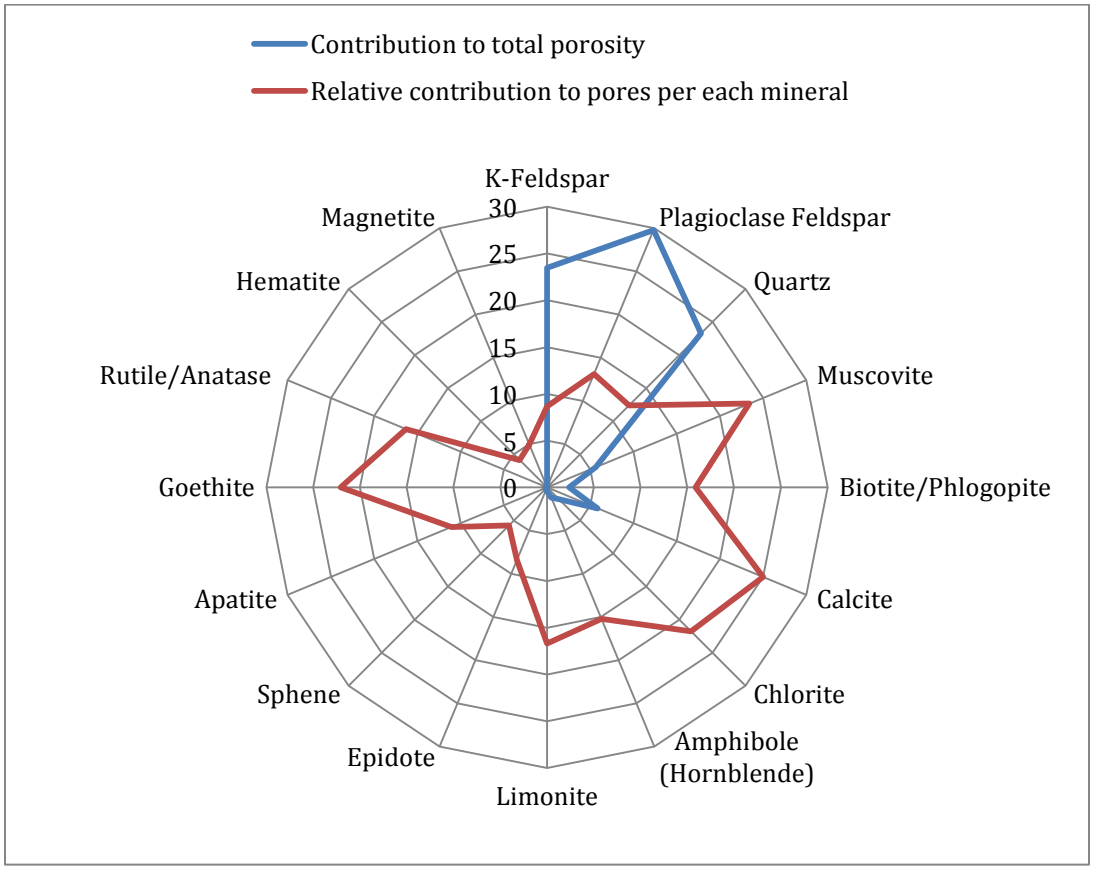

Figure 46. Association between mineralogy and pores and fractures for Navy II well 42A-16 (3000-3020 ft). Note that plagioclase, K-feldspar, and quartz are the major minerals to contribute porosity at this depth. Even though goethite and calcite are minor constituents, their contribution to porosity is non-trivial.

In addition, on a per area basis, calcite, chlorite and amphibole also have higher ratios of relative contribution to pores. At shallower intermediate depths (3000-6000 ft.) muscovite exhibits a higher ratio of relative contribution to pores (Figure 46, Figure 47), whereas at greater depths from 7000 to 8930 ft, apatite, rutile/anatase, and pyrite show higher ratios among minor minerals (Figure 48). Unlike the other depths, two samples,

from 8010-8040 ft and 8900-8930 ft (deepest) respectively, show relatively lower ratios of relative contribution to pores per each mineral of calcite and muscovite compared to pyrite and apatite along with the iron oxides (limonite). Additional diagrams are available for other depth ranges in Appendix C.

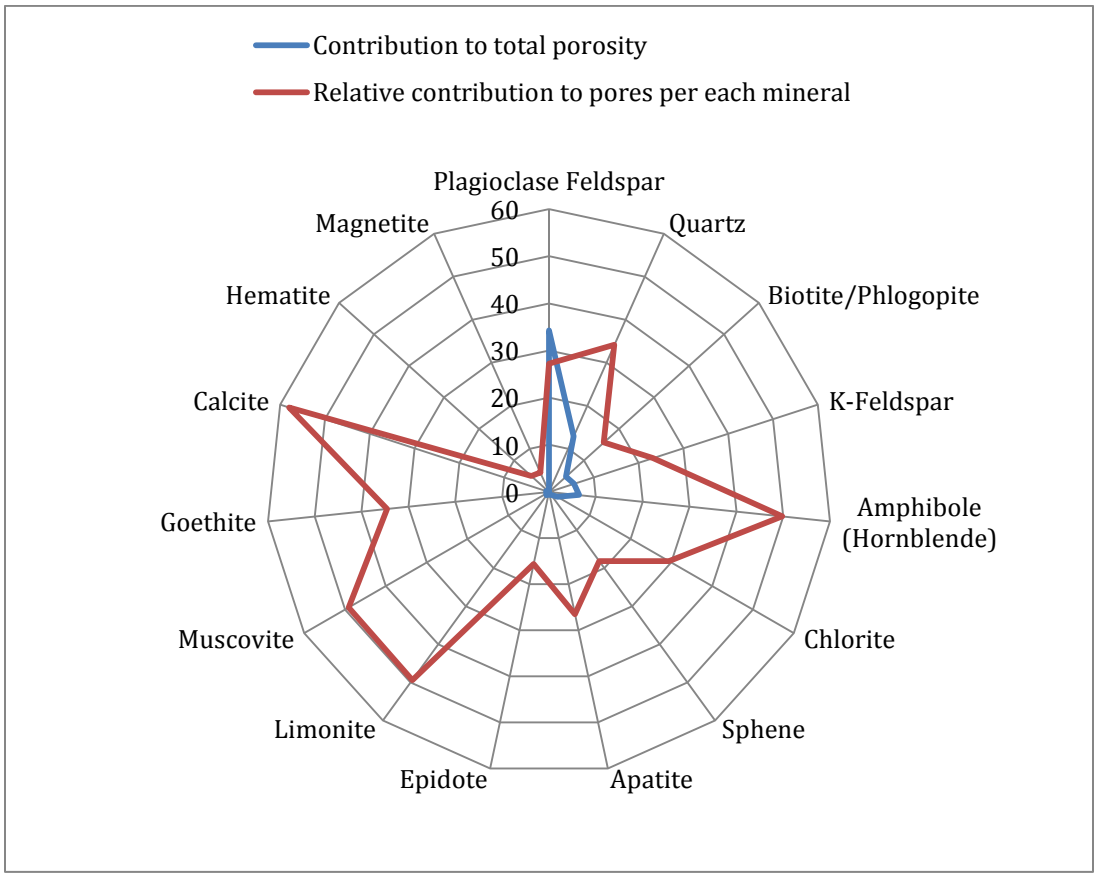

Figure 47. Association between mineralogy and pores and fractures for Navy II well 42A-16 (6000-6030 ft). Note that the higher ratio of having pores in calcite. Refer back to Figure 31 to see the textural relationships.

As described above, three samples covering the depth range from 7000 to 8940 ft, show a higher ratio of relative contributions to pores from minor minerals such as apatite, rutile/anatase, and pyrite. However, the efficacy of the approach can be called into questions. The extremely small size of cuttings makes it more difficult to distinguish between real pores in rocks and artificial pores from drilling and sampling processes. The availability of core samples would have eliminated this concern.

These radial diagrams give valuable insight into the relationship between porosity and mineralogy through a comparison of each mineral and how this contributes to open space as a function of different depths. The contribution to total porosity (blue lines) shows that plagioclase has the largest area percent of pores within the grains or adjacent to them. Relative contribution to pores (red lines) suggest that those minerals (e.g., calcite, select oxides) are associated with current pores/fractures and perhaps formed either at last stage of paragenesis or at the earlier stages but sealed in such a way as to prevent further mineralization.

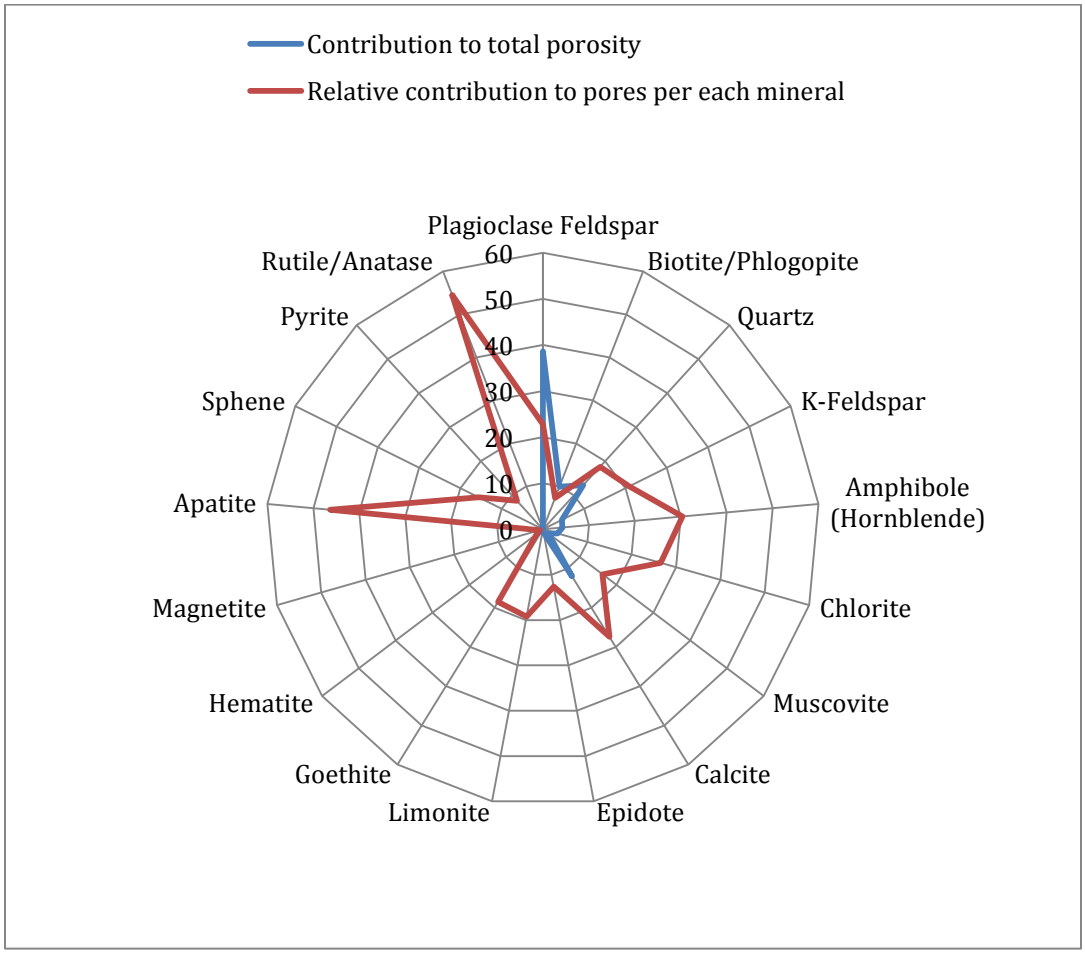

Figure 48. Association between mineralogy and pores and fractures for Navy II well 42A-16 (7000-7020 ft). Note that apatite, and rutile/anatase show higher ratio of pores adjacent to those minerals.

5.5 Porosity and Permeability

It is most certain that the assessment of porosity and permeability of the small rock fragments will be statistically valid only at these length scales and not at the macroscopic level measured on a larger sample such as core. Therefore, to obtain this macroscopic permeability from a single small fragment is unrealistic. However, we can

estimate the contribution of micro-sized pores and fractures to matrix porosity and connectivity. Although only small chips are used in this study, it may be possible to retrieve some useful information about current and past fracture porosity and permeability from representative samples. We used several analytical methods including nomogram, Mercury Intrusion Porosimetry (MIP), and Micro-Computed Tomography (Micro-CT) to complement the porosity data presented in Section 4.3. This is only a preliminary assessment that will require further quantification from the examination of many more chips using micro-CT and MIP.

A method of measuring porosity and permeability using a nomogram was presented by Norton and Knapp (1977). A nomogram is also called nomograph, which is a graphical calculation device with a set of scales. Norton and Knapp (1977) defined porosity of rocks by $\phi_{Total} = \phi_{Flow} + \phi_{Diffusion} + \phi_{Residual}$, wherein the major portion of total porosity in pluton environments typically consists of residual pores that are not interconnected to either flow or diffusion porosity. According to Norton and Knapp (1977) flow porosity (ϕ_{Total}) consists of the larger through-going fractures and pore-network "super highways" and diffusion porosity ($\phi_{Diffusion}$) involves pores connected to larger fractures or the pore network but are dead-ended (no through-way connection). Norton and Knapp (1977) report that total porosities of fractured igneous and welded volcanic rocks in hydrothermal systems range from 0.2 to 0.01 %, with diffusion porosities ranging from 10^{-3} to 10^{-5}, and flow porosities ranging from 10^{-3} to 10^{-5} based on synthesis of experimental data from the literature and field observations of fracture characteristics. According to their study of transport phenomena in hydrothermal systems,

permeability (k) may be defined as a function of flow porosity (ϕ_F), fracture abundance (n), and fracture aperture (d) (Figure 49).

Small-sized well cutting samples make it difficult to analyze fractures in this system, and it is not clear that whether the fractures observed in the samples are genuine fractures or fractures made by sampling processes. Thus, for this preliminary assessment calcite veins were used as indicators of former fracture permeability in the last stage of paragenesis (see Figure 40 and Figure 42).

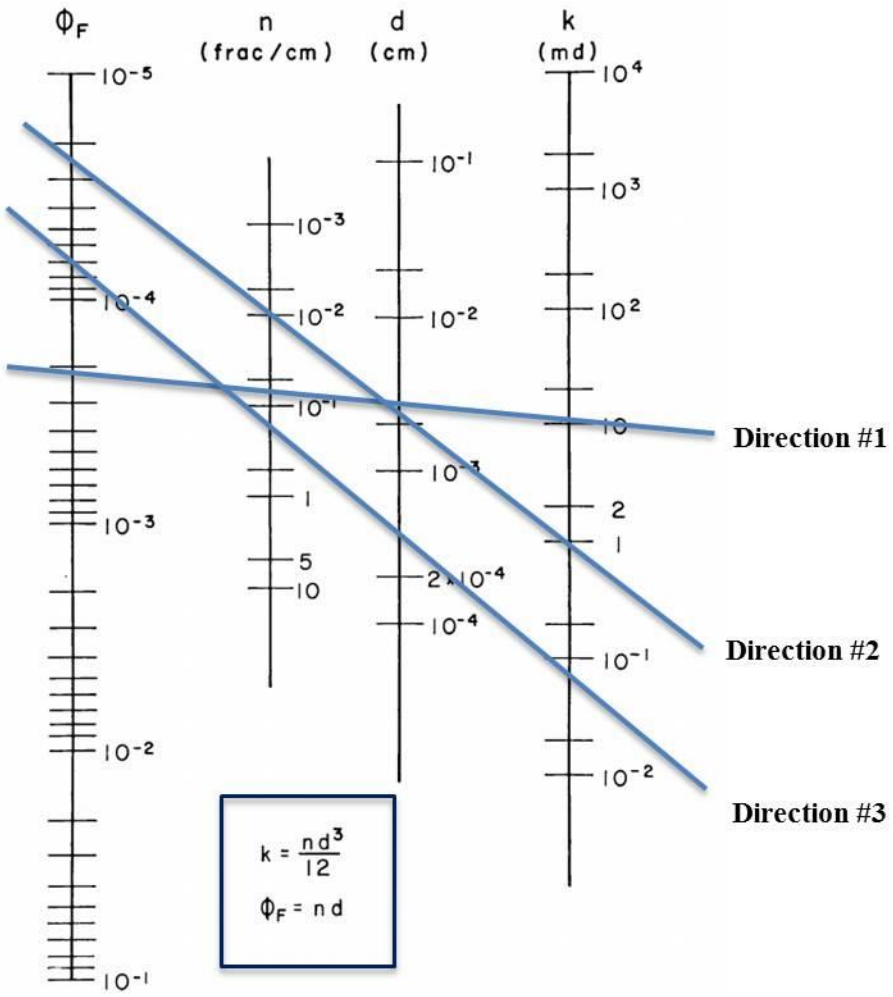

Figure 49. A nomogram which is designed to estimate porosity and permeability with parameters of porosity (ϕ_F), fracture abundance (n), and fracture aperture (d) based on two equations above. 'k' refers to permeability (millidarcy) (Norton and Knapp, 1977). Results of the nomogram in this study present in Table 7. Approximate porosity and permeability values estimated by nomogram

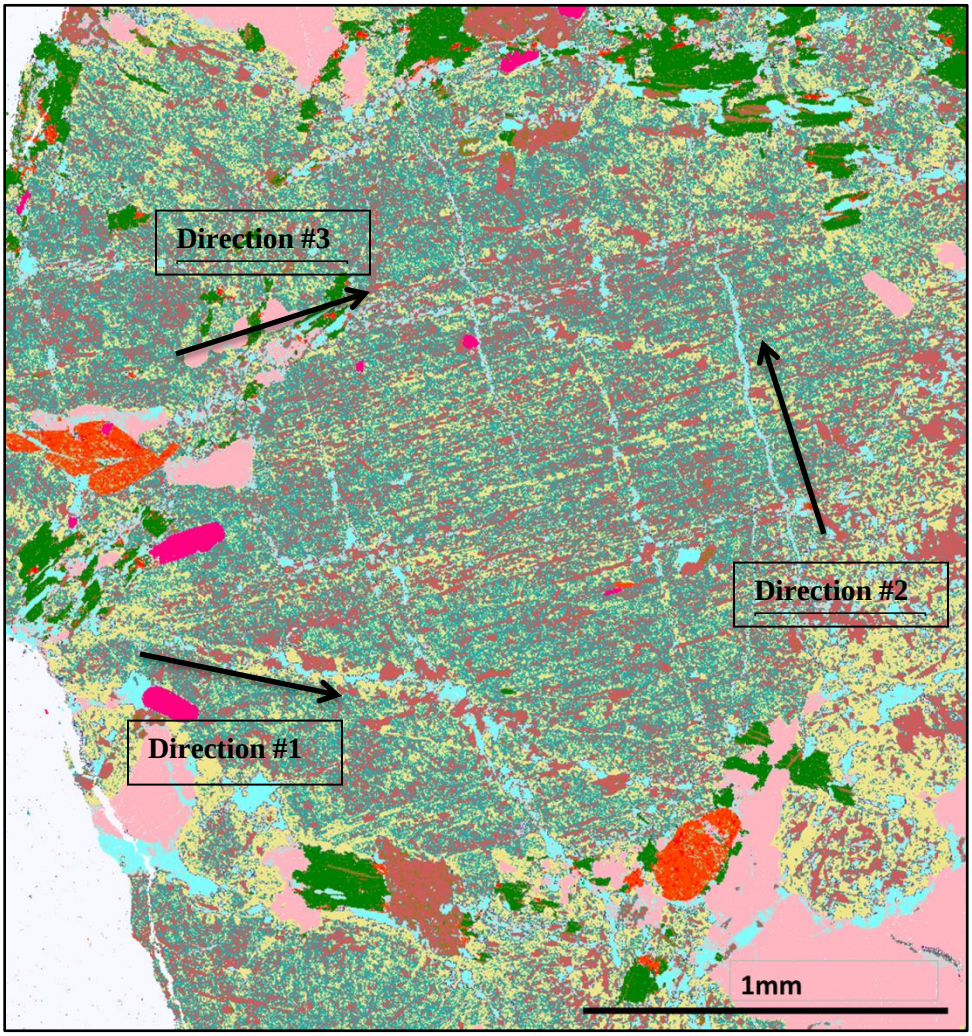

Figure 50. Example of QEMSCAN image in Coso Navy II well 42A-16 (5000-5020 ft) showing several alteration features including sericitization and calcite veins. This image has been used for nomogram calculation and is representative of other rock chips of similar size and alteration type.

Based on cross-cutting relationships of fractures in Figure 50 the fracture set of direction #1 formed earlier than that of direction #2. The relative age of the fracture set along the direction #3 may have formed earlier, but there is no clear evidence to

determine relative timing to other calcite veins. The calcite veins along fracture direction #1 tend to exhibit partial foliation affected by surrounding rocks showing that a recrystallization event occurred along the wall rocks of this fracture line, whereas the fracture sets of #2 and #3 show relatively clean and straight calcite veins, which also means that the temperature when this calcite precipitated may not be hot enough to change the surrounding foliation texture. By using the nomogram in Figure 49, the porosity, and permeability of each fracture set can be estimated shown in Table 7

Table 7. Approximate porosity and permeability values estimated by nomogram (Figure 49)

Fracture set	fracture abundance (n)	fracture aperture (d)	porosity (ϕ_F)	permeability (k)
Direction #1	8×10^{-2} (cm)	2.68×10^{-3} (cm)	2×10^{-4}	10 (md)
Direction #2	1.6×10^{-2} (cm)	2.08×10^{-3} (cm)	3×10^{-5}	1 (md)
Direction #3	0.6×10^{-2} (cm)	1.19×10^{-3} (cm)	7×10^{-5}	8×10^{-2} (md)

It is evident that fracture direction #1 yields greatest porosity and permeability out of three. Porosity generated by BET data and then corrected with rock density value in this sample was approximately 0.02, which is roughly 100 times larger than the porosity of direction #1. Therefore, flow (fracture) porosity in this type of sample is perhaps only a small portion of total connected porosity which likely consists of network of very small interconnected matrix pores.

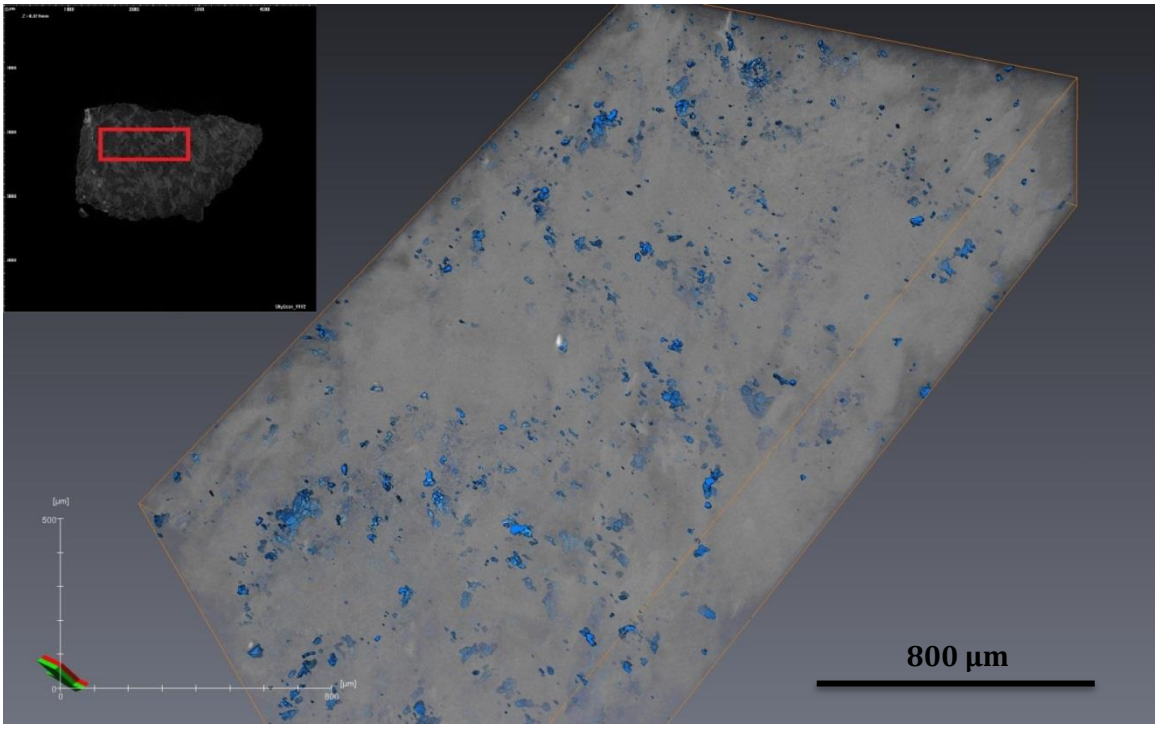

Figure 51. Preliminary mico-XCT image of a mafic sample chip from Navy II well (2000-2010 ft) showing pores throughout the well cutting (blue) in three dimensions. Data cropped to exclude exterior surfaces which contain more fractures and pores, possibly due to drilling damage.

To complement the pore assessment described above, MIP and micro-CT were used for selected samples, Navy II well 42A-16 1000 ft and 2000 ft respectively. MIP produced unexpectedly high porosity approaching 2% which may be caused by the fact that mercury is accessing artificial fractures observed via SEM on the edge of many sample chips. In other words, mercury porosimetry detects a contribution by fractures which are not real voids in the rock but produced by the drilling process. Although the

MIP method is very useful to produce reliable values of connected porosity, this method may not be appropriate for the small-sized well cuttings. On the contrary, micro-CT can be used to calculate total porosity comprised of flow porosity (ϕ_{Flow}), diffusion porosity ($\phi_{Diffusion}$), and residual porosity ($\phi_{Residual}$).

Image data were collected with a Skyscan 1172 micro-CT scanner, and raw data processed through Bruker Reconstruction software. The result (Figure 51) of micro-CT image shows unconnected (residual) porosity is dominant in the well cutting. One of the advantages of this analysis is that: 1) we can generate the porosity by the image processing to exclude exterior surfaces of the well cuttings to get more reliable porosity value, and 2) we can explain the relationship between porosity and mineralogy in three-dimension together with SEM and QEMSCAN analysis which can provide the mineralogical correction of the density values generated by micro-CT. Micro-CT is a great tool that can explain the physical characteristics of pores such as their shape and volume as a function of their distribution in minerals and rocks. Using AVIZO Fire software (not available at the time this was written), total porosity can be calculated with appropriate density values for rocks and pores. Future use of this tool will provide more reliable results correlated with other analytic methods for pore assessment in the Coso geothermal field. Especially, neutron scattering analysis also measured total porosity which includes flow, diffusion, and residual porosity to support micro-CT data. Therefore, this will be an important future research direction for the pore and mineral assessment for the Coso geothermal system.

Chapter 6: Summary and Conclusion

Mineralogy and micropore structure and pore connectivity are critical factors for estimating a number of reservoir properties including fluid characteristics, permeability, and geochemical and thermal feedbacks between the rock and the fluid. At Coso, various temperatures and fluid compositions have been documented for different periods of recent geothermal activity, as outlined in the background section above, but it is difficult to define to what extent the rock at depth and associated pore features have been affected by each specific episode. Therefore, this study focused on Navy II well 42A-16 alone with three other wells in the Coso geothermal field to characterize alteration mineralogy and the pore/fracture system to better define the evolution of the system.

Throughout this study, it has been confirmed that the most common rock types in this main well of interest are diorite to quartz-diorite and granodiorite. Granite is only encountered depth at 3000-5020 ft. and less altered than other rock types. This may be because the granites are a later-stage rock, having been exposed to hydrothermal fluids for a shorter duration of time. Mica schists have been found at 6000-6030 ft. which is the most abundant rock type in this depth range. Seven distinctive alteration types have been documented over the range of the depths covered by samples from in the Coso system: 1) albitization 2) potassic alteration 3) sericitization, 4) propylitic alteration, 5) carbonate alteration 6) silicification, and 7) oxidation. Alteration intensity appears to correlate with

the rock type and/or depth. Of these we observed that albitization and sericitization commonly occur together in quartz-diorite and granodiorite grains. Despite being able to only work with small chip samples, a mineral paragenetic sequence is constructed. The general trend of paragenesis is as follows: the earliest minerals to form were epidote, titanite, rutile/anatase, and chlorite (perhaps earlier metamorphic origin); albite and sericite dominate the middle of the paragenetic sequence with late stage alteration consisting primarily of calcite.

Through the application of six different geothermometers to fluid chemistries documented in the literature, we found that the Na-K-Ca geothermometer was effective in estimating reservoir temperatures and yielded a range of 220-265°C which is also in good agreement with Na-K geothermometer estimates, as well as the present day downhole temperatures. These results indicated that the modern-day geothermal fluids are likely "rock" buffered wherein the feldspar mineralogy, which dominates much of the rock either as primary or alteration phases, controls the water-rock interaction.

Activity diagrams were also generated to examine how the thermodynamic stability fields of key phases change as a function of temperature in the Coso geothermal system. Overall, in terms of the water-rock interaction process, the phase diagrams provide insight into how the various alteration assemblages, as defined by phase boundaries or triple points junctions, vary as a function of chemical system and temperature. A next logical step for a future effort is to conduct a fluid speciation study to see how fluid chemistries map over onto these phase diagrams to test the extent of equilibration of the fluid with the host mineralogy.

Among the minerals in this system, plagioclase has the largest area percent of pores within the grains or adjacent to them. Relative contribution to pores suggest that calcite and oxides are associated with current pores/fractures and perhaps formed either at the last stage of paragenesis or at the earlier stages but sealed in such a way as to prevent further mineralization. For the pore assessment, NS and BET methods were used to interrogate the data which sheds light on different aspect of porosity. A simple nomogram was used to calculate the flow porosity and permeability using different directions of calcite filled veins to assess the late stage porosity and permeability. Preliminary micro-CT analysis confirmed the observation that matrix porosity is indeed very small and for the most part unconnected.

Therefore, we can conclude that the Coso geothermal field is a rock buffered system, where connected (effective) porosity is generally a very small fraction of the total porosities. The alteration mineralogy evolved over a temperature range from as high as 300-325^{o}C to perhaps as low as 200^{o}C. The vertical alteration zoning pattern so common to many geothermal systems was not as well developed at the Coso field, but there was certainly a reasonably definitive paragenetic sequence of mineralization that varied somewhat depending on where you were in the producing part of the system.

In terms of future avenues for research these could include: 1) micro-CT studies to obtain more information about different type of porosity (connected and unconnected) and its distribution with regard to minerals and rocks with the support of SEM and QEMSCAN analysis; 2) thermodynamic fluid speciation calculation to determine how fluid activity relations map over to the phase diagrams to test the extent of water-rock

equilibration and assess how temperature controls the type of mineralization observed in the system.; 3) development of a water-rock model of the system that takes into account reactive transport behavior as a function of temperature-pressure-composition-space-time.

References

Adams, M. C., Moore, J. N., Bjornstad, S., and Norman, D. I., 2000. Geologic history of the Coso geothermal system. *Geothermal Resources Council Transactions*, vol. 24, p. 205–209.

Anovitz, M. C., Rother, G., Cole, D. R., 2011. Characterization of Rock Pore Features in Geothermal Systems Using Small Angle Neutron Scattering (SANS). *Proceedings of the 36th workshop on geothermal reservoir engineering, Stanford University*, CA.

Anovitz, L. M., Cole, D. R., Faulder, D. D., Sheets, J., Wang, H.-W., Rother, G., Wasbrough, M., Hjelm, R., Hartl, M., Pipich, V., and Fu, Z., 2013. Analysis of Multiscale Porosity at the Coso Geothermal Field. *Proceedings of the 38th workshop on geothermal reservoir engineering, Stanford University*, CA.

Arnorsson, S., Gunnlaugsson, E., and Svavarsson, H., 1983. The chemistry of geothermal waters in Iceland. III. Chemical geothermometry in geothermal investigations. *Geochimica et Cosmochimica Acta*, vol. 47(3), p. 567-577.

Barrett, E. P., Joyner, L. G., and Halenda, P. P., 1951. The determination of pore volume and area distributions in porous substances. I. Computations from nitrogen isotherms. *Journal of the American Chemical Society*, vol. 73, p. 373-80.

Bashar, I. L., and Garba, I., 1999. An overview of VIS-NIR Laboratory spectroscopy technique as applied to the analysis of engineering index properties of a geologic material. http://www.specterra.net/files/50329239.pdf (Accessed 2014-10-25)

Bethke, C., 1992. The geochemist's workbench: A user's guide to Rxn, Act2, Tact, React, and Gtplot. C. Bethke.

Biscaye P. E., 1964. Distinction between Kaolinite and Chlorite in Recent Sediments by X-ray Diffraction. *The American Mineralogist*, vol. 49, p. 1281-1289.

Bishop, B. P. and D. K. Bird, 1987. Variation in Sericite Compositions from Fracture-Zones within the Coso Hot-Springs Geothermal System. *Geochimica et Cosmochimica Acta* vol. 51(5) p. 1245-1256.

Bove, D. J., Alisa Mast, M., Bradley Dalton, J., Wright, W. G., and Yager, D. B., 2007. Major styles of mineralization and hydrothermal alteration and related solid-and aqueous-phase geochemical signatures. *US Geological Survey professional paper*, (1651), p. 161-230.

Brown, D., 2000. A Hot Dry Rock geothermal energy concept utilizing supercritical CO2 instead of water. In: *Proceedings of the 25th Workshop on Geothermal Reservoir Engineering, Stanford University*, CA, p. 233–238.

Bustillo, M. A., and Alonso-Zarza, A. M., 2007. Overlapping of pedogenesis and meteoric diagenesis in distal alluvial and shallow lacustrine deposits in the Madrid Miocene Basin, Spain. *Sedimentary Geology*, v. *198*(3), p. 255-271.

Carmichael, R. S., 1990. Practical handbook of physical properties of rocks and minerals: Boca Raton, Florida. CRC Press, Inc., p. 741.

Cathelineau, M., 1986. The hydrothermal alkali metasomatism effects on granitic rocks: quartz dissolution and related subsolidus changes. *Journal of Petrology*, vol. 27(4), p. 945-965.

Chung, F. H., 1974. Quantitative interpretation of X-ray diffraction patterns, I. matrix-flusing method of quantitative multicomponent analysis. *Journal of Applied Crystallography*, vol. 7, p. 513-519.

Combs, J., 1980. Heat flow in the Coso geothermal area, Inyo County, California. *Journal of Geophysical Research.* vol. 85, p. 2411–2424.

Damian, F., 2012. The mineralogical characteristics of the hydrothermal types alteration from Nistru ore deposit, Baia Mare metallogenetic district. *Studia UBB*, Geologia, vol. 48(1), p. 101-112.

Davatzes, N. C., and Hickman, S. H., 2010. The Feedback Between Stress, Faulting, and Fluid Flow: Lessons from the Coso Geothermal Field, CA, USA. *Proceedings World Geothermal Congress* Bali, Indonesia, p. 25-29.

Delany, J. M., and Lundeen, S. R., 1990. The LLNL thermochemical database. *Lawrence Livermore National Laboratory Report* UCRL-21658, p. 150.

Duffield, W. A., Bacon, C. R., and Dalymple, G. B., 1980. Late Cenozoic Volcanism, Geochronology, and the structure of the Coso Range, Inyo County, California. *Journal of Geophysical Research*, vol. 85, p. 2381-2404.

Ernst, W. G., 1963. Significance of phengitic micas from low-grade schists. *American Mineralogist*, vol. 48(11-2), p. 1357.

Etzel, T. M., Bowman, J. R., McCulloch, J. M., Moore, J. N., Spicuzza M. J., and Valley J. W., 2013. Oxygen Isotopic Evidence of Water-Rock Interaction in the Coso Geothermal System, *Proceedings of the 38th Workshop on Geothermal Reservoir Engineering, Stanford University*, CA.

Fialko, Y., and Somons, M., 2000. Deformation and seismicity in the Coso geothermal area, Inyo County, California: Observations and modeling using satellite radar interferometry. *Journal of Geophysical Research*, vol. 105, p. 21,781-21,793.

Fouillac, C. and Michard, G., 1981. Sodium/Lithium ratio in water applied to geothermometry of geothermal reservoirs. *Geothermics,* vol. 10, p. 55-70.

Fournier, R. O., 1977. Chemical geothermometers and mixing models for geothermal systems. *Geothermics*, vol. 5(1), p. 41-50.

Fournier, R. O. 1979. A revised equation for the Na/K geothermometer. *Geothermal Resources Council Transactions.* vol. 3, p. 221-224.

Fournier, R. O. 1980. Application of water geochemistry to geothermal exploration and reservoir Engineering. *In Geothermal systems: Principles and case histories* Edited by L. Rybach and L. P., Muffler, John Wiley a Sons Ltd., p. 109-143.

Fournier, R. O., and Potter R. W.II, 1979. Magnesium correction to Na-K-Ca geothermometer. *Geochimica et Cosmochimica Acta*, vol. 43, p. 1543-1550.

Fournier, R. O., Thompson, J. M., and Austin, C. F., 1980. Interpretation of chemical analyses of waters collected from two geothermal wells at Coso, California. *Journal of Geophysical Research*, vol. 85, p. 2405-2410.

Fournier, R. O., and Truesdell, A. H., 1973. An empirical Na-K-Ca geothermometer for natural waters. *Geochimica et Cosmochimica Acta*, vol. 37, p. 1255-1275.

Giggenbach W. F., 1988. Geothermal solute equilibria. *Geochimica et Cosmochimica Acta* , vol. 52, p. 2749 -2765.

Giggenbach, W. F., 1997. The origin and evolution of fluids in magmatic-hydrothermal systems. *In Geochemistry of Hydrothermal Ore Deposits* 3rd ed. H. L. Barnes, New York, Wiley-interscience, p. 737-796.

Goff, F., Bergfeld, D., and Janik, C. J., 2002. Geochemical Data on Waters, gases, scales, and rocks from the Dixie Valley Region, Nevada (1996-1999) (No. LA-13972-

MS). DOEEEGTP (USDOE Office of Energy Efficiency and Renewable Energy Geothermal Tech Pgm).

Hanaor, D. and Sorrell, C., 2011. Review of the anatase to rutile phase transformation. *Journal of Materials Science*, vol. 46, p. 1–20.

Hauksson, E. and J. Unruh, 2007. Regional tectonics of the Coso geothermal area along the intracontinental plate boundary in central eastern California: Three-dimensional V-p and V-p/V-s models, spatial-temporal seismicity patterns, and seismogenic deformation. *Journal of Geophysical Research-Solid Earth* vol. 112(B6).

Huddlestone-Homes, C. R., and Hayward, J., 2011. The Potential of geothermal energy. CSIRO report prepared as infut to the Garnaut Review Update. Available at http://www.garnautreview.org.au/update-2011/commissioned-work/potential-of-geothermal-energy.pdf (Accessed 2014-10-25)

IUPAC. 1985. Reporting Physiosorption Data for Gas/Solid Systems with Special Reference to the Determination of Surface Area and Porosity, *Pure and Applied Chemistry*, vol. 57(4), p. 603-619.

Julian, B. R., Foulger, G. R., Monastero, F. C., and Bjornstad, S., 2010. Imaging hydraulic fractures in a geothermal reservoir, *Geophysical Research Letters*, vol. 37, p. 1-5.

Karingithi, C. W., 2009. Chemical Geothermometers for Geothermal Exploration, Short Course IV on Exploration for Geothermal Resources, Kenya, 1-22, Nov. 2009.

Kovac, K. M., Moore, J. N., McCulloch, J., and Ekart, D., 2004. Geology and Mineral Paragenesis Study Within the Coso-EGS Project, *Proceedings, 29th Workshop on geothermal Reservoir Engineering, Stanford University*, CA, p. 262-267.

Kovac, K. M., Moore, J. N., and Lutz, S. J., 2005. Geologic Framework of the East Frank, Coso Geothermal Field: Implication For EGS Development. *Proceedings of the 30th workshop on geothermal reservoir engineering, Stanford University*, CA.

Kurilovitch, L., Norman, D., Heizler, M., Moore, J., and McCulloch, J., 2003. 40Ar/39Ar Thermal History of the Coso Geothermal Field, *Proceedings, 28th Workshop on Geothermal Reservoir Engineering, Stanford University*, CA, 110-116.

Lagat, J., 2007. Hydrothermal alteration mineralogy in geothermal fields with case examples from Olkaria domes geothermal field, Kenya. *Short Course II on Surface Exploration for Geothermal Resources.* Organized by UNU-GTP and KenGen, at Lake Naivasha, Kenya, p. 2-17.

Lees, J. M., and Wu, H. T., 2000. Poisson's ratio and porosity at Coso geothermal area, California. *Journal of Volcanology and Geothermal Research*, vol. 95(1-4) p. 157-173.

Manley, C. R., and Bacon, C. R., 2000. Rhyolite thermobarometry and the shallowing of the magma reservoir, Coso Volcanic Field, California. *Journal of Petrology*, vol. 41, p.149–174.

McLin, K. S., 2012. Evaluating fluid-rock interactions in geothermal and contact metamorphic systems. THE UNIVERSITY OF UTAH.

Merino, E., 1975. Diagenesis in Tertiary sandstones from Kettleman North Dome, California: I. Diagenetic mineralogy: *Journal of Sedimentary Petrology*, vol. 45, p. 320–336.

Mitchell, P. C. H., Bowker, M., Price, N., Poulston, S., James, D., and Parker, S. F., 2000. Iron antimony oxide selective oxidation catalysts–an inelastic neutron scattering study. *Topics in Catalysis*, vol. 11(1-4), p. 223-227.

Monastero, F. C. 2002. An Overview of Industry–Military Cooperation in the Development of Power Operations at the Coso Geothermal Field in Southern California. *Geothermal Resources Council Bulletin*, vol. 31 p.188-194.

Monastero, F. C., Katzenstein, A. M., Miller, J. S., Unruh, J. R., Adams, M. C., and Richards-Dinger, K., 2005. The Coso geothermal field: A nascent metamorphic core complex. *Geological Society of America Bulletin*, v. 117, no. 11-12, p. 1534-1553.

Moore, D. M., and Reynolds Jr, R. C., 1997. Sample Preparation Techniques for Clay Minerals, X-ray Diffraction and the Identification and Analysis of Clay Analysis. Oxford, Oxford University Press, p. 204–226.

Newman, G. A., Gasperikova, E., Hoversten, G. M., and Wannamaker, P. E., 2008. Three-dimensional magnetotelluric characterization of the Coso geothermal field. *Geothermics*, vol. 37, p. 369–399.

Norton, D., and Knapp, R., 1977. Transport phenomena in hydrothermal systems; the nature of porosity. *American Journal of Science*, vol. 277(8), p. 913-936.

Pruess, K., 2006. Enhanced geothermal systems (EGS) using CO2 as working fluid—A novel approach for generating renewable energy with simultaneous sequestration of carbon. *Geothermics*, vol. 35, p. 351–367.

Passchier, C. W., and Trouw, R. A., 1996. Microtectonics. vol. 256. Berlin: Springer.

Que, M., and Allen, A. R., 1996. Sericitization of plagioclase in the Rosses granite complex, Co. Donegal, Ireland. *Mineralogical Magazine*, vol. *60*(403), p. 927-936.

Reasenberg, P., Ellsworth, W., and Walter, A., 1980. Teleseismic evidence for a low-velocity body under the Coso geothermal area. *Journal of Geophysical Research*, vol. 85(5), p. 2471-2483.

Reed, M. H., 1997. Hydrothermal Alteration and its Relationship to Ore Fluid Composition, *In Geochemistry of Hydrothermal Ore Deposits* 3rd ed. H. L. Barnes, New York, Wiley-interscience, p. 303-365.

Reyes, A. G., 1990. Petrology of Philippine geothermal systems and the application of alteration mineralogy to their assessment. *Journal of Volcanology and Geothermal Research*, vol. 43(1), p. 279-309.

Rose, P., Barton, C., McCulloch, J., Moore, J. N., Kovac, K., Sheridan, J., and Berard, B., 2003. The Coso EGS Project-Recent Developments. *Transactions-Geothermal Resources Council*, p. 879-884.

Schettler, G., Oberhänsli, H., Stulina, G., and Djumanov, J. H., 2013. Hydrochemical water evolution in the Aral Sea Basin. Part II: Confined groundwater of the Amu Darya Delta – Evolution from the headwaters to the delta and SiO_2 geothermometry. *Journal of hydrology*, vol. 495, p. 285–303.

Siivola, J., and Schmid, R., 2007. List of mineral abbreviations. Metamorphic Rocks: A Classification and Glossary of Terms. Recommendations of the International Union of Geological Sciences Subcommission on the Systematics of Metamorphic Rocks, p. 93-110.

Sobash, V. P., Sabin, A., and Liedke Jr., T. R., 2014. The Power of Geothermal. The military of Engineer, 2014-4-25. http://themilitaryengineer.com/index.php/tme-articles/tme-magazine-online/item/312-the-power-of-geothermal. (Accessed 2014-9-25)

Strens, R. G. J., 1964. Epidotes of the Borrowdale volcanic rocks of central Borrowdale. *Mineral. Mag*, vol. 33, p. 868-886.

Swift, A. M., Anovitz, L. M., Sheets, J. M., Cole, D. R., Welch, S. A., and Rother G., 2014. Relationship between mineralogy and porosity in seals relevant to geologic CO_2 sequestration. *Environmental Geosciences*, vol. 21, p. 39-57.

Telford, W. M., Geldart, L. P., Sheriff, R. E., and Keys, D. A., 1976. Applied geophysics: Cambridge, UK, Cam- bridge University Press, p. 860.

Walter, A.W., and Weaver, C. S., 1980. Seismicity of the Coso Range, California. *Journal of Geophysical Research*, vol. 85(5), p. 2441-2458.

Williams, C. F., Reed, M. J., Mariner, R. H., DeAngelo, J., and Galanis, S. P., 2008. Assessment of Moderate- and High-Temperature Geothermal Resources of the United States. *U.S. Geological Survey Fact Sheet* 2008-3082, p. 4.

Wilson, C. K., Jones, C. H., and Gilbert, H. J. 2003. Single-chamber silicic magma system inferred from shear wave discontinuities of the crust and uppermost mantle, Coso geothermal area, California. *Journal of Geophysical Research-Solid Earth* vol. 108(B5).

Appendix A: Comparison of XRD and QEMSCAN Data.

XRD values reflect mass fractions as percentages; QEMSEM values reflect percentage of scan area. * refers to normalized to 100% excluding minerals less than 0.5% and some other minor minerals.

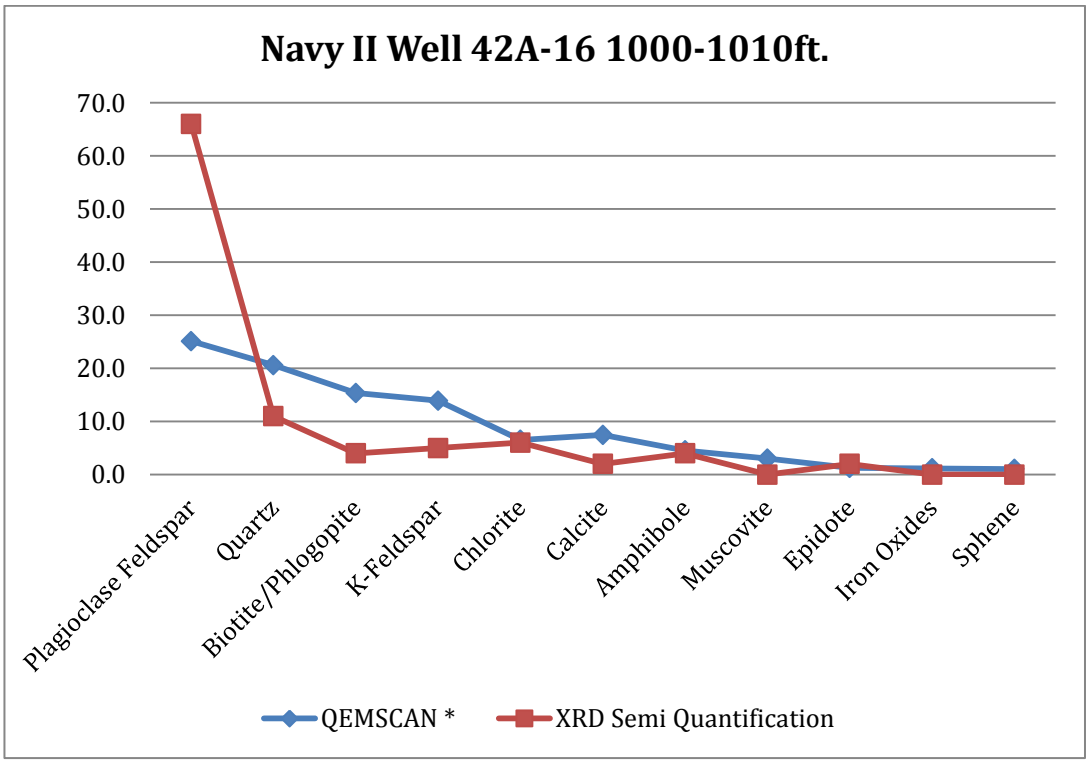

Figure 52. Comparison of XRD and QEMSCAN data (Navy II well 42A-16; 1000-1010 ft)

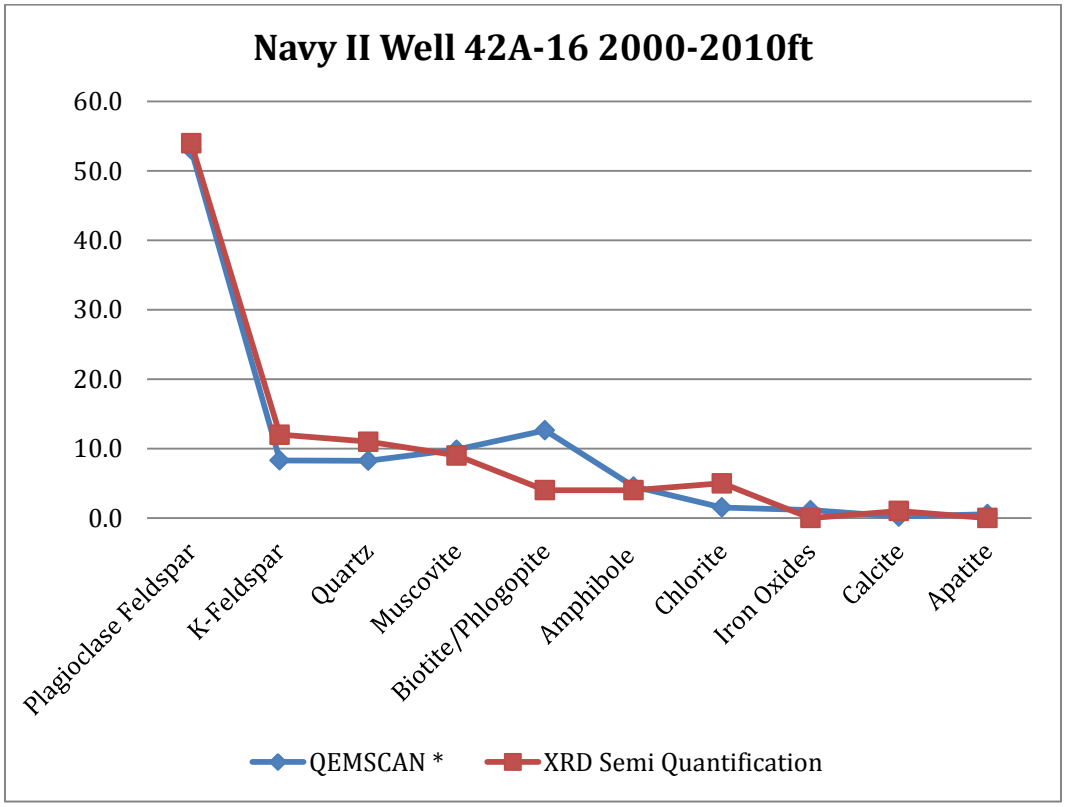

Figure 53. Comparison of XRD and QEMSCAN data (Navy II well 42A-16; 2000-2010 ft)

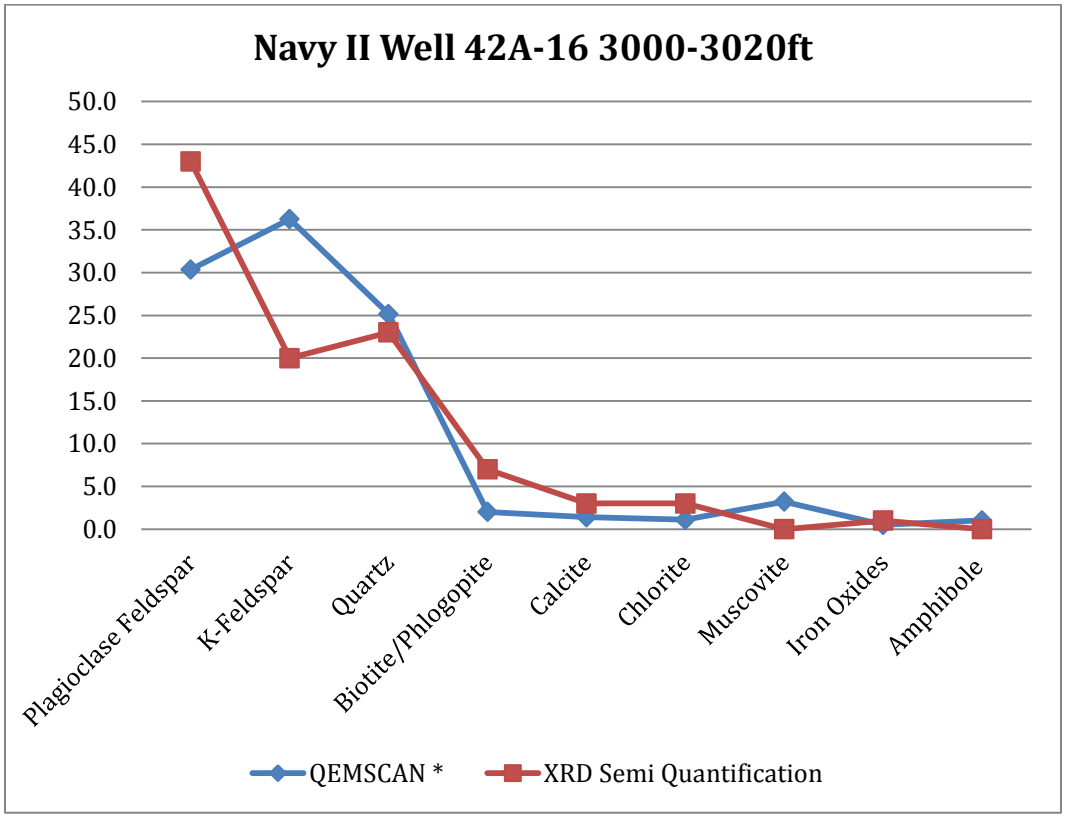

Figure 54. Comparison of XRD and QEMSCAN data (Navy II well 42A-16; 3000-3020 ft)

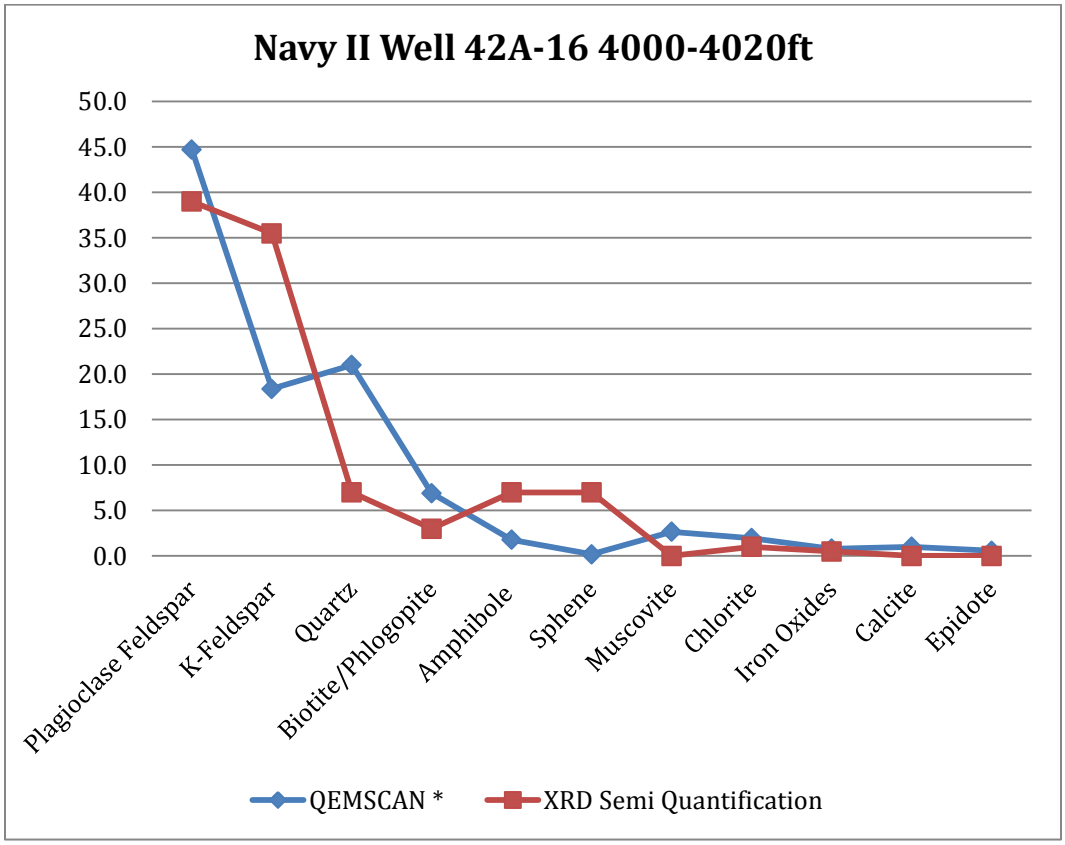

Figure 55. Comparison of XRD and QEMSCAN data (Navy II well 42A-16; 4000-4020 ft)

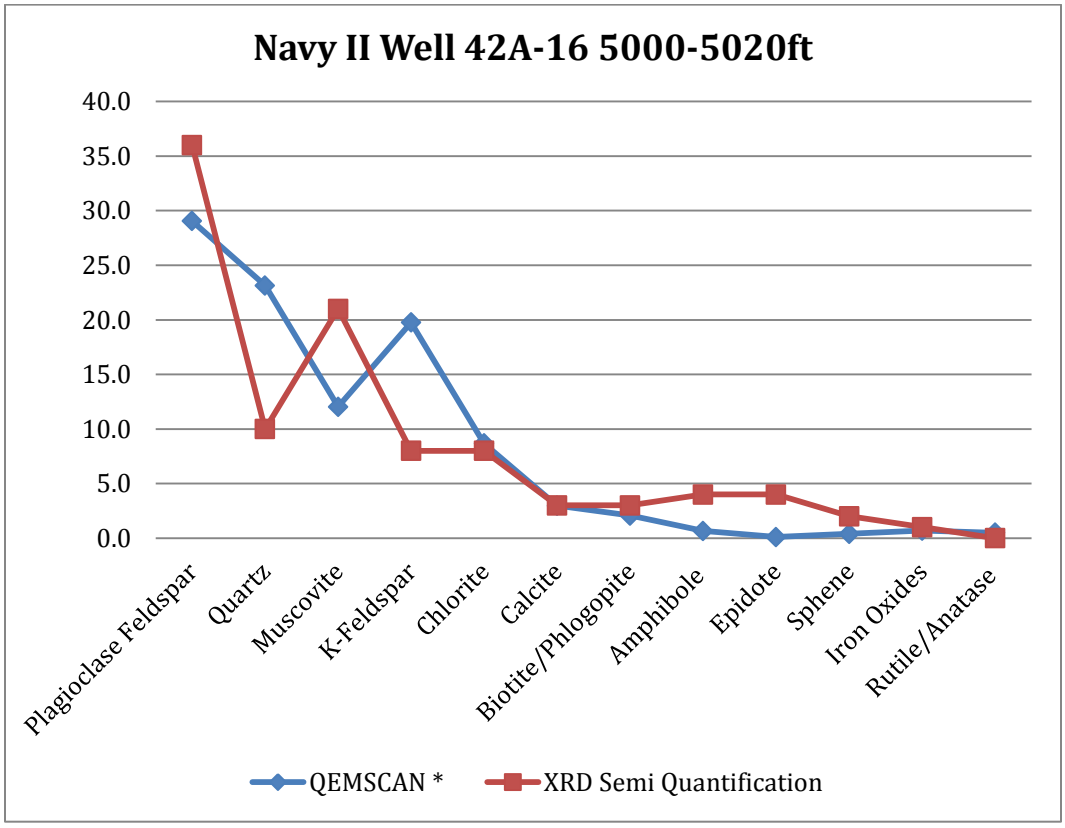

Figure 56. Comparison of XRD and QEMSCAN data (Navy II well 42A-16; 5000-5020 ft)

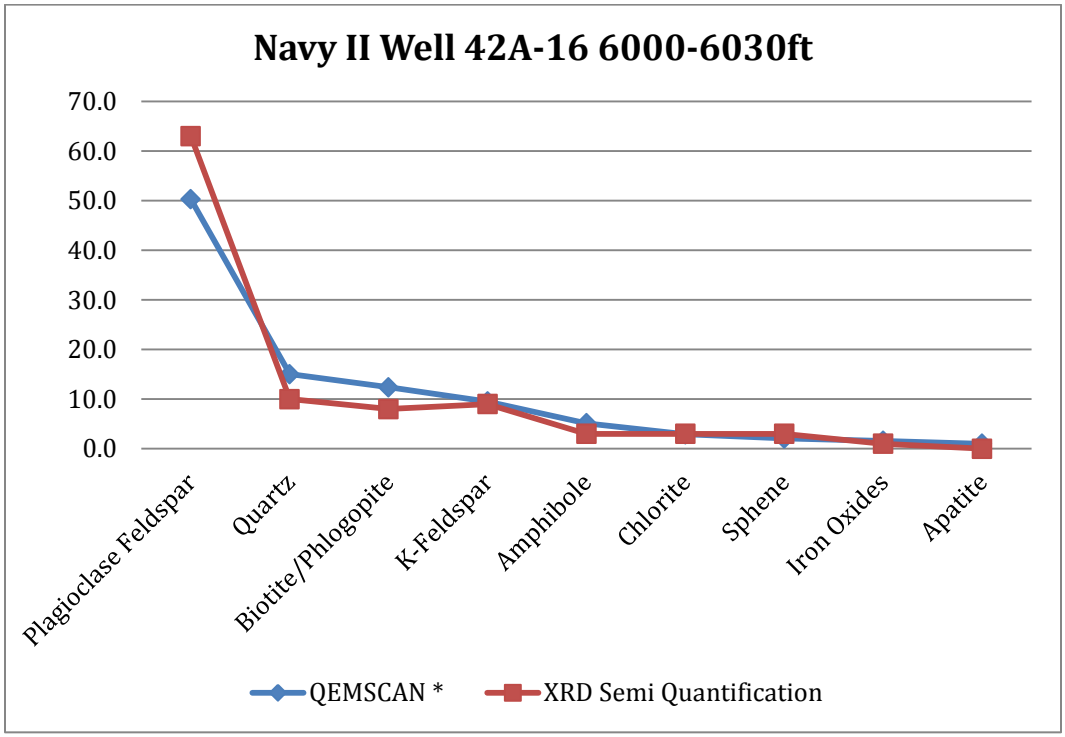

Figure 57. Comparison of XRD and QEMSCAN data (Navy II well 42A-16; 6000-6030 ft)

Note: QEMSCAN data shows that approximatly 14% of area is wollastonite and 33% of that is others (Ca, Si, and O are dominant and minor Fe, Mg detected by energy dispersive spectroscopy (EDS)). Despite its significant amounts, there is still not enough evidences to support this results. For that reason, this figure excludes both of them in total percentage, and then nomalized to 100% .

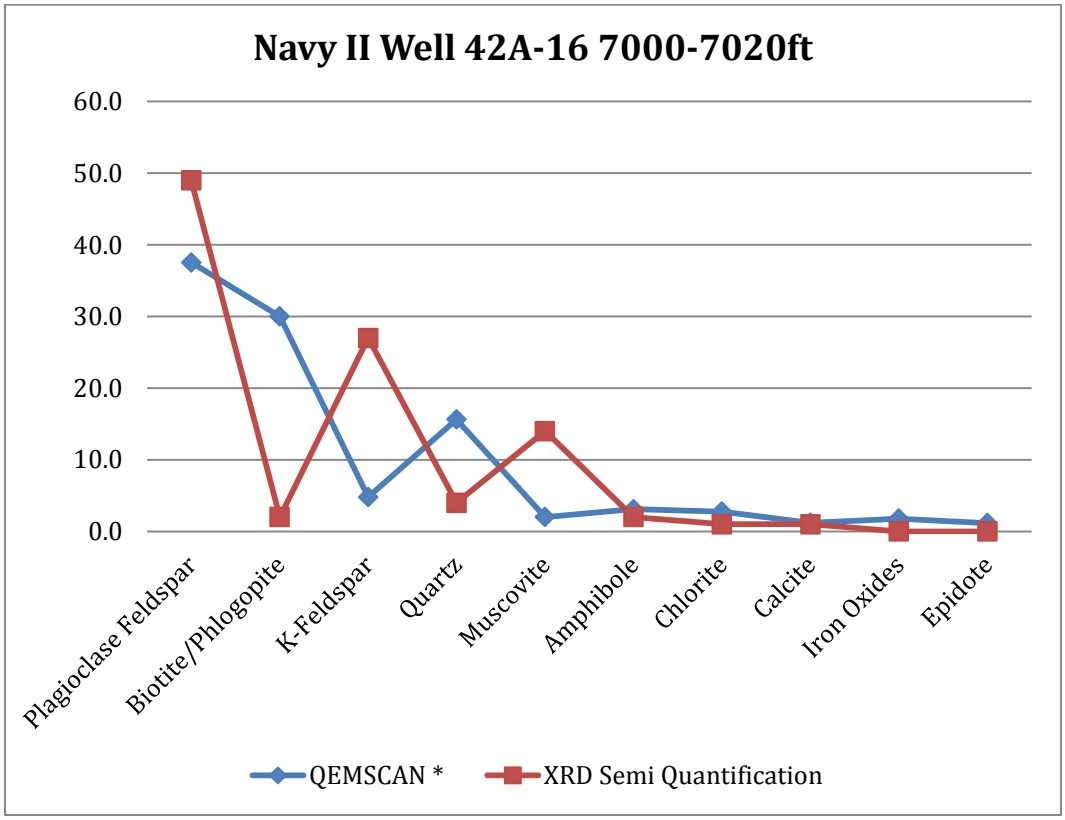

Figure 58. Comparison of XRD and QEMSCAN data (Navy II well 42A-16; 7000-7020 ft)

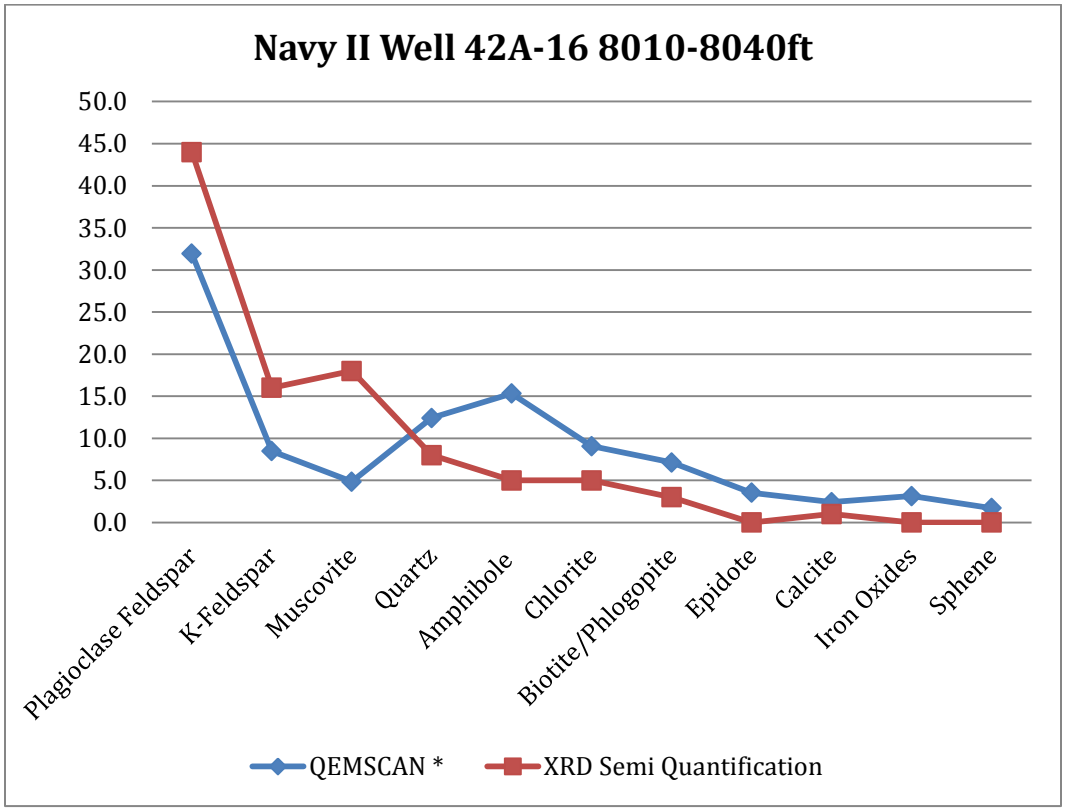

Figure 59. Comparison of XRD and QEMSCAN data (Navy II well 42A-16; 8010-8040 ft)

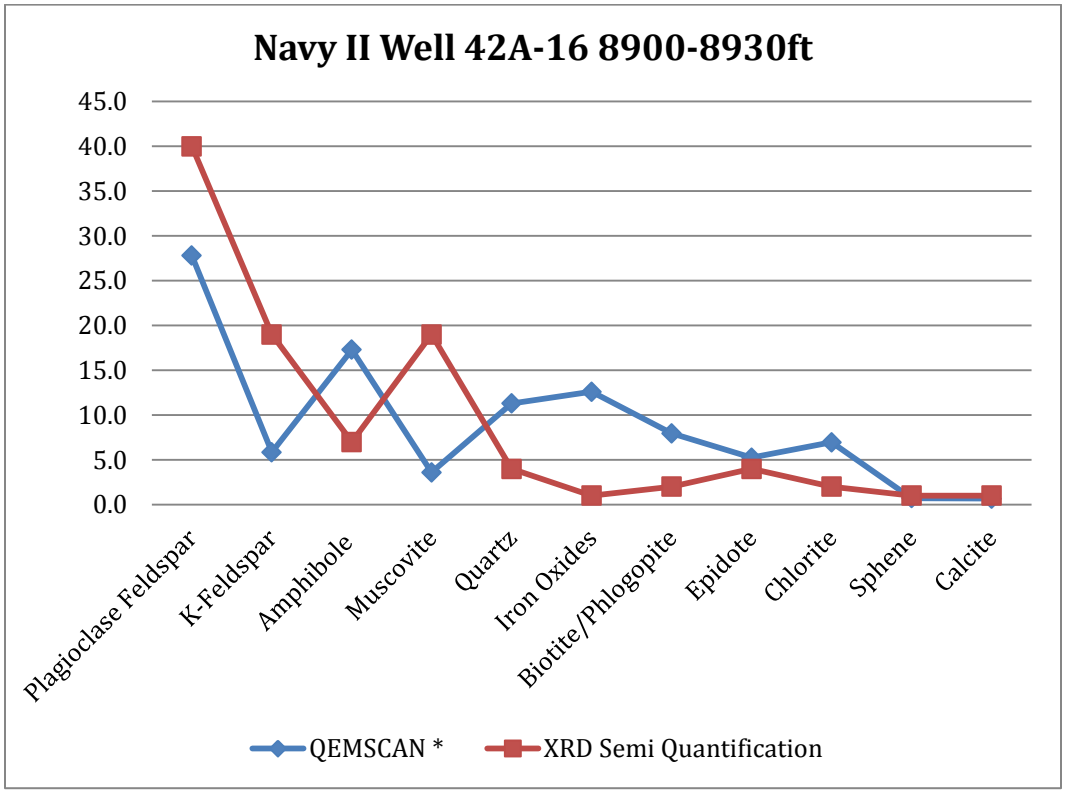

Figure 60. Comparison of XRD and QEMSCAN data (Navy II well 42A-16; 89000-8930 ft)

Note: Iron Oxides showing here indicate different minerals between two methods. First of all, QEMSCAN data shows that each iron oxides, limonite (5.2%), goethite (3.2%), hematite (1%), and magnetite (0.8%), are composed of the total area percent of the iron oxides (10.2%) and normalized up to 12.6% out of total scanned area excluding minor minerals. XRD semi quantification, however, exhibits only magnetite (Fe_3O_4) which is 1% of the total volume.

Appendix B: List of Mineral Abbreviations

Abbreviations used here for petrographic images follow the paper authored by Siivola, J., and Schmid, R. (2007) which is recommendations by IUGS Subcommission on the Systematics of Metamorphic Rocks. In case of a mixture form of iron oxides mineral which is difficult to separate one another, this study abbreviate 'the mixture of iron oxides' by using 'Fe-ox'.

Mineral name	Abbreviation
Albite	Ab
Amphibole	Am
Apatite	Ap
Biotite	Bt
Calcite	Cal
Chlorite	Chl
Epidote	Ep
Gypsum	Gp
Iron oxides	FeOx
K-feldspar	Kfs
Mica	Mca
Monazite	Mnz
Muscovite	Ms
Plagioclase	Pl
Quartz	Qtz
Rutile/Anatas	Rt/A
Sericite	Ser
Titanite	Ttn
Zircon	Zrn

Appendix C: Association Diagrams between Mineralogy and Pores and Fractures

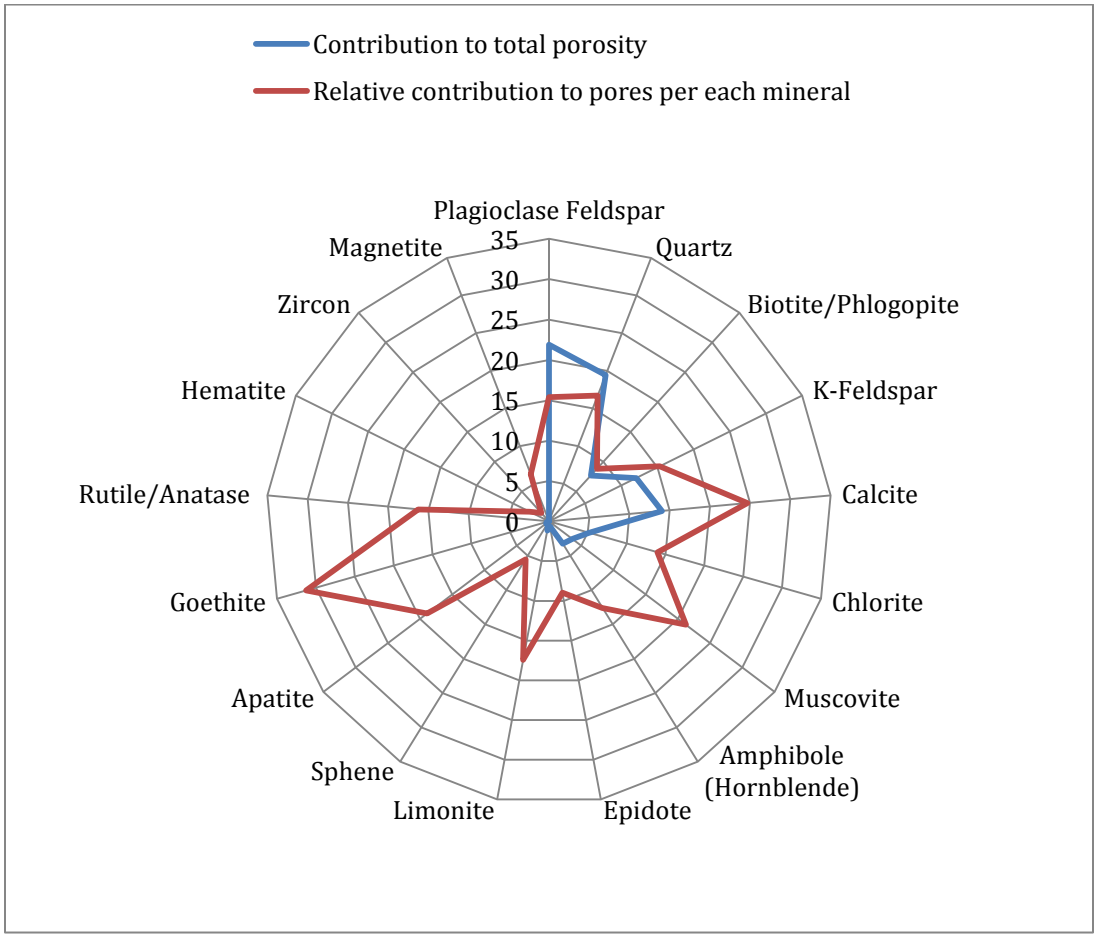

Figure 61. Association diagrams between mineralogy and pores and fractures (Navy II well 42A-16; 1000-1010 ft)

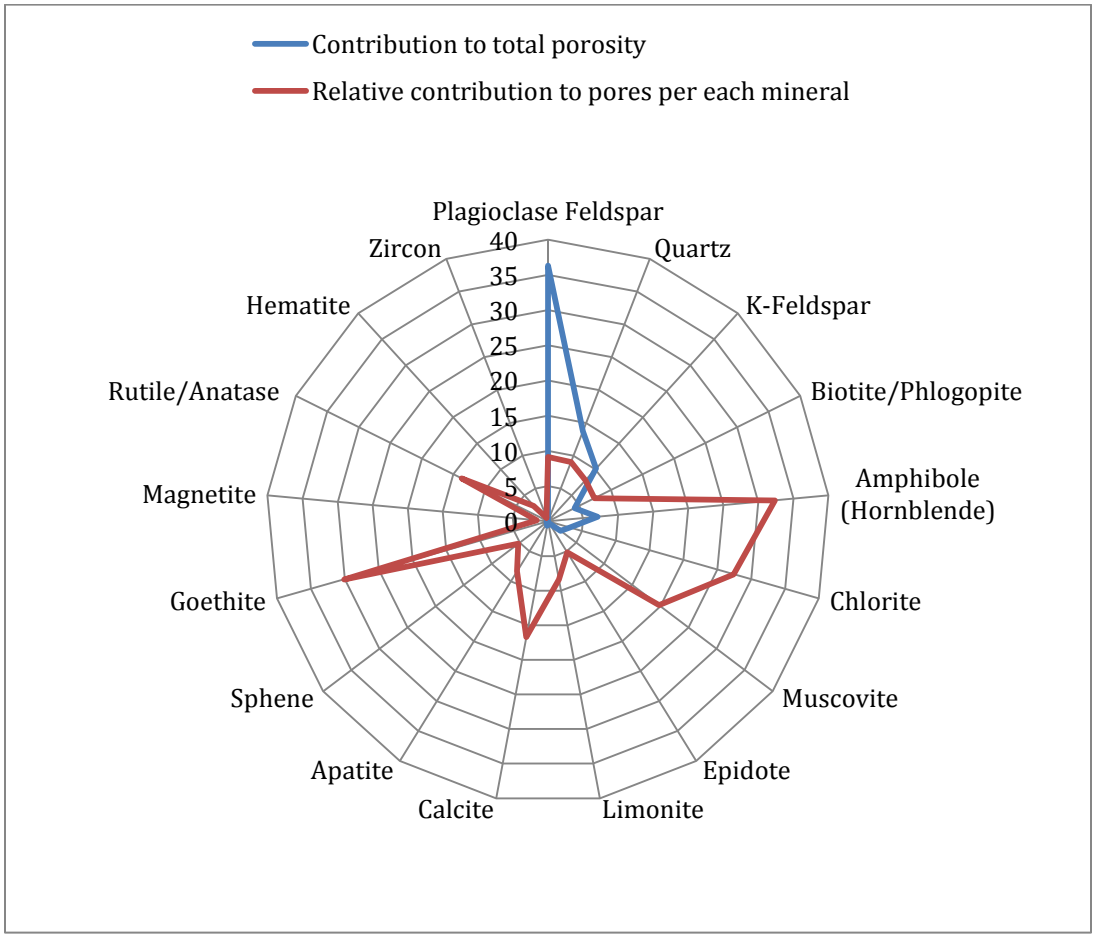

Figure 62. Association diagrams between mineralogy and pores and fractures (Navy II well 42A-16; 4000-4020 ft)

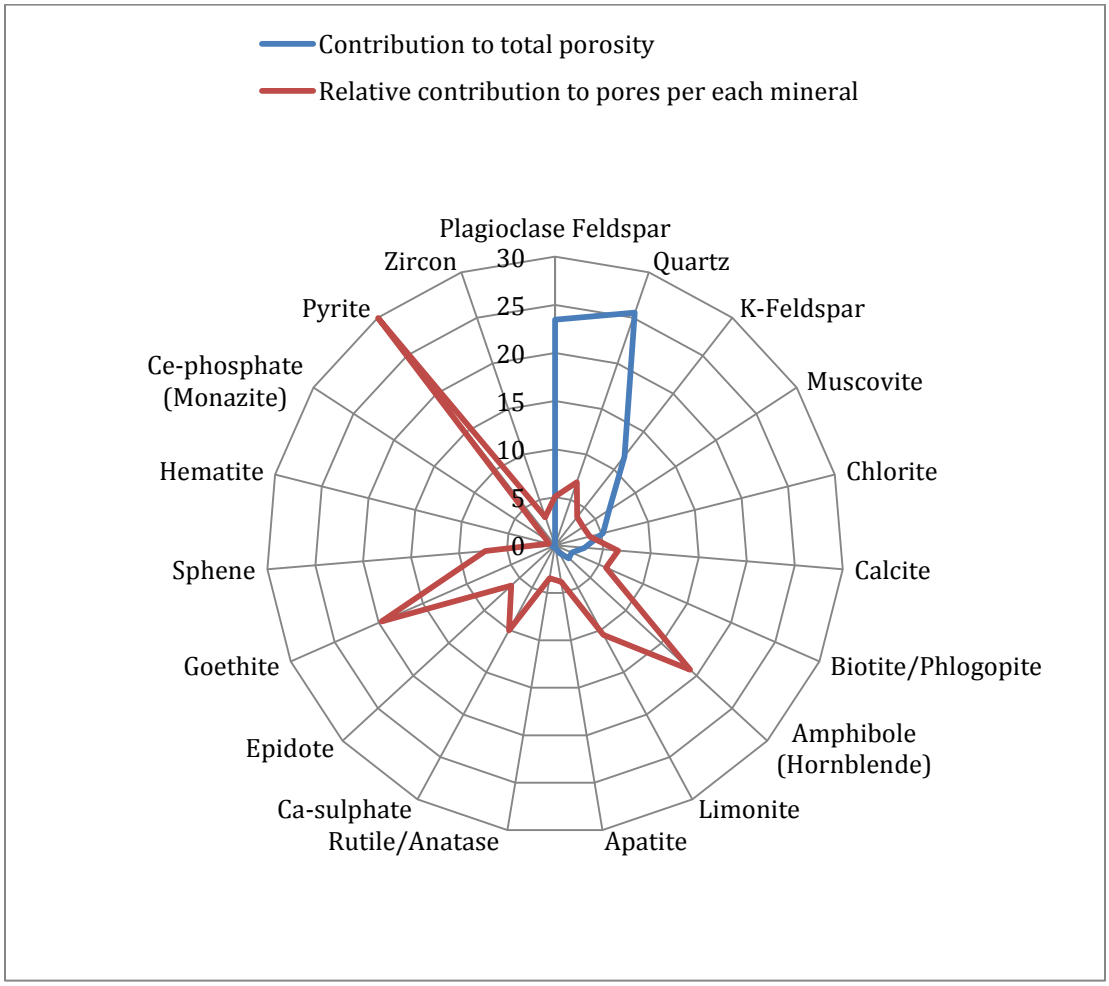

Figure 63. Association diagrams between mineralogy and pores and fractures (Navy II well 42A-16; 5000-5020 ft)

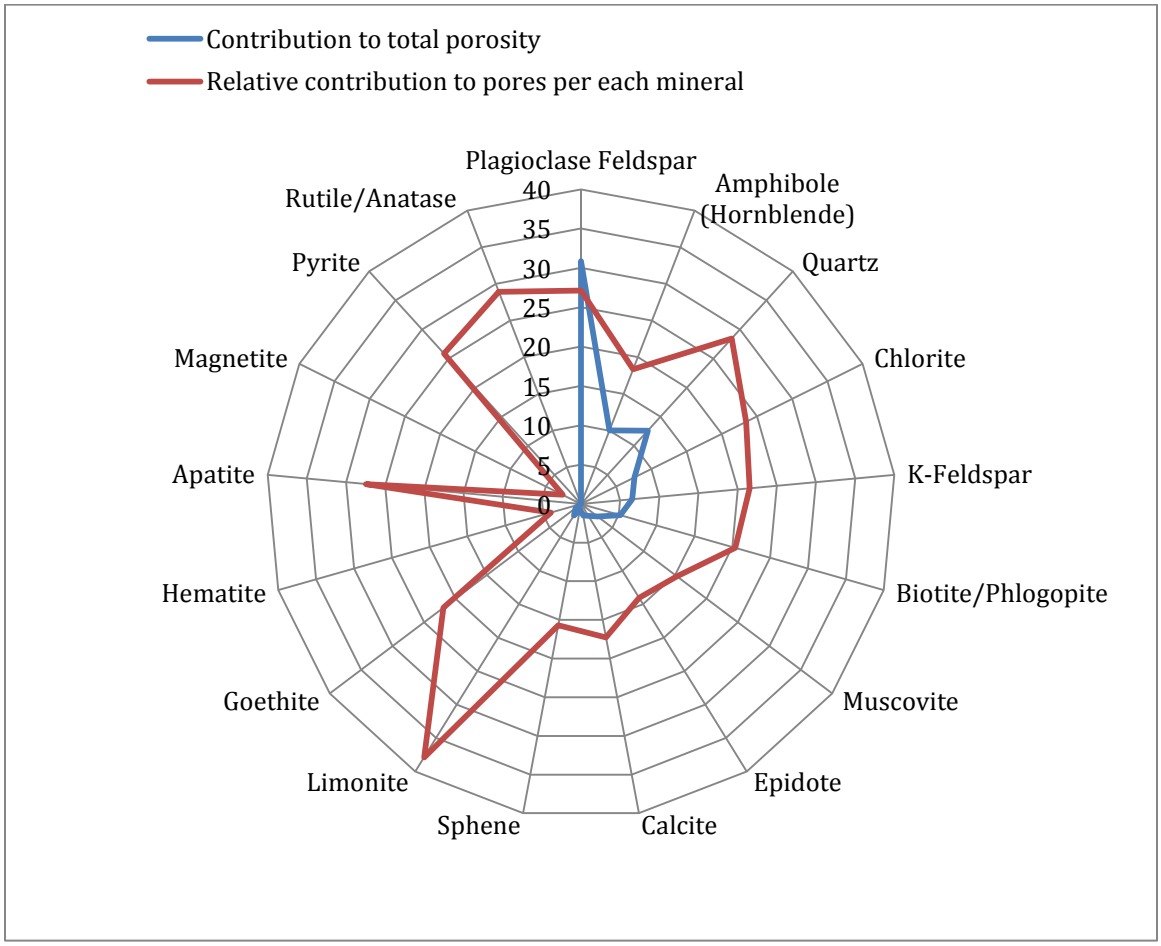

Figure 64. Association diagrams between mineralogy and pores and fractures (Navy II well 42A-16; 8010-8040 ft)

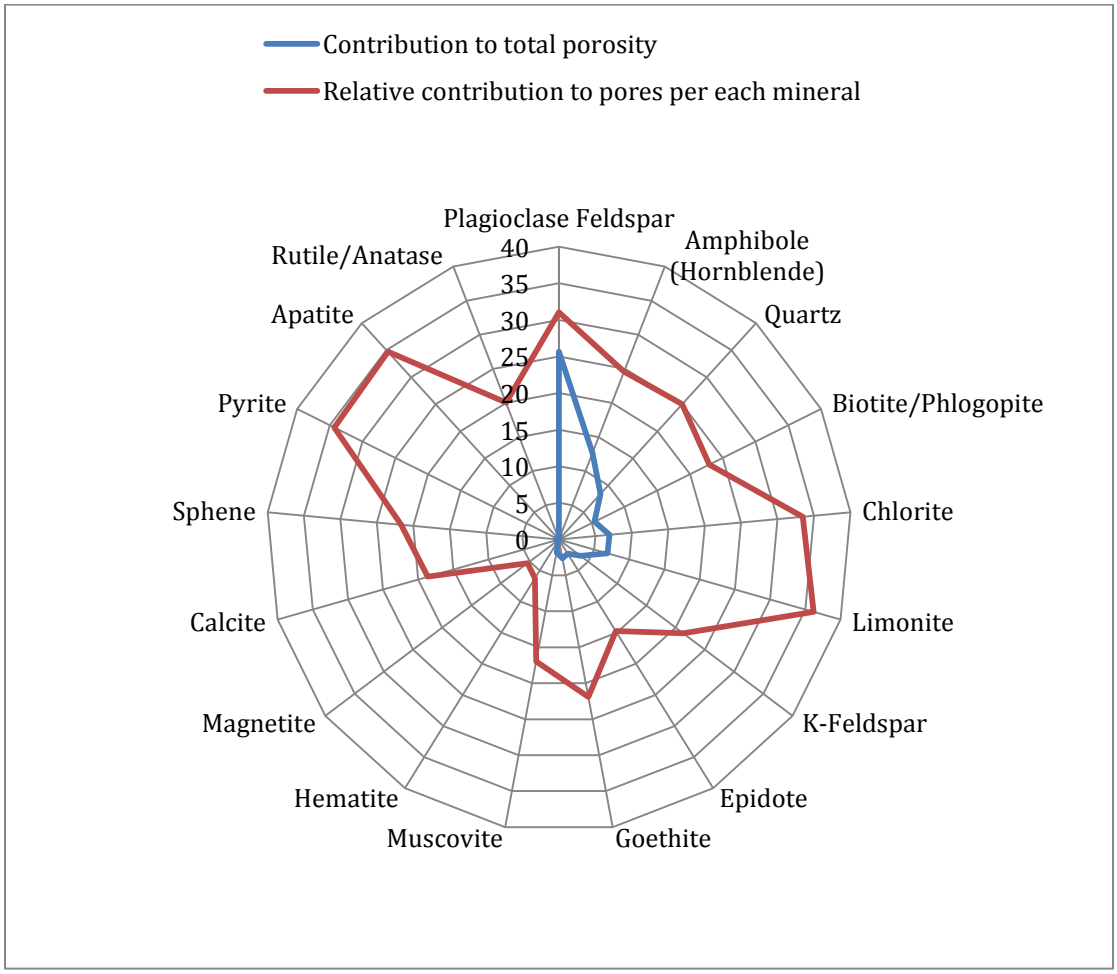

Figure 65. Association diagrams between mineralogy and pores and fractures (Navy II well 42A-16; 8900-8930 ft)

Appendix D: Fluid Chemistry of 1977 CGEH Well No. 1, 1967 Coso Well No. 1, and Well 28-33 at Coso, California

Table 8. Fluid chemistry of water from 1977 CGEH well No. 1 and 1967 Coso well No. 1 (data from Fournier et al (1980))

	1977 CGEH Well No. 1								1967 Coso Well No. 1			
	2	3	4	5	6	7	8	9	10	11	12	13
Date of collection	Dec. 2, 1977	Dec. 2, 1977	Dec. 2, 1977	March 17, 1978	March 18, 1978	March 18, 1978	July 12, 1978	July 12, 1978	Jan. 27, 1967	March 1968	March 1968	July 12, 1978
Sample collection point	wellhead	wellhead	wellhead	~835 m	~835 m	~1463 m	~1100 m	~1100 m	wellhead	wellhead	wellhead	~100 m
Sample temperature in well,˚C	~165	~165	~165	~192	~192	~186	~195	~195	116	142	142	-
Constituent, mg/kg												
Na	1600	1590	1590	1460	1500	1420	1510	1480	1764	2808	1632	1440
K	120	118	124	145	139	154	132	132	154	172	244	170
Ca	98	93	98	131	114	70	55	51	72.8	359	74.4	19.8
Mg	2.5	2.7	2.5	2.6	2.3	1.7	1	0.57	0.5	0.6	1.0	0.68
SiO_2	710*	710*	710*	37	41	201	119	149	50	27	154	84
B	53	56	58	54	66	65	49	55	48	57.4	71.6	47
Li	9.7	10.3	10	9.1	9.6	10.2	13	14	-	-	-	2.8
HCO_3	286	297	279	64	62	168	119	136	134	0	0	116
CO_3	0	0	0	0	0	0	0	0	84	50.4	77.4	0

Cl	2360	2460	2480	2470	2550	2300	2330	2360	2790	3681	3042	2370
F	3.8	3.8	4.2	-	-	-	3.3	4.2	3.7	1.6	2.2	3.3
SO_4	268	257	245	172	150	89	53	79	38	216	52.8	74
pH, field	-	-	-	5.3	5.2	5.6	5.4	-	-	-	-	6.5
pH, laboratory	7.74	8.14	8.22	-	-	-	7.49	7.75	8.9	9.8	8.5	7.75

*Total silica determined by atomic absorption using a nitrous oxide flame and includes silica in any colloidal clay dispersed in the water. Therefore the silica values probably are not indicative of the actual silica dissolved in the water.

Table 9. Fluid chemistry of water from well 28-33 (data from McLin (2012))

Well 28-33 values in ppm (mg/kg)

Date of collection	09/23 /93 [a]	12/12 /95 [b]	10/07 /96 [b]	10/30 /97 [a]	11/05 /97 [b]	04/28 /98 [a]	10/02 /98 [b]	10/21 /98 [a]	05/05 /99 [a]	01/24 /00 [b]	02/13 /01 [b]	07/27 /01 [b]	01/31 /02 [b]	04/27 /04 [b]
Na	228	433	420	429	441	447	417	412	432	454	448	441	459	415
K	6.13	70.9	71.1	70.1	71.7	67.8	63.9	65.5	66.2	74.9	58.7	65.0	62.4	56.2
Ca	15.6	9.19	8.36	7.4	8.17	7.5	8.54	7.21	6.68	8.8	6.47	7.13	7.21	5.32
Mg	2.08	-	-	0.02	-	<0.01	-	0.03	0.02	-	-	-	-	-
SiO_2	101	629	623	642	609	550	534	531	561	542	587	645	548	538
B	2.25	10.5	10.5	9.47	10.2	9.38	10.7	9.73	9.60	11.7	9.86	10.9	10.0	8.97
Li	0.35	-	-	2.24	-	2.28	1.75	2.03	2.24	2.58	2.11	1.59	1.98	2.07
HCO_3	140	132	126	115	148	73.2	140	75.6	85	153	199	188	167	157
CO_3	0	35	43	52.8	30.3	72	31	76.8	74	28	23.9	31.2	21.5	39.2
Cl	70.1	463	453	470	463	446	454	441	483	473	463	438	443	427
F	4.28	16.4	15	15.4	16.4	16.6	15	15.6	16.3	15.2	15.8	16.9	16	18.4
SO_4	273	214	214	199	200	199	211	199	213	221	238	242	234	182
pH, laboratory	7.58	-	-	9.13	-	9.01	-	9.38	9.1	-	-	-	-	-

Superscript in date refers to: a. reported by goff et al. (2002) and b. reported by Terra-Gen

Appendix E: Pressure and Temperature Profiles as a Function of Depth for Coso Navy II Well 42A-16 (Data from Jess McCulloch, pers. comm.)

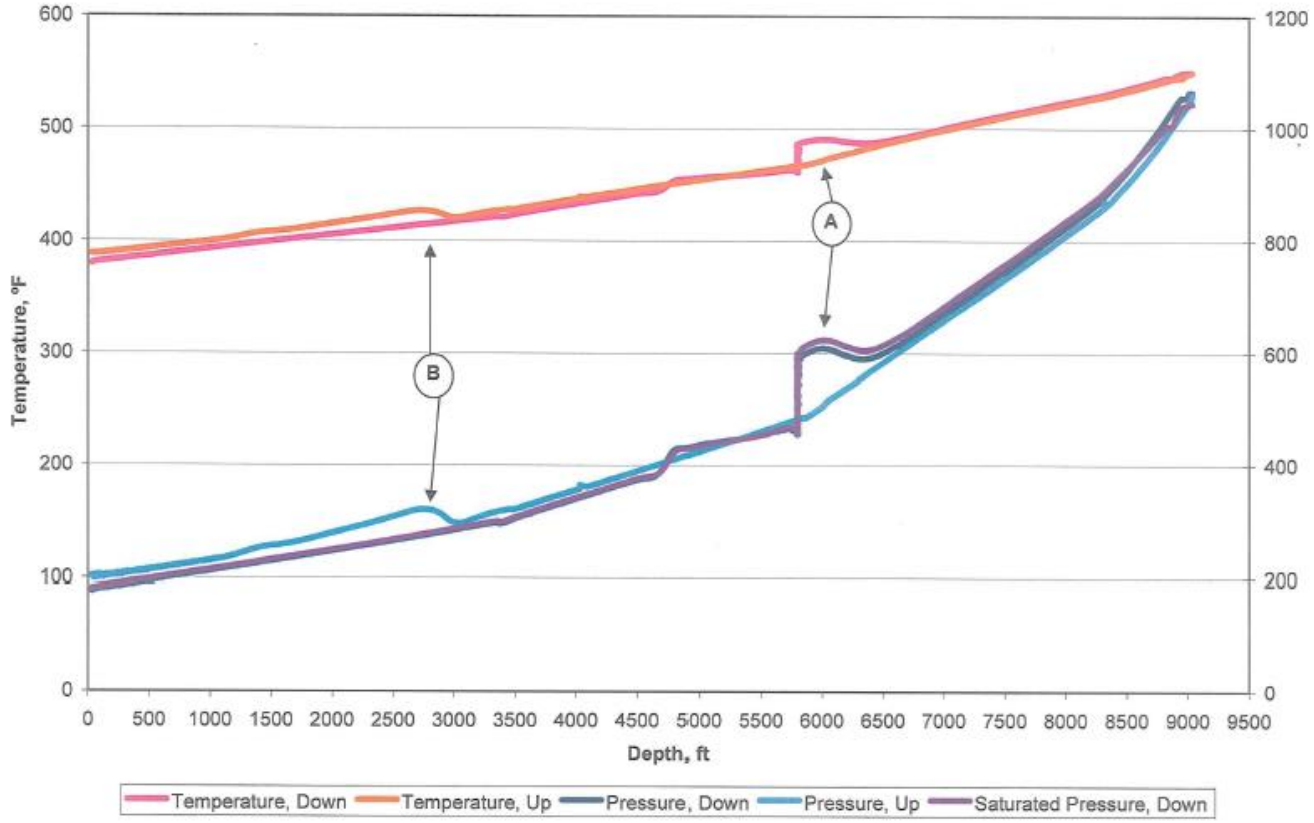

Figure 66. Pressure and temperature profiles as a function of depth for Coso Navy II well 42A-16 (Data from Jess McCulloch, pers. comm.)